# Plant Proteins as Multifunctional Additives in Polymer Composites

Barbara L. DeButts

Dissertation submitted to the faculty of the Virginia Polytechnic Institute and State University in partial fulfillment of the requirements for the degree of
Doctor of Philosophy
In
Macromolecular Science and Engineering

Justin R. Barone, Chair
Donald G. Baird
Michael J. Bortner
E. Johan Foster
Charles E. Frazier

March 27, 2019
Blacksburg, Virginia

Keywords: Polymer composite, Protein, Isoprene rubber, Poly(vinyl alcohol), Polymer processing

Plant Proteins as Multifunctional Additives in Polymer Composites

Barbara L. DeButts

## ABSTRACT

Wheat gluten, wheat gliadin, and corn zein agricultural proteins were evaluated as multifunctional additives that: (1) provided reinforcement, (2) improved thermal stability, and (3) lowered the cost of polymer composites. Wheat proteins were utilized in two polymer matrices: poly(vinyl alcohol) (PVA) and synthetic cis-1,4-polyisoprene rubber (IR). The proteins were hydrolyzed and dispersed in the polymer matrix, where they cooperatively self-assembled into nanostructures called amyloids. Amyloids have the potential for high rigidity and stability due to high β-sheet content. In Chapter II, trypsin hydrolyzed wheat gluten (THWG) proteins were incubated in aqueous PVA solutions, then the composite solutions were air dried and compression molded into films. Anisotropic protein aggregates formed through a typical mechanism of β-sheet self-assembly, where a greater molding time and pressure and/or a lower PVA molecular weight allowed for more protein aggregation. The larger protein structures provided less reinforcement. In Chapters III and IV, THWG and trypsin hydrolyzed gliadin (THGd), a component protein in wheat gluten, were compounded in synthetic polyisoprene rubber to form nanocomposites. The reinforcement correlated to the protein β-sheet content and varied with protein concentration, protein batch preparation, processing temperature, and compounding time. The isotropic β-sheet containing structures were very thermally stable, even under harsh rubber compounding conditions. By optimizing the processing parameters uniform protein dispersion and optimal IR reinforcement were achieved, although the protein and IR phases had poor compatibility. In Chapter V, the THGd-IR composites were cured using a typical cure package and molding process. Protein aggregation into nanostructured β-sheets was observed during the curing process. Rubber reinforcement increased as a function of protein concentration and curing time. In Chapter VI, a hydrophobic protein (zein) was substituted for the hydrophilic protein (gliadin) used previously to improve protein-IR compatibility. The zein protein was better at reinforcing IR, while gliadin improved mechanical stability. Both zein and gliadin improved the thermal stability of IR. The results from Chapters II-VI showed an interesting concept: *in situ* filler formation in polymer matrices where the choice of protein, polymer, and processing conditions influenced the final morphology and composite properties.

Plant Proteins as Multifunctional Additives in Polymer Composites

Barbara L. DeButts

GENERAL AUDIENCE ABSTRACT

We use plastics every day for a wide range of applications, from food packaging to automobile tires. Many of these plastics are composite materials, called "polymer composites," meaning they are made of two or more chemically distinct materials where one material is a polymer. For reference, a polymer is a long chain molecule made of many ("poly-") units ("-mer"). Polymer composites often contain additives which modify the properties of the polymer. For example, many soft polymers, such as tire rubber, need to be made stiffer and so a "reinforcing additive" is used to improve the stiffness of the rubber. Many composite materials are made stiffer so less material can be used. This process is called "lightweighting." The automotive industry and food packaging industry use this process to reduce weight and fuel costs. In this research, plant proteins are tested as reinforcing additives in polymer composites. Plant proteins, such as wheat gluten, are abundant, non-toxic, sustainable, and can self-assemble into extremely small, stiff structures. For these reasons, plant proteins offer an environmentally friendly alternative to typical reinforcing additives. This dissertation shows that plant proteins can reinforce two polymers with very different properties. The first polymer is poly(vinyl alcohol) (PVA), which is biodegradable, hydrophilic (i.e., "water loving"), and is commonly used in flexible food packaging. The second polymer is synthetic cis-1,4-polyisoprene rubber (IR), which is non-biodegradable, hydrophobic (i.e., "water fearing"), and is commonly used in automotive tires. In Chapters II-V, the wheat gluten protein is hydrolyzed, i.e., chemically "chopped" into short chain peptides, to encourage the self-assembly of the plant protein into small, stiff structures. The self-assembled protein structures survive typical industrial processing techniques, such harsh rubber compounding conditions which involve high heat, pressure, and shear forces (i.e., the material is pushed in opposing directions). In Chapter VI, full corn and wheat proteins are incorporated into IR using standard industrial mixing and curing processes. The corn and wheat proteins reinforce the synthetic rubber and inhibit the degradation of the chemical structure of cured rubber under high heat. At certain protein concentrations, the proteins improve the elasticity and lessen the permanent deformation in the polymer composite. Together, Chapters II-VI show that proteins from diverse plant sources can be used to improve the performance of polymers with dissimilar properties.

ACKNOWLEDGEMENT

I appreciate the advice and direction provided by my advisor Dr. Justin Barone, as well as my committee members Dr. Chip Frazier, Dr. Don Baird, Dr. Johan Foster and Dr. Michael Bortner, and Macromolecular Science and Engineering Program Director Dr. Robert Moore. Their guidance over the past four years has been integral to my transformation from artist to polymer engineer. Most importantly, I would like to thank my family for always believing I can do the impossible.

TABLE OF CONTENTS

LIST OF FIGURES

CHAPTER II



CHAPTER III

LIST OF TABLES

ABBREVIATIONS

| | |
|---|---|
| $\alpha$ | degree of cure |
| ATR FTIR | attenuated total reflectance Fourier transform infrared spectroscopy |
| BME | β-mercaptoethanol |
| BSE | backscatter electron |
| $\chi$ | Flory-Huggins polymer-solvent interaction parameter |
| CB | carbon black |
| CRI | Cure Rate Index |
| DSC | differential scanning calorimetry |
| $\overline{E}_\alpha$ | average activation energy |
| $\Delta H$ | heat of reaction |
| $\Delta H_f$ | experimental heat of fusion |
| $\Delta M$ | change in torque |
| $\Delta t$ | elapsed curing time |
| E | Young's modulus |
| $\epsilon$ | tensile elongation |
| G | shear modulus |
| G' | storage modulus |
| G" | loss modulus |
| Gd | gliadin from wheat protein |
| GR | guayule rubber |
| IR | synthetic cis-1,4-polyisoprene rubber |
| MH | maximum torque |
| ML | minimum torque |
| $M_t$ | elastic torque at time, t |
| NR | natural rubber |
| PCR | Peak Cure Rate |
| $\phi_r$ | volume fraction of rubber in a solvent swollen network |
| phr | parts per hundred rubber |
| PTFE | polytetrafluoroethylene |
| PVA | poly(vinyl alcohol) |

| | |
|---|---|
| REF | rubber elongation factor |
| RT | room temperature |
| S | sulfur |
| SEM-EDX | scanning electron microscopy with energy dispersive x-ray spectroscopy |
| $\sigma$ | tensile stress |
| SIL | (3-mercaptopropyl)triethoxysilane |
| tan $\delta$ | loss tangent |
| TBBS | N-tert-butyl-benzothiazole sulfonamide |
| $T_g$ | glass transition temperature |
| TGA | thermogravimetric analysis |
| THGd | trypsin hydrolyzed gliadin from wheat |
| THGd-SA | solution aggregated trypsin hydrolyzed gliadin from wheat |
| THWG | trypsin hydrolyzed wheat gluten |
| $T_m$ | melting temperature |
| ts1 | scorch/induction time |
| t'90 | time to 90% cure |
| $\Delta$t'100 | elapsed time to 100%cure |
| UTS | ultimate tensile strength |
| [X] | crosslink density |
| ZnO | zinc oxide |

## ATTRIBUTION

Author Barbara L. DeButts is the major contributor and writer of the manuscripts in Chapters 2-6. Co-author Dr. Justin Barone contributed to the research strategy, conclusions, and writing of the manuscripts in Chapters 2-6. Co-authors Cara R. Spivey (Chapter 2), Laura E. Hanzly (Chapter 3), Renee V. Thompson (Chapter 5) and Natasha Chauhan (Chapter 6) all contributed to the research within these manuscripts. The contributions of the co-authors is greatly appreciated. At the time of the research, Barbara L. DeButts was with the Macromolecules Innovation Institute and Macromolecular Science and Engineering, 1075 Life Science Circle, Suite 130, Virginia Tech, Blacksburg, VA 24061. The co-authors Cara R. Spivey and Renee V. Thompson performed parts of this research while in the "Biomechanics from molecular to organismal scales" NSF-Research Experience for Teachers (RET) program. Laura E. Hanzly was with the Department of Biological Systems Engineering, 203 Seitz Hall, Virginia Tech, Blacksburg VA 24061 and Natasha Chauhan was with the Department of Chemical Engineering, Virginia Tech, 245 Goodwin Hall, 635 Prices Fork Road, Blacksburg, VA 24061.

# CHAPTER I. INTRODUCTION AND LITERATURE REVIEW

## 1.1. Nanofillers and nanocomposite processing.

Polymer nanocomposites are of great interest to researchers and industry because of the promise of exceptional mechanical and barrier properties at low concentrations. Fillers with nanometer-scale dimensions generally have large surface areas and high width-to-thickness ratios, which lead to augmented filler-matrix interactions [1]. Thus, a low concentration of nanofiller has the potential to affect a large volume fraction of the matrix [2]. The problem with nanocomposites is that the high surface area creates surface forces between the particles, causing agglomeration. Even weak van der Waals forces become impactful because they are summed many times. This makes nanofillers very difficult to disperse into polymers using typical processing equipment.[3-4]

Typical polymer processing techniques have proven insufficient to overcome nanoparticle agglomeration. Characteristic nanocomposite preparation methods include solution or melt mixing, and in-situ polymerization.[5] Solution mixing requires toxic organic solvents, while melt mixing uses high heat and shear conditions and long residence times to disperse fillers.[6] Processing aids can improve dispersion but bear significant cost. *In-situ* polymerization, where monomers are mixed with nanofillers and then polymerized is limited to select polymers and requires an initiator or catalyst.[7] Thus, the most effective dispersion techniques, such as layer-by-layer assembly or *in situ* polymerization, are applicable only in special cases and are too time-intensive to adapt to large scale production.[8-11] Despite the huge advantages of nanocomposites reported for the past 20 years, a large volume practical application has not been realized.

## 1.2. Biocomposites.

Biological fillers for polymer composites offer many benefits, including cost reduction, environmental sustainability and recyclability, lower density, and the possibility of diverting material from the agricultural waste stream.[12] Not all biological fillers are equally sustainable and some, such as cotton, have high land and pesticide usage which decrease sustainability.[13] Furthermore, some biological fillers have been shown to have inferior properties, require low-processing temperatures, exhibit poor filler-polymer adhesion, or have a shortened composite life cycle compared to synthetic fillers.[13-14] For a biological filler to be industrially viable it must maintain or exceed the properties of the synthetic filler, be relatively low cost, and be processable with industry standard methods. Biological fillers typically begin to degrade between 150 and 220

°C, which restricts the type of processing conditions as well as the type of polymer matrices that can be used to those with low thermal transitions.[14-15]

1.3. Plant proteins as biological nanofillers for polymer composites.

To surmount the detriments of typical nanocomposite processing methods, a new, low-energy preparation method is proposed using a biological filler: plant proteins. *In situ* nanofiller formation exploits a biological process to form a nanophase within a polymer matrix. Proteins naturally self-assemble into crystalline β-sheet structures, which impart stiffness and mechanical stability to materials such as spider silk and amyloid fibers.[16] The aggregation behavior can be controlled to encourage the formation of preferred structures, resulting in designed functional nanomaterials with high moduli on the order of GPa.[17] Continued self-assembly of protein molecules into anisotropic structures results in the formation of amyloid protofibrils. Amyloids are commonly associated with pathological disorders such as neurodegenerative and prion diseases.[18-19] However, in certain living systems, amyloids protect and proliferate life. Non-disease related, or "functional," amyloids in barnacle cement and fungi improve adhesion and biofilm formation, respectively.[20-21] The β-sheet phase endows these materials with rigidity and toughness because of nanoscale modification. Theoretical predictions of protein self-assembly through non-covalent, non-ionic interactions, i.e. hydrogen bonding only, yield structures with elastic moduli of 10 to 20 GPa. Experimental results approach these values and show amyloid formation to be a highly evolved process, even when replicated *in vitro*.[17, 22-24] Thus, incorporating self-assembled amyloids into engineered materials like films, adhesives, and composites is of substantial interest in sustainable technology.[25]

*1.3.1. In-vitro amyloid self-assembly.*

*In situ* nanofiller formation utilizes a protein's natural tendency to self-assemble under denaturing conditions.[19, 26] In aqueous solution, protein molecules can aggregate or hierarchically self-assemble into supramolecular structures consisting of perpendicularly stacked rigid β-sheet nanostructures.[27-28] A very common and easy aggregation motif is when a protein molecule or "chain" unfolds, straightens, and hydrogen bonds to a nearby straightened chain to form a β-sheet.[27, 29-30] In a self-assembled β-sheet, hydrogen bonding happens between the main chain carbonyl (-C=O) on one protein and the main chain secondary amine (-NH) on another chain. The characteristic distance between 2 protein chains in a self-assembled β-sheet is ~0.47 nm.[26, 29-31] A pair of stacked β-sheets is the elementary "particle" from which larger structures form.

Hydrophobic interactions can further drive the packing of β-sheet structures into larger oligomeric or fibrillar structures, i.e. amyloid β-peptides (Aβ).[32-33] The conversion of low-density random coil (RC) structures to α-helical intermediates, then into high density β-sheet structures, is thought to be the universal aggregation pathway for many proteins.[34-36]

Protein unfolding and refolding is a dynamic process which is heavily impacted by external conditions. A change in protein secondary structure has been shown to result from 1) pressure, 2) an increase in conformational entropy with heat application, 3) pH changes, 4) the introduction of denaturants, such as alcohols, 5) increasing salt concentration and, 6) interfacial denaturing conditions.[37-39] α-β transitions have also been shown to occur spontaneously at air-water interfaces, due to hydrophobic interactions with the gas phase.[37] Thus, the morphological features and properties of the nanostructure can be easily altered by changes in solution pH, temperature, and ionic strength [40].

*1.3.2. A biological model: amyloid-like properties of natural rubber (NR).*

Natural rubber (NR), which is a product of the coagulation of the latex obtained from the *Hevea brasiliensis* tree, contains a few percent natural proteins and lipid. NR is used in demanding applications like airplane and truck tires because it has superior properties to synthetically-derived polyisoprene. It has long been believed that the combination of protein, lipid, and high molecular weight polyisoprene is the origin of NR's superior properties, but no definitive mechanism has been found.[41-43] In 2012, Berthelot et al.[44] identified rubber elongation factor (REF) proteins in NR which self-assemble into amyloids with high β-sheet content. It can be inferred that a highly reinforcing amyloid phase formed during rubber compounding would confer a significant property advantage to NR over other rubbers that do not contain the protein.[45] Protein powders ground to particle sizes of tens to hundreds of microns have been used before to reinforce rubber, but they were not aggregated or necessarily highly structured proteins.[46-48] It is proposed that introducing known aggregating proteins into IR, i.e., synthetic rubber, can create a composite that matches the properties of NR. This would be important to the use of synthetic rubber since NR is used in more demanding applications.

*1.3.3. Amyloid polymer composites in literature.*

There are a few reports of amyloid protofibril reinforcement of polymers in the literature. One study details the lysozyme protein protofibril reinforcement of cross-linked polydimethylsiloxane (PDMS).[49] At low filler concentrations (2 wt%), amyloids showed equal

reinforcement to carbon nanotubes (CNT). Another study described the lysozyme protofibril reinforcement of polylactic acid (PLA) at 1-5 wt% amyloid.[50] Modulus and strain-to-break increased as a function of amyloid content. In another report, insulin amyloid protofibrils were added to aqueous polyvinyl alcohol (PVA) solutions, then the water was evaporated.[51] The resulting 0.6 wt% amyloid-PVA nanocomposites were 15% stiffer than PVA. In each case, amyloid protofibrils were pre-formed in solution, then isolated and mixed into the polymer to form the nanocomposite.

1.4. Wheat gluten (WG) protein and WG hydrolysis.

As discussed above, exposing protein molecules to denaturing surfaces or denaturing conditions, such as applied stress or changes in solution pH, ionic strength, and temperature, can encourage β-sheet self-assembly.[52] Hydrolyzing full proteins to short chain peptides is another way to foster β-sheet formation.[40, 53] Many different proteins can be hydrolyzed or denatured to form β-sheet-containing amyloids.[18-19, 21, 52-56] Gluten, the protein component of wheat, can be hydrolyzed into peptides which, through extensive hydrogen bonding, form β-sheet nanostructures with superior properties.[40, 57] Unlike the full WG protein, the short glutamine-rich peptides produced from trypsin hydrolysis of WG can self-assemble at mild denaturing conditions into β-sheets.[58-59] Previous studies have shown that self-assembly could occur at near physiological conditions of 37 °C and pH 8, which were good conditions to perform the enzymatic hydrolysis in a repeatable manner.[60] At pH 8, WG is hydrolyzed by trypsin enzyme into smaller, more uniform peptides primarily ≤ 10 kDa molecular weight, with some residual 29 kDa and 37 kDa fragments.[58, 61] The peptide bonds in the component proteins of WG, i.e., gliadin (Gd) and low and high molecular weight glutenin (GtL and GtH), are preferentially cleaved by trypsin enzyme at arginine (R) and/or lysine (K) amino acids (Gd, UniProt P04721, 0.49 mol fraction; GtL, UniProt P10386, 0.45 mol fraction; GtH, UniProt P08488, 0.06 mol fraction).[60] Since aggregation into β-sheets occurs in solution, the reduction in peptide molecular weight is important to help solubilize the protein.[62]

In addition to the amyloid forming potential of WG, WG is also low cost, has good film forming ability and oxygen barrier properties, and has been explored as a biodegradable packaging material.[63] WG can be compression molded, which encourages hydrophobic interactions and can induce aggregation and crosslinking, thereby increasing tensile strength while lowering elongation to break.[64-66] A fully self-assembled WG composite film was produced by incubating THWG at

37 °C to form short amyloid fibers which, when dried, reinforced the remaining unassembled THWG polymer matrix.[34]

1.5. Packaging applications: Vinyl alcohol polymer matrices.

Poly(vinyl alcohol) (PVA) is a widely produced, water soluble and biodegradable polymer with good gas barrier properties, which has been reinforced with biological fillers to create sustainable, environmentally friendly composite films.[67-70] Poly(vinyl alcohol) films and composites can be used in multi-layer packaging applications. In a multi-layer film, a vinyl alcohol polymer layer is typically used as a core layer between polyolefin layers.[71] The function of the vinyl alcohol core is to act as a gas barrier, while the polyolefin layers serve to support the brittle vinyl alcohol layer and act as water barriers.[72] Introducing nanofillers can further improve the gas barrier properties of PVA by creating a tortuous diffusion pathway.[73] To reduce the brittleness of WG and/or PVA films, a plasticizer, such as glycerol, is commonly added.[49, 74] WG has been blended with PVA to form compression molded films.[50-51] However, these blends have used full WG proteins mixed with PVA to form a WG/polymer powder.

PVA is most commonly used in the packaging and fiber industries [69]. As the packaging industry strives to decrease material volume by making thinner films, the material must be engineered to maintain properties and performance. Moreover, increasing environmental concerns over end-of-life disposal necessitates low-cost, bio-based fillers. Rigid nanofillers, such as self-assembled β-sheets, have the potential to increase mechanical properties and impede solute permeability while still maintaining cost-competitiveness. Indeed, increased mechanical and thermal properties have been achieved with other amyloid fiber-filled PVA composites.[75]

1.6. Automotive applications: filled rubber systems.

The automotive industry is interested in new materials that will reduce weight, thereby improving fuel efficiency and reducing $CO_2$ emissions.[76-77] Additionally, legislation from the European Union and some Asian countries specify end-of-use guidelines that require a high percentage (95% target) of automotive parts to be reusable or recyclable.[78-79] Natural fibers, such as bamboo, cotton, flax, jute, pineapple, and sugarcane bagasse, have been incorporated into composites primarily used in the automotive interior.[13, 80] Commonly investigated biofillers for rubber tires include cellulose nanofibers, bio-silica, and lignin, amongst others.[81-84] Some biological fillers, such as lignocellulosic fibers can be incorporated into rubber using standard processing techniques.[85] The use of compatibilizers with hydrophilic natural fibers/fillers is

common. In addition to natural rubber, bio-based elastomers have been synthesized and offer the possibility of a completely "green" tire where both the filler and polymer matrix have biological origins.[86] Since end-of-life applications for scrap tires can include granulation and use as infill for synthetic turf, the desorption of volatile filler compounds from the rubber matrix is also of concern.[87]

Rubber nanocomposites are of interest, especially in the tire industry, because nanofillers can increase tear strength while decreasing viscoelastic losses and gas permeability.[88-89] Early rubber nanocomposite research focused on nanoclay, i.e., layered silicates, to reinforce natural or synthetic rubbers such as polyisoprene and styrene-butadiene.[90-94] More recently, other nanofillers have been studied, including nanocellulose, carbon nanotubes, and graphene oxide.[95-106] However, the most common rubber reinforcing fillers are petroleum-based carbon black (CB) and silica (clay), which can be difficult to disperse in rubber and are non-degradable.[107] Additionally, to effectively reinforce rubber, CB and silica must be present in high quantities, typically 50-70 parts per hundred rubber (phr).[108]

*1.6.1. Rubber processing.*

Synthetic polyisoprene rubber (IR) is a polymer matrix that is a melt, i.e., viscous polymer liquid, at room temperature and is typically processed at temperatures $\leq$ 150 °C.[109] Thus, IR represents an ideal matrix for use with biological fillers. Conventional manufacturing of rubber involves either a two-roll mill or internal mixer to compound fillers into rubber. Curing or thermosetting processes include compression molding, injection molding, and extrusion. In cured rubber, reinforcement results in improved stiffness and hardness, as well as improved resistance to abrasion, tear, cutting, and rupture.[110] In the uncured compounds, reinforcing fillers can have a significant effect on flow properties. To achieve optimal reinforcement, aggregate size and size distribution, surface area, and dispersion must be optimized.[111] Processing-induced flow is an important mode of dispersing and deagglomerating filler particles in filled-polymer systems. Three types of flow-induced dispersion have been studied: 1) agglomerate rupture, which occurs when the applied hydrodynamic stress is greater than the agglomerate cohesive strength, 2) erosion of small filler fragments from the agglomerate surface, and 3) collision-induced fragmentation.[112] Modeling of these dispersion mechanisms shows a linear shear rate dependency.[113] Thus, shear rate is another important processing parameter to consider.

*1.6.2. Basics of rubber curing.*

Sulfur vulcanization, i.e., curing, of rubber is a reaction between sulfur and rubber typically in the presence of a catalyst, which leads to the formation of a permanently crosslinked network.[114] It is a complex process in which a many-component system undergoes a series of reactions. A basic rubber curing recipe consists of four components: a rubber matrix, an activator system, an accelerator, and a crosslinking agent.[115-117] Typical industrial rubber compounds also contain additives such as reinforcing fillers, processing aids, retardants, compatibilizers, antidegradants, and antioxidants.[111] The concentration and chemical properties of the additives affect the cure kinetics and the final properties of the rubber vulcanizate.[118] The cure kinetics are further influenced by many other parameters, such as the cure temperature and characterization method.[119]

Rubber vulcanization proceeds through three distinct stages: induction, curing, and post-cure behavior. The induction period, also called the scorch time, is the pre-cure elapsed time during which the compound can be processed.[120] From a mechanistic perspective, accelerated sulfur vulcanization proceeds through the following steps: (1) an activator, usually zinc oxide (ZnO), forms an intermediate complex with an accelerator during the induction stage, (2) the accelerator-zinc complex reacts with sulfur to form an active sulfurating agent, (3) the active sulfurating agent reacts with rubber at the allylic hydrogen to form a crosslink precursor, (4) the crosslink precursor is converted to polysulfidic crosslinks, which is followed by (5) network maturation.[121-124]

*1.6.3. Activation by zinc oxide (ZnO).*

The activator system for sulfur-cured rubber is typically zinc oxide (ZnO, micron-sized, at a concentration of 5 parts per hundred rubber (phr)) combined with stearic acid (STE). The activator system is used in combination with a sulfenamide accelerator and sulfur crosslinking agent. The benefits of ZnO as an activator include improved vulcanization kinetics, processability, and physical properties, such as abrasion resistance.[125-127] ZnO may play a secondary role during network maturation by catalyzing a reduction in sulfur rank, i.e., converting polysulfidic crosslinks into di- or monosulfidic crosslinks, which increases crosslink density.[128] The use of ZnO as an activator is problematic because it is high density and possesses significant ecotoxicity.[129] ZnO has been proven poisonous to aquatic species. The Environmental Protection Agency (EPA) and European Union (EU) have called for a reduction in ZnO usage in commercial products due to its detrimental effects on aquatic organisms.[129-130]

Much of the research concerning ZnO-reduction in rubber has focused on reducing the amount of ZnO by reducing the quantity and/or particle size.[128] In particular, ZnO nanoparticles

(NPs) used in concentrations of 0.5-1 phr have been shown to successfully activate sulfur vulcanization, while providing additional rubber reinforcement.[130-131] However, ZnO NPs present the same environmental hazards as micron-sized ZnO.[132-134] Zinc oxide NPs enter waterways through rubber production and leachate from landfills. Once there, they can dissolve, forming toxic metal ions. In aquatic species, this results in an increase in the number of reactive oxidative species, as well as an increase in the oxidative stress response and/or chemosensitivity.[134] ZnO NPs have been shown to be cytotoxic to human epithelial cells at concentrations ≥ 100 mg/L. At drinking water concentrations ≥10 mg/L, they increase the oxidative stress response, which could potentially harm humans over time.[135] Few attempts have been made to completely replace ZnO with a more environmentally friendly activator [136].

Attempts have been made to reduce or eliminate zinc using multifunctional additives (MFAs), which are amines complexed with fatty acids. MFAs have the general structure of $[R'NH_2(CH_2)_3NH_3]^{2+}2[C_{17}H_{33}COO]^-$.[125] MFAs have been used as additives in a variety of synthetic and natural rubbers, resulting in improved processability, good cure characteristics and mechanical properties, but with a suppressed induction time. Ismail and Chia found that a MFA with diamine and carboxylic acid functionality was able to activate and accelerate sulfur curing of epoxidized natural rubber (ENR) in combination with 2 phr ZnO.[137] Enhanced tear strength and tensile properties were observed in the ENR vulcanizates, but the induction time was suppressed. In graphene oxide-natural rubber composites, hydroxyl and carboxylic acid functionalities were found to react with sulfur and form crosslinks, thereby accelerating the crosslinking reaction.[138] In another study, a complete substitution of ZnO was achieved using a secondary accelerator to activate curing. The amine complex had the structural formula of $NH_2$ --A[NH--$(CH_2)_x$ NH]$_n$ A--$NH_2$, where A represents an alkylene group and x = 2 or 3.[136] To facilitate the curing of synthetic rubber in this zinc-free system, an excess of sulfur (0.2 to 8 phr) and primary accelerator (0.1 to 2.5 phr) was required. In comparison, typical concentrations of sulfur and accelerator were 1-2.5 phr and 0.2-1.5 phr, respectively.

*1.6.4. Biological fillers as multifunctional additives (MFAs).*

Some natural reinforcing fillers have been found to have a beneficial effect on rubber curing kinetics. Da Costa et al.[139-140] found that a white rice husk ash reinforcing filler functioned in a catalytic capacity, accelerating the crosslinking reaction and lowering activation energy ($E_a$). Barrera and Cornish[141-142] studied the effect of waste-derived fillers as co-fillers for carbon black

and found that eggshell particles increased the rate of cure, which resulted in higher crosslink density and improved mechanical properties. Wheat gluten protein, a by-product of food production as consumers prefer "gluten-free" foods, has been successfully used as a reinforcing filler for various polymer matrices but not as part of the rubber curing package.[51]

*1.6.5. Practical considerations.*

In 2016, worldwide zinc production was in excess of 13 Mt.[144] Comparatively, in 2016, the worldwide crop production of wheat was 750 Mt, which was surpassed only by maize and rice.[145-146] The protein content (10-13%) of wheat, i.e., wheat gluten, is high compared to maize and rice (2-8% protein), so a significant amount of protein can be obtained from wheat production even if less is grown.[147] The gliadin fraction of wheat gluten is used in this study. Gliadin is approximately 40% of the total wheat grain protein.[148] Thus, the total gliadin from wheat protein available globally in 2016 was 30-34 Mt, which exceeded the production of 13 Mt of ZnO and makes gliadin a viable substitute for typical rubber fillers. A comparative cost analysis using the global commodity markets for zinc and wheat raw materials reveals that there is a significant advantage to using a wheat-filler as a replacement for typical rubber fillers. As of March 2018, the World Bank listed the cost of wheat grain as $190.6 per metric ton, while the price of Zn ore was $3,533/t.[149] Moreover, the price of Zn ore has steadily risen over the previous three years, totaling a $1,000/t increase since 2015, while the price of wheat has remained roughly the same. Thus, there are environmental and economic advantages to utilizing protein in cured rubber.

1.7. Research objectives.

*1.7.1. Objective 1.* Cooperatively self-assemble trypsin hydrolyzed wheat gluten (THWG) proteins into amyloid structures in an aqueous poly(vinyl alcohol) (PVA) solution to demonstrate *in situ* nanofiller formation. Thermally process the resulting THWG films by compression molding and characterize the thermal, mechanical, structural, and morphological properties of the films.

*1.7.2. Objective 2.* Compound hydrolyzed proteins previously shown to aggregate in aqueous solution in synthetic cis-1,4-polyisoprene rubber (IR) to form a reinforcing phase. Quantify the protein β-sheet content in THWG-IR or trypsin hydrolyzed gliadin (THGd)-IR compounds. Analyze the impact of the protein type, concentration, and aggregation state, and the compounding conditions on the mechanical, thermal, structural and morphological properties of the composite compounds.

*1.7.3. Objective 3.* Determine an optimized set of processing parameters for trypsin hydrolyzed gliadin from wheat protein (THGd) and synthetic isoprene rubber (IR) composite compounds. Investigate the dependence of the rheological properties and protein dispersion on compounding temperature, time, and speed. Examine the effect of drying the THGd hydrolysate at a slower rate or to a greater solids content on the composite properties.

*1.7.4. Objective 4.* Utilize trypsin hydrolyzed gliadin (THGd) from wheat protein as a reinforcement in zinc oxide (ZnO)-free cured THGd-IR composites. The objective is to self-assemble THGd during the curing process using a standard industrial cure recipe and processing method. Compare the change in curing kinetics, crosslink densities, mechanical properties, and structure as a function of THGd concentration, coupling agent concentration, and curing time. Determine the potential for a completely zinc-free rubber curing system.

*1.7.5. Objective 5.* Investigate alternate agricultural proteins as multifunctional additives, i.e., reinforcing fillers and anti-reversion agents, in a ZnO-free, cured, synthetic cis-1,4-polyisoprene rubber (IR) system. The proteins of interest are corn zein and wheat gliadin because of the difference in the hydrophobicity of each protein. Evaluate the effect of protein on the curing kinetics, mechanical properties, and composite morphology and compare to a system containing a zinc oxide (ZnO) activator or a carbon black (CB) reinforcing filler.

1.8. References.


1. Varghese, S.; Karger-Kocsis, J., Natural rubber-based nanocomposites by latex compounding with layered silicates. *Polymer* 2003, *44*, 4921-4927.
2. Vaia, R. A.; Giannelis, E. P., Polymer nanocomposites: status and opportunities. *MRS Bull.* 2001, *26*, 394-401.
3. Sinha Ray, S.; Okamoto, M., Polymer/layered silicate nanocomposites: a review from preparation to processing. *Prog. Polym. Sci.* 2003, *28*, 1539-1641.
4. Pavlidou, S.; Papaspyrides, C. D., A review on polymer–layered silicate nanocomposites. *Prog. Polym. Sci.* 2008, *33*, 1119-1198.
5. Ray, S. S.; Okamoto, M., Polymer/layered silicate nanocomposites: a review from preparation to processing. *Prog. Polym. Sci.* 2003, *28*, 1539-1641.
6. Zhao, R.; Torley, P.; Halley, P. J., Emerging biodegradable materials: starch- and protein-based bio-nanocomposites. *Journal of Materials Science* 2008, *43*, 3058-3071.

7. Kutz, M., *Applied Plastics Engineering Handbook: Processing and Materials*. William Andrew: Amsterdam, 2011; Vol. 1st.

8. Podsiadlo, P.; Choi, S.-Y.; Shim, B.; Lee, J.; Cuddihy, M.; Kotov, N. A., Molecularly engineered nanocomposites: layer-by-layer assembly of cellulose nanocrystals. *Biomacromolecules* 2005, *6*, 2914-2918.

9. Ou, Y.; Yang, F.; Yu, Z. Z., A new conception on the toughness of nylon 6/silica nanocomposite prepared via in situ polymerization. *J. Polym. Sci., Part B: Polym. Phys.* 1998, *36*, 789-795.

10. Zeng, C.; Lee, L. J., Poly (methyl methacrylate) and polystyrene/clay nanocomposites prepared by in-situ polymerization. *Macromolecules* 2001, *34*, 4098-4103.

11. Sun, T.; Garces, J. M., High-performance polypropylene–clay nanocomposites by in-situ polymerization with metallocene/clay catalysts. *Adv. Mater.* 2002, *14*, 128-130.

12. Rwawiire, S.; Tomkova, B.; Militky, J.; Jabbar, A.; Kale, B. M., Development of a biocomposite based on green epoxy polymer and natural cellulose fabric (bark cloth) for automotive instrument panel applications. *Composites Part B* 2015, *81*, 149-157.

13. Dunne, R.; Desai, D.; Sadiku, R.; Jayaramudu, J., A review of natural fibres, their sustainability and automotive applications. *J. Reinf. Plast. Compos.* 2016, *35*, 1041-1050.

14. Holbery, J.; Houston, D., Natural-fiber-reinforced polymer composites in automotive applications. *JOM* 2006, *58*, 80-86.

15. Espinach, F. X.; Granda, L. A.; Tarrés, Q.; Duran, J.; Fullana-i-Palmer, P.; Mutjé, P., Mechanical and micromechanical tensile strength of eucalyptus bleached fibers reinforced polyoxymethylene composites. *Composites Part B: Engineering* 2017, *116*, 333-339.

16. Keten, S.; Xu, Z.; Ihle, B.; Buehler, M. J., Nanoconfinement controls stiffness, strength and mechanical toughness of [beta]-sheet crystals in silk. *Nat. Mater.* 2010, *9*, 359-367.

17. Knowles, T. P. J.; Buehler, M. J., Nanomechanics of functional and pathological amyloid materials. *Nat. Nanotechnol.* 2011, *6*, 469-479.

18. Anand, G.; Sharma, S.; Dutta, A. K.; Kumar, S. K.; Belfort, G., Conformational Transitions of Adsorbed Proteins on Surfaces of Varying Polarity. *Langmuir* 2010, *26*, 10803-10811.

19. Sethuraman, A.; Vedantham, G.; Imoto, T.; Przybycien, T.; Belfort, G., Protein unfolding at interfaces: Slow dynamics of α-helix to β-sheet formation. *Proteins: Struct. Funct. Bioinform.* 2004, *56*, 669-678.

20. Prusiner, S. B., Neurodegenerative diseases and prions. *New Engl. J. Med.* 2001, *344*, 1516-1526.

21. Chiti, F.; Dobson, C. M., Protein misfolding, functional amyloid, and human disease. *Annu. Rev. Biochem.* 2006, *75*, 333-366.

22. Barlow, D. E.; Dickinson, G. H.; Orihuela, B.; Kulp III, J. L.; Rittschof, D.; Wahl, K. J., Characterization of the adhesive plaque of the barnacle *Balanus amphitrite*: Amyloid-like nanofibrils are a major component. *Langmuir* 2010, *26*, 6549-6556.

23. Gebbink, M. F. B. G.; Claessen, D.; Bouma, B.; Dijkhuizen, L.; Wosten, H. A. B., Amyloids-A functional coat for microorganisms. *Nat. Rev. Microbiol.* 2005, *3*, 333-341.

24. Adamcik, J.; Berquand, A.; Mezzenga, R., Single-step direct measurement of amyloid fibrils stiffness by peak force quantitative nanomechanical atomic force microscopy. *Appl. Phys. Lett.* 2011, *98*, 193701.

25. Adamcik, J.; Lara, C.; Usov, I.; Jeong, J. S.; Ruggeri, F. S.; Dietler, G.; Lashuel, H. A.; Hamley, I. W.; Mezzenga, R., Measurement of intrinsic properties of amyloid fibrils by the peak force QNM method. *Nanoscale* 2012, *4*, 4426-4429.

26. Nelson, R.; Sawaya, M. R.; Balbirnie, M.; Madsen, A. Ø.; Riekel, C.; Grothe, R.; Eisenberg, D., Structure of the cross-β spine of amyloid-like fibrils. *Nature* 2005, *435*, 773-778.

27. van Hest, J. C. M.; Tirrell, D. A., Protein-based materials, toward a new level of structural control. *Chem. Commun.* 2001, 1897-1904.

28. Ridgley, D. M.; Barone, J. R., Evolution of the amyloid fiber over multiple length scales. *ACS Nano* 2013, *7*, 1006-1015.

29. Sunde, M.; Serpell, L. C.; Bartlam, M.; Fraser, P. E.; Pepys, M. B.; Blake, C. C. F., Common core structure of amyloid fibrils by synchrotron X-ray diffraction. *J. Mol. Biol.* 1997, *273*, 729-739.

30. Makin, O. S.; Sikorski, P.; Serpell, L. C., Diffraction to study protein and peptide assemblies. *Curr. Opin. Chem. Biol.* 2006, *10*, 417-422.

31. Serpell, L. C.; Smith, J. M., Direct visualisation of the β-sheet structure of synthetic Alzheimer's amyloid. *J. Mol. Biol.* 2000, *299*, 225-231.

32. Cerf, E.; Sarroukh, R.; Tamamizu-Kato, S.; Breydo, L.; Derclaye, S.; Dufrêne, Y. F.; Narayanaswami, V.; Goormaghtigh, E.; Ruysschaert, J.-M.; Raussens, V., Antiparallel β-sheet: a signature structure of the oligomeric amyloid β-peptide. *Biochem. J.* 2009, *421*, 415-423.

33. Ghosh, D.; Singh, P. K.; Sahay, S.; Jha, N. N.; Jacob, R. S.; Sen, S.; Kumar, A.; Riek, R.; Maji, S. K., Structure based aggregation studies reveal the presence of helix-rich intermediate during α-Synuclein aggregation. *Scientific reports* 2015, *5*, 9228.

34. Claunch, E. C.; Ridgley, D. M.; Barone, J. R., Completely self-assembled fiber composites. *Composites Sci. Technol.* 2015.

35. Nabers, A.; Ollesch, J.; Schartner, J.; Kötting, C.; Genius, J.; Haußmann, U.; Klafki, H.; Wiltfang, J.; Gerwert, K., An infrared sensor analysing label-free the secondary structure of the Abeta peptide in presence of complex fluids. *Journal of Biophotonics* 2016, *9*, 224-234.

36. Surowka, A. D.; Pilling, M.; Henderson, A.; Boutin, H.; Christie, L.; Szczerbowska-Boruchowska, M.; Gardner, P., FTIR imaging of the molecular burden around Aβ deposits in an early-stage 3-Tg-APP-PSP1-TAU mouse model of Alzheimer's disease. *Analyst* 2017, *142*, 156-168.

37. Yohko, F. Y., Kinetics of protein unfolding at interfaces. *J. Phys.: Condens. Matter* 2012, *24*, 503101.

38. Jeyachandran, Y. L.; Mielczarski, E.; Rai, B.; Mielczarski, J. A., Quantitative and Qualitative Evaluation of Adsorption/Desorption of Bovine Serum Albumin on Hydrophilic and Hydrophobic Surfaces. *Langmuir* 2009, *25*, 11614-11620.

39. Yu, L.; Zhang, L.; Sun, Y., Protein behavior at surfaces: Orientation, conformational transitions and transport. *J. Chromatogr. A* 2015, *1382*, 118-134.

40. Ridgley, D. M.; Ebanks, K. C.; Barone, J. R., Peptide mixtures can self-assemble into large amyloid fibers of varying size and morphology. *Biomacromolecules* 2011, *12*, 3770-3779.

41. Tanaka, Y.; Tarachiwin, L., Recent advances in structural characterization of natural rubber. *Rubber Chem. Technol.* 2009, *82*, 283-314.

42. Sansatsadeekul, J.; Sakdapipanich, J.; Rojruthai, P., Characterization of associated proteins and phospholipids in natural rubber latex. *J. Biosci. Bioeng.* 2011, *111*, 628-634.

43. Rattanasom, N.; Thammasiripong, U.; Suchiva, K., Mechanical properties of deproteinized natural rubber in comparison with synthetic *cis*-1,4 polyisoprene vulcanizates: Gum and black-filled vulcanizates. *J. Appl. Polym. Sci.* 2005, *97*, 1139-1144.

44. Berthelot, K.; Lecomte, S.; Estevez, Y.; Coulary-Salin, B.; Bentaleb, A.; Cullin, C.; Deffieux, A.; Peruch, F., Rubber elongation factor (REF), a major allergen component in Hevea brasiliensis latex has amyloid properties. *PloS one* 2012, *7*, 48065.

45. Berthelot, K.; Lecomte, S.; Estevez, Y.; Peruch, F., Hevea brasiliensis REF (Hev b 1) and SRPP (Hev b 3): An overview on rubber particle proteins. *Biochimie* 2014, *106*, 1-9.

46. Jong, L., Rubber composites reinforced by soy spent flakes. *Polym. Int.* 2005, *54*, 1572-1580.

47. Jong, L., Characterization of soy protein/styrene–butadiene rubber composites. *Compos. Part A: Appl. Sci. Manuf.* 2005, *36*, 675-682.

48. Hergenrother, W. L.; Shultz, L. L.; Lin, C. J. Keratin in rubber applications. 2015.

49. Vo Hong, N.; Pyka, G.; Wevers, M.; Goderis, B.; Van Puyvelde, P.; Verpoest, I.; Van Vuure, A. W., Processing rigid wheat gluten biocomposites for high mechanical performance. *Compos. Part A: Appl. Sci. Manuf.* 2015, *79*, 74-81.

50. Dicharry, R. M.; Ye, P.; Saha, G.; Waxman, E.; Asandei, A. D.; Parnas, R. S., Wheat Gluten− Thiolated poly (vinyl alcohol) blends with improved mechanical properties. *Biomacromolecules* 2006, *7*, 2837-2844.

51. Dong, J.; Dicharry, R.; Waxman, E.; Parnas, R. S.; Asandei, A. D., Imaging and Thermal Studies of Wheat Gluten/Poly(vinyl alcohol) and Wheat Gluten/Thiolated Poly(vinyl alcohol) Blends. *Biomacromolecules* 2008, *9*, 568-573.

52. Fändrich, M.; Forge, V.; Buder, K.; Kittler, M.; Dobson, C. M.; Diekmann, S., Myoglobin forms amyloid fibrils by association of unfolded polypeptide segments. *Proc. Natl. Acad. Sci.* 2003, *100*, 15463.

53. Adamcik, J.; Jung, J.-M.; Flakowski, J.; De Los Rios, P.; Dietler, G.; Mezzenga, R., Understanding amyloid aggregation by statistical analysis of atomic force microscopy images. *Nat. Nanotechnol.* 2010, *5*, 423-428.

54. Eisenberg, D.; Weiss, R. M.; Terwilliger, T. C.; Wilcox, W., Hydrophobic moments and protein structure. *Faraday Symp. Chem. S.* 1982, *17*, 109-120.

55. Eisenberg, D.; Wilcox, W.; McLachlan, A. D., Hydrophobicity and amphiphilicity in protein structure. *J. Cell. Biochem.* 1986, *31*, 11-17.

56. Dunstan, D. E.; Hamilton-Brown, P.; Asimakis, P.; Ducker, W.; Bertolini, J., Shear flow promotes amyloid-β fibrilization. *Protein Eng. Des. Sel.* 2009, *22*, 741-746.

57. Ridgley, D. M.; Claunch, E. C.; Barone, J. R., Characterization of large amyloid fibers and tapes with Fourier Transform Infrared (FT-IR) and raman spectroscopy. *Appl. Spectrosc.* 2013, *67*, 1417-1426.

58. Athamneh, A. I.; Barone, J. R., Enzyme-mediated self-assembly of highly ordered structures from disordered proteins. *Smart Mater. Struct.* 2009, *18*, 104024.

59. Barone, J. R.; Athamneh, A., Large Self-Assembled Peptide Fibers. *Mater. Res. Soc. Symp. Proc.* 2011, *1301*.

60. Ridgley, D. M.; Claunch, E. C.; Barone, J. R., The effect of processing on large, self-assembled amyloid fibers. *Soft Matter* 2012, *8*, 10298-10306.

61. Tuck, C. S.; Latham, A.; Lee, P. W.; Barone, J. R., Wheat Gluten Plasticized with Its Own Hydrolysate. *J. Polym. Environ.* 2014, *22*, 430-438.

62. Fändrich, M.; Dobson, C. M., The behaviour of polyamino acids reveals an inverse side chain effect in amyloid structure formation. *EMBO J.* 2002, *21*, 5682-5690.

63. Zubeldía, F.; Ansorena, M. R.; Marcovich, N. E., Wheat gluten films obtained by compression molding. *Polym. Test.* 2015, *43*, 68-77.

64. Sun, S.; Song, Y.; Zheng, Q., Morphologies and properties of thermo-molded biodegradable plastics based on glycerol-plasticized wheat gluten. *Food Hydrocoll.* 2007, *21*, 1005-1013.

65. Sun, S.; Song, Y.; Zheng, Q., Thermo-molded wheat gluten plastics plasticized with glycerol: effect of molding temperature. *Food Hydrocoll.* 2008, *22*, 1006-1013.

66. Gällstedt, M.; Mattozzi, A.; Johansson, E.; Hedenqvist, M. S., Transport and Tensile Properties of Compression-Molded Wheat Gluten Films. *Biomacromolecules* 2004, *5*, 2020-2028.

67. Cheng, Q.; Wang, S.; Rials, T. G.; Lee, S.-H., Physical and mechanical properties of polyvinyl alcohol and polypropylene composite materials reinforced with fibril aggregates isolated from regenerated cellulose fibers. *Cellulose* 2007, *14*, 593-602.

68. Zhang, W.; Yang, X.; Li, C.; Liang, M.; Lu, C.; Deng, Y., Mechanochemical activation of cellulose and its thermoplastic polyvinyl alcohol ecocomposites with enhanced physicochemical properties. *Carbohydr. Polym.* 2011, *83*, 257-263.

69. Chiellini, E.; Corti, A.; D'Antone, S.; Solaro, R., Biodegradation of poly (vinyl alcohol) based materials. *Prog. Polym. Sci.* 2003, *28*, 963-1014.

70. Siddaramaiah; Raj, B.; Somashekar, R., Structure–property relation in polyvinyl alcohol/starch composites. *J. Appl. Polym. Sci.* 2004, *91*, 630-635.

71. Schroeder, G. O. Multi-layer barrier film. Mar 3, 1981, 1981.

72. Cheng, A.; Rodriguez, F., Mechanical properties of borate crosslinked poly(vinyl alcohol) gels. *J. Appl. Polym. Sci.* 1981, *26*, 3895 - 3908.

73. Kim, H. M.; Lee, J. K.; Lee, H. S., Transparent and high gas barrier films based on poly(vinyl alcohol)/graphene oxide composites. *Thin Solid Films* 2011, *519*, 7766-7771.

74. Lagrain, B.; Goderis, B.; Brijs, K.; Delcour, J. A., Molecular basis of processing wheat gluten toward biobased materials. *Biomacromolecules* 2010, *11*, 533-541.

75. Rao, S. P.; Meade, S. J.; Healy, J. P.; Sutton, K. H.; Larsen, N. G.; Staiger, M. P.; Gerrard, J. A., Amyloid fibrils as functionalizable components of nanocomposite materials. *Biotechnol. Prog.* 2012, *28*, 248-256.

76. Kc, B.; Faruk, O.; Agnelli, J. A. M.; Leao, A. L.; Tjong, J.; Sain, M., Sisal-glass fiber hybrid biocomposite: Optimization of injection molding parameters using Taguchi method for reducing shrinkage. *Compos. Part A: Appl. Sci. Manuf.* 2016, *83*, 152-159.

77. Park, G.; Park, H., Structural design and test of automobile bonnet with natural flax composite through impact damage analysis. *Compos. Struct.* 2018, *184*, 800-806.

78. Yang, S. S.; Nasr, N.; Ong, S. K.; Nee, A. Y. C., Designing automotive products for remanufacturing from material selection perspective. *J. Clean. Prod.* 2017, *153*, 570-579.

79. Despeisse, M.; Kishita, Y.; Nakano, M.; Barwood, M., Towards a Circular Economy for End-of-Life Vehicles: A Comparative Study UK – Japan. *Procedia CIRP* 2015, *29*, 668-673.

80. Al-Oqla, F. M.; Sapuan, S.; Ishak, M.; Nuraini, A., A decision-making model for selecting the most appropriate natural fiber–Polypropylene-based composites for automotive applications. *J. Compos. Mater.* 2016, *50*, 543-556.

81. Phakkeeree, T.; Ikeda, Y.; Yokohama, H.; Phinyocheep, P.; Kitano, R.; Kato, A., Network-Like Structure of Lignin in Natural Rubber Matrix to Form High Performance Elastomeric Bio-composite. *Journal of Fiber Science and Technology* 2016, *72*, 160-165.

82. Kato, A.; Tohsan, A.; Kohjiya, S.; Phakkeeree, T.; Phinyocheep, P.; Ikeda, Y., 12 - Manufacturing and Structure of Rubber Nanocomposites. In *Progress in Rubber Nanocomposites*, Woodhead Publishing: 2017; pp 415-461.

83. Smitthipong, W.; Suethao, S.; Shah, D.; Vollrath, F., Interesting green elastomeric composites: Silk textile reinforced natural rubber. *Polym. Test.* 2016, *55*, 17-24.

84. Hariwongsanupab, N.; Thanawan, S.; Amornsakchai, T.; Vallat, M.-F.; Mougin, K., Improving the mechanical properties of short pineapple leaf fiber reinforced natural rubber by blending with acrylonitrile butadiene rubber. *Polym. Test.* 2017, *57*, 94-100.

85. Zhou, Y.; Fan, M.; Chen, L.; Zhuang, J., Lignocellulosic fibre mediated rubber composites: An overview. *Composites Part B* 2015, *76*, 180-191.

86. Wang, R.; Zhang, J.; Kang, H.; Zhang, L., Design, preparation and properties of bio-based elastomer composites aiming at engineering applications. *Composites Sci. Technol.* 2016, *133*, 136-156.

87. Canepari, S.; Castellano, P.; Astolfi, M. L.; Materazzi, S.; Ferrante, R.; Fiorini, D.; Curini, R., Release of particles, organic compounds, and metals from crumb rubber used in synthetic turf under chemical and physical stress. *Environ. Sci. Pollut. Res.* 2018, *25*, 1448-1459.

88. Sengupta, R.; Chakraborty, S.; Bandyopadhyay, S.; Dasgupta, S.; Mukhopadhyay, R.; Auddy, K.; Deuri, A. S., A short review on rubber/clay nanocomposites with emphasis on mechanical properties. *Polym. Eng. Sci.* 2007, *47*, 1956-1974.

89. Bhattacharya, M.; Biswas, S.; Bhowmick, A. K., Permeation characteristics and modeling of barrier properties of multifunctional rubber nanocomposites. *Polymer* 2011, *52*, 1562-1576.

90. Galimberti, M., Rubber clay nanocomposites. In *Advanced Elastomers - Technology, Properties, and Applications*, Boczkowska, A., Ed. InTech: Rijeka, Croatia, 2012; pp 91-120.

91. Liu, Q.; Zhang, Y.; Xu, H., Properties of vulcanized rubber nanocomposites filled with nanokaolin and precipitated silica. *Appl. Clay Sci.* 2008, *42*, 232-237.

92. Varghese, S.; Karger-Kocsis, J., Melt-compounded natural rubber nanocomposites with pristine and organophilic layered silicates of natural and synthetic origin. *J. Appl. Polym. Sci.* 2004, *91*, 813-819.

93. Wang, Y.; Zhang, L.; Tang, C.; Yu, D., Preparation and characterization of rubber–clay nanocomposites. *J. Appl. Polym. Sci.* 2000, *78*, 1879-1883.

94. Zhang, L. Q.; Wang, Y.; Wang, Y.; Sui, Y.; Yu, D., Morphology and mechanical properties of clay/styrene-butadiene rubber nanocomposites. *J. Appl. Polym. Sci.* 2000, *78*, 1873-1878.

95. Bokobza, L., Multiwall carbon nanotube elastomeric composites: A review. *Polymer* 2007, *48*, 4907-4920.

96. Bouthegourd, E.; Rajisha, K. R.; Kalarical, N.; Saiter, J. M.; Thomas, S., Natural rubber latex/potato starch nanocrystal nanocomposites: Correlation morphology/electrical properties. *Mater. Lett.* 2011, *65*, 3615-3617.

97. Bras, J.; Hassan, M. L.; Bruzesse, C.; Hassan, E. A.; El-Wakil, N. A.; Dufresne, A., Mechanical, barrier, and biodegradability properties of bagasse cellulose whiskers reinforced natural rubber nanocomposites. *Ind. Crops Prod.* 2010, *32*, 627-633.

98. De Falco, A.; Goyanes, S.; Rubiolo, G. H.; Mondragon, I.; Marzocca, A., Carbon nanotubes as reinforcement of styrene–butadiene rubber. *Appl. Surf. Sci.* 2007, *254*, 262-265.

99. Deng, F.; Ito, M.; Noguchi, T.; Wang, L.; Ueki, H.; Niihara, K.-i.; Kim, Y. A.; Endo, M.; Zheng, Q.-S., Elucidation of the Reinforcing Mechanism in Carbon Nanotube/Rubber Nanocomposites. *ACS Nano* 2011, *5*, 3858-3866.

100. Fakhru'l-Razi, A.; Atieh, M. A.; Girun, N.; Chuah, T. G.; El-Sadig, M.; Biak, D. R. A., Effect of multi-wall carbon nanotubes on the mechanical properties of natural rubber. *Compos. Struct.* 2006, *75*, 496-500.

101. Montesdeoca-Esponda, S.; Sosa-Ferrera, Z.; Kabir, A.; Furton, K.; Santana-Rodríguez, J., Fabric phase sorptive extraction followed by UHPLC-MS/MS for the analysis of benzotriazole UV stabilizers in sewage samples. *Anal. Bioanal. Chem.* 2015, 1-14.

102. Gopalan Nair, K.; Dufresne, A., Crab Shell Chitin Whisker Reinforced Natural Rubber Nanocomposites. 1. Processing and Swelling Behavior. *Biomacromolecules* 2003, *4*, 657-665.

103. Kueseng, K.; Jacob, K. I., Natural rubber nanocomposites with SiC nanoparticles and carbon nanotubes. *Eur. Polym. J.* 2006, *42*, 220-227.

104. Le, H. H.; Parsaker, M.; Sriharish, M. N.; Henning, S.; Menzel, M.; Wiebner, S.; Das, A.; Do, Q. K.; Heinrich, G.; Radusch, H.-J., Effect of rubber polarity on selective wetting of carbon nanotubes in ternary blends. *Express Polym. Lett.* 2015, *9*, 960-971.

105. Potts, J. R.; Shankar, O.; Du, L.; Ruoff, R. S., Processing–Morphology–Property Relationships and Composite Theory Analysis of Reduced Graphene Oxide/Natural Rubber Nanocomposites. *Macromolecules* 2012, *45*, 6045-6055.

106. Siqueira, G.; Tapin-Lingua, S.; Bras, J.; da Silva Perez, D.; Dufresne, A., Mechanical properties of natural rubber nanocomposites reinforced with cellulosic nanoparticles obtained from combined mechanical shearing, and enzymatic and acid hydrolysis of sisal fibers. *Cellulose* 2011, *18*, 57-65.

107. Ma, J.; Zhang, L.-Q.; Geng, L., Manufacturing Techniques of Rubber Nanocomposites. In *Rubber Nanocomposites*, John Wiley & Sons, Ltd: 2010; pp 21-62.

108. Tzounis, L.; Debnath, S.; Rooj, S.; Fischer, D.; Mäder, E.; Das, A.; Stamm, M.; Heinrich, G., High performance natural rubber composites with a hierarchical reinforcement structure of carbon nanotube modified natural fibers. *Mater. Des.* 2014, *58*, 1-11.

109. D3182-16 Standard Practice for Rubber-Materials, Equipment, and Procedures for Mixing Standard Compounds and Preparing Standard Vulcanized Sheets. ASTM International: On-line, 2016; p 8.

110. Leblanc, J. L., Rubber–filler interactions and rheological properties in filled compounds. *Prog. Polym. Sci.* 2002, *27*, 627-687.

111. Erman, B.; Mark, J. E.; Roland, C. M., *The science and technology of rubber*. 4 ed.; Elsevier Academic Press: Boston, 2013; p 816.

112. Seyvet, O.; Navard, P., Collision-induced dispersion of agglomerate suspensions in a shear flow. *J. Appl. Polym. Sci.* 2000, *78*, 1130-1133.

113. Olalla, B.; Carrot, C.; Fulchiron, R.; Boudimbou, I.; Peuvrel-disdier, E., Analysis of the influence of polymer viscosity on the dispersion of magnesium hydroxide in a polyolefin matrix. *Rheol. Acta* 2012, *51*, 235-247.

114. Coran, A. Y., Vulcanization. In *The Science and Technology of Rubber*, 4 ed.; Mark, J. E.; Erman, B.; Roland, M., Eds. Academic press: Waltham, MA, 2013; pp 339-385.

115. Rodger, E., Vulcanization systems. In *Developments in Rubber Technology*, A. Whelan; Lee, K. S., Eds. Springer: Netherlands, 1979; Vol. 1, pp 105-117.

116. Dunn, J.; Scanlan, J.; Watson, W., Stress relaxation during the thermal oxidation of vulcanized natural rubber. *Trans. Faraday Society* 1959, *55*, 667-675.

117. Lee, C.; Poh, B., Temperature dependence of Mooney scorch time of rubber compounds. *J. Appl. Polym. Sci.* 1985, *30*, 71-81.

118. Chough, S. H.; Chang, D. H., Kinetics of sulfur vulcanization of NR, BR, SBR, and their blends using a rheometer and DSC. *J. Appl. Polym. Sci.* 1996, *61*, 449-454.

119. Kamal, M.; Sourour, S., Kinetics and thermal characterization of thermoset cure. *Polym. Eng. Sci.* 1973, *13*, 59-64.

120. Engels, H.-W.; Weidenhaupt, H.-J.; Pieroth, M.; Hofmann, W.; Menting, K.-H.; Mergenhagen, T.; Schmoll, R.; Uhrlandt, S., Rubber, 9. Chemicals and Additives. In *Ullmann's*

*Encyclopedia of Industrial Chemistry*, Wiley-VCH Verlag GmbH & Co. KGaA: Weinheim, 2011; pp 1-66.

121. Krejsa, M.; Koenig, J., A review of sulfur crosslinking fundamentals for accelerated and unaccelerated vulcanization. *Rubber Chem. Technol.* 1993, *66*, 376-410.

122. Ding, R.; Leonov, A., A kinetic model for sulfur accelerated vulcanization of a natural rubber compound. *J. Appl. Polym. Sci.* 1996, *61*, 455-463.

123. Loo, C. T., High temperature vulcanization of elastomers: 2. Network structures in conventional sulphenamide-sulphur natural rubber vulcanizates. *Polymer* 1974, *15*, 357-365.

124. Kruželák, J.; Sýkora, R.; Hudec, I., Sulphur and peroxide vulcanisation of rubber compounds–overview. *Chem. Pap. - Chem. Zvesti* 2016, *70*, 1533-1555.

125. Heideman, G.; Noordermeer, J. W.; Datta, R. N.; van Baarle, B., Multifunctional additives as zinc-free curatives for sulfur vulcanization. *Rubber Chem. Technol.* 2006, *79*, 561-588.

126. Das, A.; Wang, D.-Y.; Leuteritz, A.; Subramaniam, K.; Greenwell, H. C.; Wagenknecht, U.; Heinrich, G., Preparation of zinc oxide free, transparent rubber nanocomposites using a layered double hydroxide filler. *J. Mater. Chem.* 2011, *21*, 7194-7200.

127. Manoharan, P.; Chandra Das, N.; Naskar, K., On-demand tuned hazard free elastomeric composites: A green approach. *Biopolymers* 2017, *107*.

128. Heideman, G.; Datta, R.; Noordermeer, J. W.; Baarle, B. v., Influence of zinc oxide during different stages of sulfur vulcanization. Elucidated by model compound studies. *J. Appl. Polym. Sci.* 2005, *95*, 1388-1404.

129. Bindu, P.; Thomas, S., Viscoelastic Behavior and Reinforcement Mechanism in Rubber Nanocomposites in the Vicinity of Spherical Nanoparticles. *J. Phys. Chem. B* 2013, *117*, 12632-12648.

130. Panampilly, B.; Thomas, S., Nano ZnO as cure activator and reinforcing filler in natural rubber. *Polym. Eng. Sci.* 2013, *53*, 1337-1346.

131. Roy, K.; Alam, M. N.; Mandal, S. K.; Debnath, S. C., Surface modification of sol–gel derived nano zinc oxide (ZnO) and the study of its effect on the properties of styrene–butadiene rubber (SBR) nanocomposites. *J. Nanostruct. Chem.* 2014, *4*, 133-142.

132. Dale, A. L.; Lowry, G. V.; Casman, E. A., Stream Dynamics and Chemical Transformations Control the Environmental Fate of Silver and Zinc Oxide Nanoparticles in a Watershed-Scale Model. *Environ. Sci. Technol.* 2015, *49*, 7285-7293.

133. Ma, H.; Williams, P. L.; Diamond, S. A., Ecotoxicity of manufactured ZnO nanoparticles – A review. *Environ. Pollut.* 2013, *172*, 76-85.

134. Wu, B.; Torres-Duarte, C.; Cole, B. J.; Cherr, G. N., Copper Oxide and Zinc Oxide Nanomaterials Act as Inhibitors of Multidrug Resistance Transport in Sea Urchin Embryos: Their Role as Chemosensitizers. *Environ. Sci. Technol.* 2015, *49*, 5760-5770.

135. Giovanni, M.; Tay, C. Y.; Setyawati, M. I.; Xie, J.; Ong, C. N.; Fan, R.; Yue, J.; Zhang, L.; Leong, D. T., Toxicity profiling of water contextual zinc oxide, silver, and titanium dioxide nanoparticles in human oral and gastrointestinal cell systems. *Environ. Toxicol.* 2015, *30*, 1459-1469.

136. Sandstrom, P. H. Vulcanization accelerating diamines. April 25, 1989.

137. Ismail, H.; Chia, H. H., The Effects of Multifunctional Additive and Epoxidation in Silica Filled Natural Rubber Compounds. *Polym. Test.* 1998, *17*, 199-210.

138. Wu, J.; Xing, W.; Huang, G.; Li, H.; Tang, M.; Wu, S.; Liu, Y., Vulcanization kinetics of graphene/natural rubber nanocomposites. *Polymer* 2013, *54*, 3314-3323.

139. da Costa, H. M.; Visconte, L. L. Y.; Nunes, R. C. R.; Furtado, C. R. G., Rice husk ash filled natural rubber. III. Role of metal oxides in kinetics of sulfur vulcanization. *J. Appl. Polym. Sci.* 2003, *90*, 1519-1531.

140. Da Costa, H.; Visconte, L.; Nunes, R.; Furtado, C., Rice-husk-ash-filled natural rubber. II. Partial replacement of commercial fillers and the effect on the vulcanization process. *J. Appl. Polym. Sci.* 2003, *87*, 1405-1413.

141. Barrera, C. S.; Cornish, K., Processing and mechanical properties of natural rubber/waste-derived nano filler composites compared to macro and micro filler composites. *Ind. Crops Prod.* 2017, *107*, 217-231.

142. Barrera, C. S.; Cornish, K., High performance waste-derived filler/carbon black reinforced guayule natural rubber composites. *Ind. Crops Prod.* 2016, *86*, 132-142.

143. Ahmad, I. A.; Justin, R. B., Enzyme-mediated self-assembly of highly ordered structures from disordered proteins. *Smart Mater. Struct.* 2009, *18*, 104024.

144. Van Genderen, E.; Wildnauer, M.; Santero, N.; Sidi, N., A global life cycle assessment for primary zinc production. *Int. J. Life Cycle Assess.* 2016, *21*, 1580-1593.

145. Food and Agriculture Organization of the United Nations. www.fao.org/faostat (accessed Mar 23).

146. Asseng, S.; Cammarano, D.; Basso, B.; Chung, U.; Alderman, P. D.; Sonder, K.; Reynolds, M.; Lobell, D. B., Hot spots of wheat yield decline with rising temperatures. *Global Change Biol.* 2017, *23*, 2464-2472.

147. Weegels, P. L.; Marseille, J. P.; Hamer, R. J., Enzymes as a Processing Aid in the Separation of Wheat Flour into Starch and Gluten. *Starch - Stärke* 1992, *44*, 44-48.

148. Daniel, C.; Triboi, E., Effects of Temperature and Nitrogen Nutrition on the Grain Composition of Winter Wheat: Effects on Gliadin Content and Composition. *J. Cereal Sci.* 2000, *32*, 45-56.

149. World Bank Commodities Price Data (The Pink Sheet). http://www.worldbank.org/commodities (accessed Mar 24).

# CHAPTER II. WHEAT GLUTEN AGGREGATES AS A REINFORCEMENT FOR POLY(VINYL ALCOHOL) FILMS

DeButts, B. L., Spivey, C. R., & Barone, J. R. (2017). Wheat Gluten Aggregates as a Reinforcement for Poly (vinyl alcohol) Films. *ACS Sustainable Chemistry & Engineering*, *6*(2), 2422-2430.

ACS Sustainable Chemistry & Engineering

Research Article

Cite This: ACS Sustainable Chem. Eng. 2018, 6, 2422−2430

# Wheat Gluten Aggregates as a Reinforcement for Poly(vinyl alcohol) Films

Barbara L. DeButts,[†,‡,§] Cara R. Spivey,[∥] and Justin R. Barone*[,‡,§,∥,⊥]

[†]Macromolecular Science and Engineering and [‡]Macromolecules Innovation Institute, Virginia Tech, ICTAS II, 240 West Campus Drive, Blacksburg, Virginia 24060, United States

[§]Biological Systems Engineering and [∥]NSF RET: Biomechanics from molecular to organismal scales, Biological Systems Engineering, Virginia Tech, 301D Human and Agricultural Biosciences Building 1, 1230 Washington Street SW, Blacksburg, Virginia 24061, United States

[⊥]Center for Soft Matter and Biological Physics, Department of Physics, Virginia Tech, 850 West Campus Drive, Blacksburg, Virginia 24061, United States

Supporting Information

**ABSTRACT:** Dispersion of fillers in polymers is problematic, particularly nanofillers that prefer to agglomerate. Here, in-situ filler formation is demonstrated where a protein aggregate forms in a biodegradable polymer matrix via a low-energy solution incubation method. Wheat gluten protein molecules are dispersed in aqueous poly(vinyl alcohol) (PVA), and then cooperatively self-assemble into anisotropic structures. The tensile modulus of the composite films is up to 241% higher than the PVA controls, and the composite glass transition temperature ($T_g$) is increased by up to 12.1 ± 1.6 °C. Thermal processing for long times under increasing pressure can encourage protein aggregation into well-defined structures. However, the PVA phase is degraded by severe thermal processing, as evidenced by thermogravimetric analysis (TGA), Fourier transform infrared spectroscopy (FTIR), and modulus reduction. β-Sheet formation in the protein phase is observed with FTIR, indicating that the protein structures are amyloids.

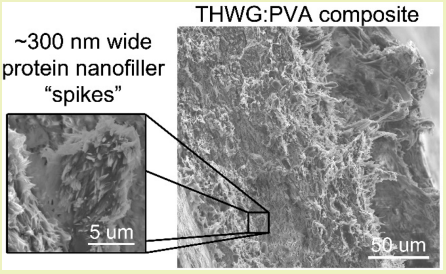


**KEYWORDS:** *Composite, Biobased, Mechanical properties, Molecular structure, Thermal properties*

## INTRODUCTION

It is very straightforward to self-assemble protein molecules into various structures in aqueous solution.[1,2] One self-assembly route is to form an amyloid, where the protein molecules unfold and hydrogen bond to form β-sheets with a protein interchain distance of about 0.48 nm.[1,3,4] β-Sheet formation in aqueous solution is thermodynamically driven by the packing of hydrophobic groups on amino acid side chains.[5−8] Many different proteins can be hydrolyzed or denatured to form β-sheet-containing amyloids.[7−13]

Amyloid protofibrils are formed when protein molecules continue to self-assemble into anisotropic structures.[14] Amyloids are commonly associated with pathological disorders such as neurodegenerative and prion diseases.[12,13] However, in certain living systems, amyloids protect and proliferate life.[14,15] Nondisease related, or "functional," amyloids in barnacle cement and fungi improve adhesion and biofilm formation, respectively.[15,16] The β-sheet phase endows these materials with rigidity and toughness because of nanoscale modification. Theoretical predictions of protein self-assembly through noncovalent, nonionic interactions, i.e., hydrogen bonding only, yield structures with elastic moduli of 10−20 GPa.[14] Experimental results approach these values and show amyloid formation to be a highly evolved process, even when replicated in vitro.[14,17−19] Thus, incorporating self-assembled amyloids into engineered materials such as films, adhesives, and composites is of substantial interest in sustainable technology.[14,20]

Enzyme-mediated hydrolysis of wheat gluten (WG) has been shown to promote amyloid formation. Unlike the full WG protein, the short glutamine-rich peptides produced from trypsin hydrolysis of WG can self-assemble at mild denaturing conditions into β-sheets.[21,22] Previous studies have shown that self-assembly could occur at near-physiological conditions of 37 °C and pH 8, which were good conditions to perform the enzymatic hydrolysis in a repeatable manner.[23] At pH 8, WG was hydrolyzed by trypsin enzyme into smaller, more uniform peptides of primarily ≤10 kDa molecular weight, with some residual 29 and 37 kDa fragments.[21,24] The peptide bonds in the component proteins of WG, i.e., gliadin (Gd) and low and high molecular weight glutenin (GtL and GtH), are preferentially cleaved by trypsin enzyme at arginine (R) and/or lysine (K) amino acids (Gd, UniProt P04721, 0.49 mole fraction; GtL, UniProt P10386, 0.45 mole fraction; GtH,

Received: October 24, 2017
Revised: December 13, 2017
Published: December 15, 2017

UniProt P08488, 0.06 mole fraction).[23] Since aggregation into β-sheets occurs in solution, the reduction in peptide molecular weight is important to help solubilize the protein.[25]

WG is low cost, has good film forming ability and oxygen barrier properties, and has been explored as a biodegradable packaging material.[26] WG can be compression molded, which encourages hydrophobic interactions and can induce aggregation and cross-linking, thereby increasing tensile strength while lowering elongation to break.[27−29] A fully self-assembled WG composite film was produced by incubating THWG at 37 °C to form short amyloid fibers which, when dried, reinforced the remaining unassembled THWG polymer matrix.[30] Poly(vinyl alcohol) (PVA) is a water-soluble and biodegradable polymer with good gas barrier properties, which has been reinforced with biological fillers to create sustainable, environmentally friendly composite films.[31−34] Poly(vinyl alcohol) films and composites can be used in multilayer packaging applications. In a multilayer film, a vinyl alcohol polymer layer is typically used as a core layer between polyolefin layers.[35] The function of the vinyl alcohol core is to act as a gas barrier, while the polyolefin layers serve to support the brittle vinyl alcohol layer and act as water barriers.[36] Introducing nanofillers can further improve the gas barrier properties of PVA by creating a tortuous diffusion pathway.[37] To reduce the brittleness of WG and/or PVA films, a plasticizer, such as glycerol, is commonly added.[38,39] WG has been blended with PVA to form compression-molded films.[40,41] However, these blends have used full WG proteins mixed with PVA to form a WG/polymer powder.

There are a few reports of amyloid protofibril reinforcement of polymers in the literature. One study details the lysozyme protein protofibril reinforcement of cross-linked polydimethylsiloxane (PDMS).[39] At low filler concentrations (2 wt %), amyloids showed equal reinforcement to carbon nanotubes (CNT). Another study described the lysozyme protofibril reinforcement of poly(lactic acid) (PLA) at 1−5 wt % amyloid.[40] Modulus and strain to break increased as a function of amyloid content. In another report, insulin amyloid protofibrils were added to aqueous poly(vinyl alcohol) (PVA) solutions, and then the water was evaporated.[41] The resulting 0.6 wt % amyloid−PVA nanocomposites were 15% stiffer than PVA. In each case, amyloid protofibrils were preformed in solution, and then isolated and mixed into the polymer to form the nanocomposite.

Here, in-situ filler formation was demonstrated where the protein nanofiller formed in an aqueous PVA solution. Hydrolyzed wheat gluten proteins were dispersed in aqueous PVA, and then cooperatively self-assembled into amyloid structures. The resulting films were thermally processed by compression molding and the thermal, mechanical, structural, and morphological properties of the films were characterized.

## EXPERIMENTAL SECTION

**Materials.** Wheat gluten (WG) was purchased from MP Biomedicals, LLC, (Solon, OH). Low weight-average molecular weight ($M_w$ ~ 31 kDa) and high weight-average molecular weight ($M_w$ ~ 67 kDa) poly(vinyl alcohol) (PVA, 86.7−88.7 mol % hydrolysis), and trypsin enzyme (type I from bovine pancreas), were purchased from Sigma-Aldrich (St. Louis, MO).

**Protein Hydrolysis and Composite Formation.** WG (20 g) was dispersed in distilled water (800 mL) while rapidly stirring at 250 rpm at 37 °C. The stirring speed was reduced to 50 rpm and trypsin enzyme (0.3 g) was added at a 1:67 w/w enzyme to substrate ratio. The dispersion was maintained at 37 °C and pH 8 with NaOH (1 or 4 M) and HCl (1 M) for 72 h to hydrolyze the protein. THWG dispersions were poured into aqueous solutions of PVA (20 g in 800 mL) at a 1:2 wt/wt protein to polymer ratio (33 wt % THWG). The THWG/PVA aqueous dispersions were incubated for 33 days at 37 °C and pH 8, and then poured into polytetrafluoroethylene (PTFE)-coated aluminum containers and incubated in the oven for 5 days at 40 °C. The 33-day incubation period was chosen to compare to previous results that characterized the aggregation of the same hydrolyzed proteins in purely aqueous solution.[42] On day 38, the containers were removed to dry at 22 °C and 16% relative humidity under a Supreme Air LV fume hood (Kewaunee Scientific Corp. Siemens Building Technologies, Inc., Buffalo Grove, IL) until solid films measuring 100 × 60 × 1 mm were obtained.

Dried 33 wt % THWG composites were compression molded to improve film uniformity for mechanical testing and to study the composite behavior during processing. The films were compression molded at 120 °C on an Auto Series hydraulic laboratory press (Carver, Wabash, IN) for (1) 10 min at 1.85 MPa pressure ("M10" conditions) or (2) "M10" plus 5 min at 2.59 MPa, and then an additional 5 min at 3.34 MPa pressure ("M20" conditions). Higher pressure was required to achieve uniform tensile specimens.

**Tensile Testing.** Tensile testing was performed on a TA.HD.*plus* Texture Analyzer (Texture Technologies Corp., Scarsdale, NY) with self-tightening crosshatched grips and a 100-kg load cell. Straight specimens (10 × 100 × 1 mm) were uniaxially deformed at a rate of 12.5 mm/min with a grip separation of 60 mm, as specified in ASTM D882. Average Young's modulus ($E$), ultimate tensile strength (UTS), and elongation to break (EB) values with standard error were determined from a sample size of five. Linear regression analysis of the linear portion of the stress−strain plots in Excel was used to calculate $E$.

**Fourier Transform Infrared (FTIR) Spectroscopy.** Protein−PVA films were vacuum-dried for 3 days at room temperature (RT). Attenuated total reflectance (ATR) FTIR spectra of the composites were recorded on a Thermo Nicolet 6700 FTIR spectrometer with a Smart Orbit ATR diamond crystal (Thermo Fisher Scientific Inc., Madison, WI) with 128 scans at a 4 $cm^{-1}$ resolution from 4000 to 525 $cm^{-1}$. Spectra were baseline corrected and analyzed using OMNIC v8.1 software.

**Scanning Electron Microscopy with Energy Dispersive X-ray Spectroscopy (SEM−EDX).** Tensile fracture surfaces were sputter coated with 5 nm of iridium and imaged using a FEI Quanta 600 FEG environmental SEM equipped with a Bruker EDX silicon drifted detector (Thermo Fisher Scientific, Waltham, MA). Micrographs were obtained with a 12.4 mm working distance and 10 kV accelerating voltage. Nitrogen was exclusive to the protein phase, and high contrast areas in the nitrogen elemental maps were used to identify the morphology of the protein aggregates. Due to beam limitations, protein aggregates smaller than 1 $\mu m^2$ could not be resolved. A smooth map filter was applied to the elemental maps by Bruker Quantex 400 Esprit 1.9 collection software.

**Differential Scanning Calorimetry (DSC).** A heat−cool−heat cycle between −10 and 210 °C at 10 °C/min was performed in triplicate on compression-molded samples (~9 mg, Q200 DSC, TA Instruments, New Castle, DE) in a nitrogen atmosphere. The thermal transitions were determined from the second heating cycle using Universal Analysis software (TA Instruments). The percent crystallinity of the PVA phase ($X_c$) was calculated from

$$X_c = \frac{\Delta H_f}{m_{PVA}\Delta H_f^\circ} \quad (1)$$

where $\Delta H_f$ is the experimental heat of fusion, $m_{PVA}$ is the mass fraction of PVA in the composite, and $\Delta H_f^\circ$ = 150 J/g is the theoretical heat of fusion of 100% crystalline PVA.[43,44]

**Thermogravimetric Analysis (TGA).** Samples (10−12 mg) were heated at 10 °C/min from RT to 600 °C in a nitrogen atmosphere on a TA Instruments SDT-Q600 simultaneous TGA/DSC (New Castle, DE). A graph of weight loss versus temperature and the first derivative


DOI: 10.1021/acssuschemeng.7b03872
ACS Sustainable Chem. Eng. 2018, 6, 2422−2430

**Table 1. Tensile and Thermal Properties for PVA Controls and THWG:PVA Composite Compression Molded Films[a]**

| name | $E$ (MPa) | UTS (MPa) | EB (%) | $T_g$ (°C) | $T_m$ (°C) | $X_c$ (%) |
|---|---|---|---|---|---|---|
| PVA ($M_w$ 67 kDa)-M10 | 140.0 ± 2.5 | 7.9 ± 0.5 | 64.6 ± 7.6 | 63.6 ± 1.4 | 215.0 ± 1.7 | 21.8 ± 4.1 |
| THWG:PVA ($M_w$ 67 kDa)-M10 | 478.2 ± 28.0 | 8.7 ± 1.2 | 10.8 ± 2.2 | 75.7 ± 0.8 | 217.3 ± 0.4 | 26.1 ± 0.8 |
| PVA ($M_w$ 67 kDa)-M20 | 106.9 ± 8.6 | 11.0 ± 0.8 | 92.5 ± 16.2 | 65.2 ± 0.9 | 213.7 ± 0.3 | 25.0 ± 3.3 |
| THWG:PVA ($M_w$ 67 kDa)-M20 | 297.1 ± 33.9 | 7.4 ± 0.2 | 9.9 ± 1.2 | 68.0 ± 1.3 | 216.4 ± 0.5 | 28.2 ± 4.4 |
| PVA ($M_w$ 31 kDa)-M20 | 216.9 ± 9.4 | 9.0 ± 0.3 | 21.7 ± 2.1 | 63.9 ± 0.7 | 215.5 ± 0.4 | 24.9 ± 4.2 |
| THWG:PVA ($M_w$ 31 kDa)-M20 | 411.0 ± 23.6 | 8.5 ± 0.4 | 7.5 ± 0.7 | 69.7 ± 0.6 | 214.6 ± 0.4 | 33.7 ± 6.6 |

[a]Thermal properties were calculated from the second heating cycle after rapid cooling. Young's modulus ($E$), ultimate tensile strength (UTS), elongation to break (EB), midpoint glass transition temperature ($T_g$), peak melting temperature ($T_m$), and percent crystallinity ($X_c$) values are given as the mean ± standard error.

of weight loss with respect to temperature ($dW/dT$) versus temperature was generated by Universal Analysis software.

## RESULTS AND DISCUSSION

**Thermal and Mechanical Properties.** The tensile and thermal properties of the controls and composites as a function of compression molding conditions and PVA molecular weight are given in Table 1. The glass transition temperature ($T_g$), melting temperature ($T_m$), and percent crystallinity ($X_c$) were calculated from the second heating cycle and reflect the material properties rather than the processing history (Figures S1 and S2). At 33 wt % THWG protein filler, the composites demonstrated Young's modulus ($E$) increases of 89−241% and $T_g$ increases of 2.8 ± 1.6 to 12.1 ± 1.6 °C over the controls (Table 1). The increase in modulus was at the expense of elongation to break (EB), i.e., flexibility, which decreased from 14.2 ± 2.9 to 82.6 ± 21.0% depending on the processing parameters, which is typical behavior for reinforced polymer composites. These results were similar to those obtained in studies for PVA mixed with other biological fillers, such as fish myofibrillar protein,[45,46] algae,[47] and chitosan.[48] The films reported here attained similar $E$ increases to PVA reinforced with 10−20 wt % nanofibrillated cellulose (2.5−3-fold increased in $E$), despite the fact that the theoretical modulus of a cellulose crystal (130−250 GPa) is much higher than that of a $\beta$-sheet ($E$ = 22−36 GPa).[49−51] The addition of protein increased the $T_g$ of PVA, which signified decreased PVA molecular mobility possibly from THWG−PVA hydrogen bonding interactions because PVA has been shown to hydrogen bond to other biobased materials and wheat gluten.[52−54] The $T_g$'s of the films reported here were similar to those obtained by Maria et al.[55] for solution-cast films of gelatin:PVA blends of variable PVA molecular weight. The protein had little effect on the crystallinity of PVA, and the $T_m$ and $X_c$ of the composites were close to or within standard error of the controls. As shown by the derivative of the weight loss in TGA, the onset of primary PVA degradation shifted to a lower temperature in the composites (Figure 1). Since PVA degrades shortly after melting, any decrease in degradation temperature reduces the processability of PVA.[56]

The 67 kDa PVA films were subjected to moderate compression molding time and pressure, i.e., M10, and severe compression molding time and pressure, i.e., M20, conditions, as specified in the Experimental Section. In the PVA(67 kDa)-M10 and -M20 controls, increased molding time and pressure had no effect on the thermal transitions of the material; i.e., the difference of means for $T_g$, $T_m$, and $X_c$ were within standard error (Table 1). However, the mechanical properties of the high molecular weight PVA controls were altered. Ultimate tensile strength (UTS) increased by 3.1 ± 1.2 MPa and

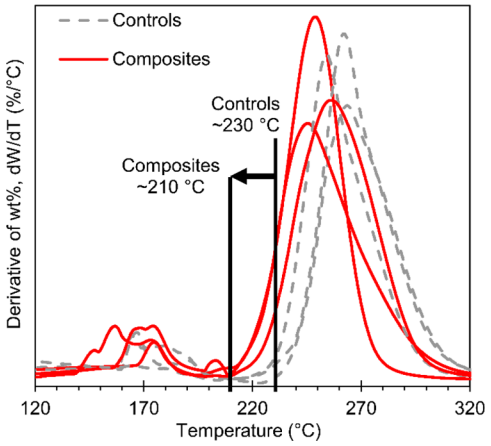


**Figure 1.** Graph of the first derivative of weight loss with respect to temperature ($dW/dT$) vs temperature. TGA data depicts the major degradation events for the PVA controls (dashed lines) and THWG:PVA composites (solid lines).

elongation to break (EB) increased by 27.9 ± 23.1%, while modulus decreased by 33.1 ± 11.5 MPa (~24%) (Table 1). The decreased modulus, combined with increased UTS and EB, indicated that compression molding improved PVA flexibility.[57] Greater weight loss was observed in the PVA(67 kDa) controls as molding time and pressure increased (Table 2), indicating that the thermal stability of PVA was

**Table 2. TGA Weight Loss Data for PVA Controls and THWG:PVA Composites for Two Isolated Temperature Ranges**

| | weight loss (%) | |
|---|---|---|
| sample | 20−200 °C | 200−320 °C |
| PVA(67 kDa)-M10 control | 10.8 | 45.6 |
| THWG:PVA(67 kDa)-M10 | 9.9 | 48.4 |
| PVA(67 kDa)-M20 control | 14.6 | 49.8 |
| THWG:PVA(67 kDa)-M20 | 15.2 | 48.3 |
| PVA(31 kDa)-M20 control | 16.9 | 45.7 |
| THWG:PVA(31 kDa)-M20 | 10.7 | 51.4 |

compromised by extensive compression molding and PVA degradation occurred.[56] Typically, PVA degradation below $T_m$ ~ 200 °C occurs via water elimination from the hydroxyl side groups, while degradation above $T_m$ occurs via chain scission.[58]

The largest modulus increase of 338.2 ± 36.2 MPa (+241% over the PVA control) was observed in the composite molded for less time and pressure, i.e., THWG:PVA(67 kDa)-M10. This composite exhibited the highest $T_g$ of 75.7 ± 0.8 °C and greatest increase in $T_g$ over the control (+12.1 ± 1.6 °C), but


DOI: 10.1021/acssuschemeng.7b03872
ACS Sustainable Chem. Eng. 2018, 6, 2422−2430

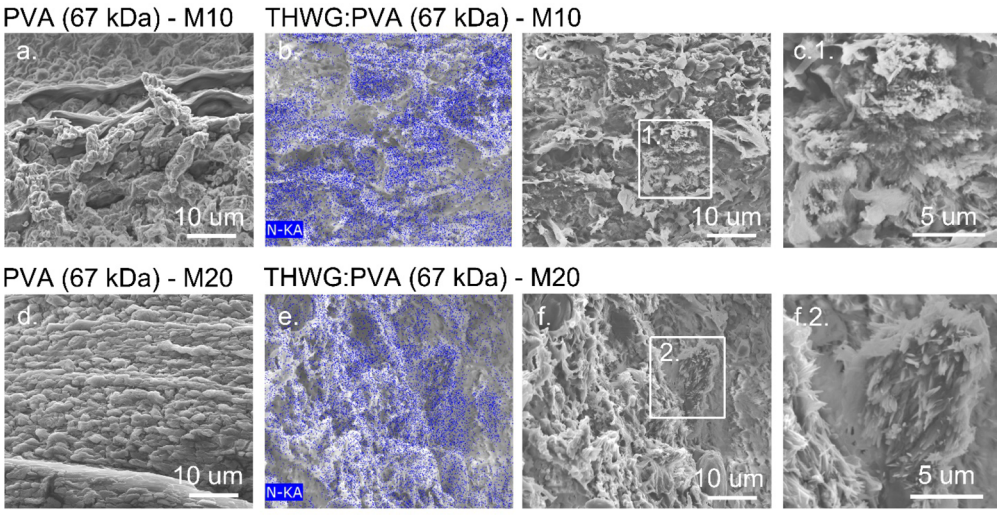


**Figure 2.** (a) SEM of PVA(67 kDa)-M10 control. (b) SEM−EDX and (c) SEM of THWG:PVA(67 kDa)-M10 composite showing protein dispersion in blue and protein aggregate morphology (inset, c1). (d) SEM of PVA(67 kDa)-M20 control. (e) SEM−EDX and (f) SEM of THWG:PVA(67 kDa)-M20 composite showing protein dispersion in blue and development of protein aggregate morphology with additional compression molding (inset, f1). All SEM−EDX images show nitrogen distribution.

similar $T_m$ and $X_c$ to the control. As molding progressed from M10 to M20 conditions, the THWG:PVA(67 kDa) composite modulus decreased by 181.1 ± 56.8 MPa (−38%), while UTS and EB were unaffected. Similarly, there was a significant decrease in $T_g$ of 7.7 ± 1.5 °C with composite compression molding, while $T_m$ and $X_c$ for THWG:PVA(67 kDa)-M10 and -M20 were unaffected. The decrease in $T_g$ with compression molding was only observed for the 67 kDa PVA composites, and implied a decrease in protein−PVA, i.e. hydrogen bonding, interactions, with molding. Generally, high temperatures (>70 °C), high pressures (>200 MPa), and/or long times (>10 min) can induce conformational changes in gliadins and rearrangement of intrachain disulfide bonds into interchain disulfide bonds, i.e., induce cross-linking.[59] Temperature and pressure affect noncovalent bonds differently; hydrogen bonds are thermally labile, but need more pressure to break than weaker hydrophobic interactions, which increase with temperature and are easily broken under pressure.[60] At the relatively low pressures (1.85−3.34 MPa) and high temperature (120 °C) used, it was likely that rearrangements in hydrogen bonding occurred, while the hydrophobic interactions governing protein aggregation, i.e., protein−protein interactions, were increased with compression molding. Dicharry et al.[40] hypothesized that strong interactions of a phase with itself came at the expense of interactions between phases, which caused a decrease in the mechanical properties of the blend. Thus, as THWG−THWG interactions increased, protein−PVA interactions decreased, which reduced the modulus. The modulus decrease in the composites was greater (−38%) than in the controls (−24%), which supported protein−PVA interactions as the origin of reinforcement. The weight loss between 20 and 200 °C was similar for the 67 kDa PVA controls and composites, which indicated that degradation primarily occurred in the PVA phase and increased with processing, i.e., from M10 (∼10% weight loss) to M20 (∼15% weight loss) molding conditions (Table 2). Although protein degradation into low-molecular-weight fragments has been shown to result from thermomolding for long times (15−25 min) at temperatures of 170 °C,[61] this was greater than the processing temperature of 120 °C used here.

PVA molecular weight influenced composite properties. At constant M20 molding conditions, it was found that the 31 kDa PVA control outperformed the 67 kDa PVA control in terms of modulus, but exhibited lower UTS and EB (Table 1). Limpan et al.[46] reported a similar result for solution-cast PVA films with a high degree of hydrolysis (DH, 98.5−99.2%). The authors tested films of comparable molecular weights to the PVA films studied here, i.e., 22−27 and 75−80 kDa, and found that the lower molecular weight PVA film had a higher modulus, but lower UTS and EB. Similarly, Dicharry et al.[40] tested compression-molded thiolated PVA (TPVA)−WG blends using PVA of $M_w$ 2, 9.5, 50, and 205 kDa. At the highest TPVA loading of 40 wt %, which was most comparable to the blend ratio studied here, the authors found that the midmolecular weight PVA ($M_w$ 50 kDa) had the highest modulus. The THWG:PVA(31 kDa)-M20 composite exhibited a greater $T_g$ increase (+5.8 ± 0.9 °C) over the control than the 67 kDa PVA composite (+2.8 ± 1.6 °C, Table 1). An increase in protein−PVA hydrogen bonding could have contributed to the $T_g$ increase. The 31 kDa composite also had greater PVA thermal stability. From 20 to 200 °C, THWG: PVA(31 kDa)-M20 had less weight loss than the control (Table 2). This was the only composite to significantly improve PVA thermal stability over the control for any temperature range. Similarly, Cano et al.[62] found that the thermal stability of PVA was improved for some starch−PVA biocomposite blends. However, between 200 and 320 °C it had the highest weight loss of any sample, with a maximum rate of weight loss occurring at ∼255 °C.

**Composite Morphology.** The morphology of the fracture surface after uniaxial deformation was examined as a function of thermal processing (Figure 2). The protein phase appeared as bright colored areas in the SEM−EDX nitrogen maps, where regions of amorphous, unassembled protein and regions of structured protein are visible (Figure 2b,c,e,f). Good adhesion between the protein and PVA phases was observed, although there was some evidence of THWG-rich and PVA-rich domains forming on the micrometer scale. Within the THWG-rich domains, short, anisotropic aggregates were mixed with larger, well-defined "spikes" in the THWG:PVA(67 kDa)-


DOI: 10.1021/acssuschemeng.7b03872
ACS Sustainable Chem. Eng. 2018, 6, 2422−2430

M10 composite. The spikes were wide, flat, and pointed on the end, measuring hundreds of nanometers wide at most (Figure 2c.1). As molding time and pressure increased, larger, well-defined spikes appeared that were 270−405 nm wide (Figure 2f.2). The THWG:PVA(67 kDa)-M20 composite displayed many well-defined spikes, suggesting that thermal processing under pressure allowed for more protein aggregation. It has been shown that processing proteins with heat, pressure, and dehydration can encourage aggregation by destabilizing the protein molecules and exposing hydrophobic surfaces.[40,52,63] The spikes observed in Figure 2f.2 were approximately the same width as the spikes observed in Meyer et al.,[64] while the spikes in Figure 4b.1,b.2 were thinner with a width of ca. 120 nm.[65]

Although protein assembly into well-defined anisotropic structures increased with processing, the composite modulus decreased. It was possible that the protein aggregation phenomenon, i.e., an increase in THWG−THWG interactions, caused a decrease in THWG−PVA interactions and, consequently, reduced the modulus.[40] Or, that the smaller nanostructures observed in the THWG:PVA(67 kDa)-M10 composite were better at reinforcement. SEM−EDX of the same fracture surface shown in Figure 2 depicts a large protein agglomerate in THWG:PVA(67 kDa)-M20 that lacked the anisotropic protein structures observed elsewhere in the fracture surface (Figure 3). These large protein agglomerates may not contribute to the modulus in the same way as smaller, more well-defined anisotropic structures.

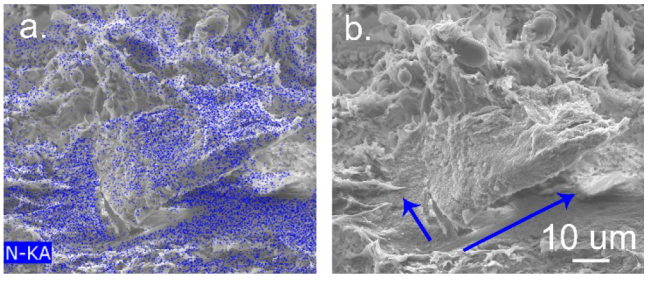


**Figure 3.** (a) SEM−EDX identifying the protein phase in blue for THWG:PVA(67 kDa)-M20 composite. (b) SEM showing the fracture behavior of a large protein agglomerate.

For the THWG:PVA(31 kDa)-M20 composite, dense agglomerates of radially oriented spikes were observed (Figure 4). The agglomerates formed THWG-rich domains measuring tens of micrometers, which were larger than the THWG domains in THWG:PVA(67 kDa)-M20 (Figure 4b compared to Figure 2f). The agglomerates were broken in the fracture plane indicating adhesion between the protein and the 31 kDa PVA and visual evidence of protein−PVA bonding interactions (Figure 4b). Some of the agglomerates had pulled away from the PVA matrix, but others had not. These protein agglomerates resembled amyloid protein "pompons" observed in early stage aggregation in vivo.[63] It is not clear why individual spikes, and then pompons, form in early stage protein aggregation in vivo, nor why the in vitro aqueous PVA environments studied here also exhibited spikes and pompons rather than the long, anisotropic fibrils usually observed for in vitro protein aggregation in aqueous solution. It could be that the in vitro aqueous PVA environment mimicked an in vivo environment. In any case, there was a clear trend: (1) a 67 kDa PVA environment resulted in short, anisotropic aggregates that

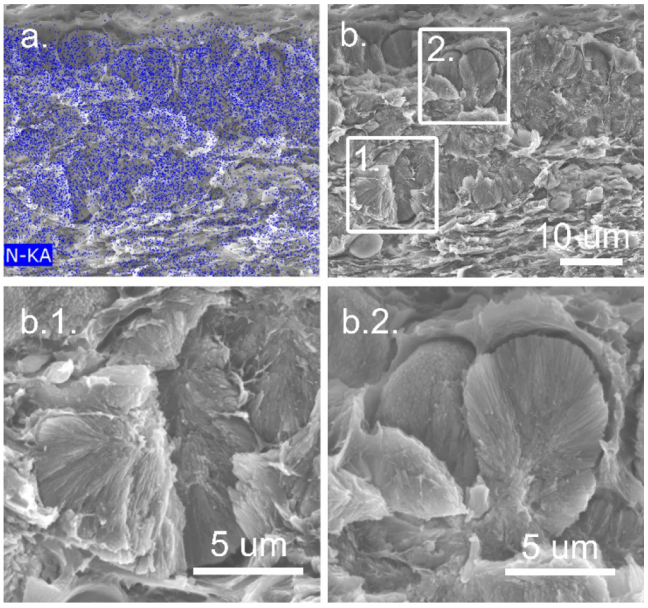


**Figure 4.** (a) SEM−EDX showing protein dispersion in blue for THWG:PVA(31 kDa)-M20. The PVA(31 kDa)-M20 control (not shown) is comparable to Figure 3d. (b) SEM of THWG:PVA(31 kDa)-M20 with protein aggregate "pompon" morphology (inset, b1 and b2).

developed into spikes and agglomerates of spikes with increased thermal processing (M10 vs M20, Figure 2) and, (2) when processed under M20 conditions, a 67 kDa PVA environment resulted in wide, partially agglomerated spikes (Figure 2f), while a 31 kDa PVA environment resulted in thinner spikes that aggregated into dense pompons (Figure 4b). The agglomeration of spikes into dense pompons in THWG:PVA(31 kDa)-M20 may have enhanced thermal stability between 20 and 200 °C. Aggregated proteins have been shown to be thermally stable.[40,66] It appeared that the increase in PVA molecular weight to 67 kDa prevented spike agglomeration into pompoms within the time frame of the experiment.

Given the size of the observable protein structures, the SEM images supported the hypothesis that a THWG protein phase could self-assemble in a PVA polymer matrix. While the exact mechanism of amyloid formation is a subject of much debate, the generally accepted theory is that amyloid formation is a cooperative and hierarchical process which follows an entropy-driven nucleation and growth mechanism.[67] Thus, parameters which alter the protein concentration and self-assembly kinetics are important factors for controlling the final aggregate morphology.[68,69] In this work, both PVA molecular weight and compression molding at elevated temperatures influenced the protein aggregate self-assembly. An increase in PVA molecular weight appeared to decrease the self-assembly kinetics, perhaps by reducing protein mobility through a highly entangled polymer phase. This resulted in individual, anisotropic nanostructures with good adhesion to the PVA phase and a high composite modulus. Continued compression molding at elevated temperatures favored protein aggregation into large agglomerates, which decreased modulus. These results presented a simple way to limit aggregation of protein nanostructures into agglomerates, i.e., by decreasing thermal processing and increasing polymer molecular weight, thus maximizing protein reinforcement.


DOI: 10.1021/acssuschemeng.7b03872
ACS Sustainable Chem. Eng. 2018, 6, 2422−2430

**Molecular Structure.** The FTIR spectra of the PVA controls conditioned at 23% relative humidity (RH), i.e., were normalized to the absorbance of the PVA methylene scissoring mode, $\delta(CH_2)$.[70−73] In the processed PVA controls $\delta(CH_2)$ occurred at 1403 $cm^{-1}$, and in the as-received PVA(67 kDa) it occurred at 1429 $cm^{-1}$. The as-received PVA was included to show the PVA structural changes with processing (Figure 5).

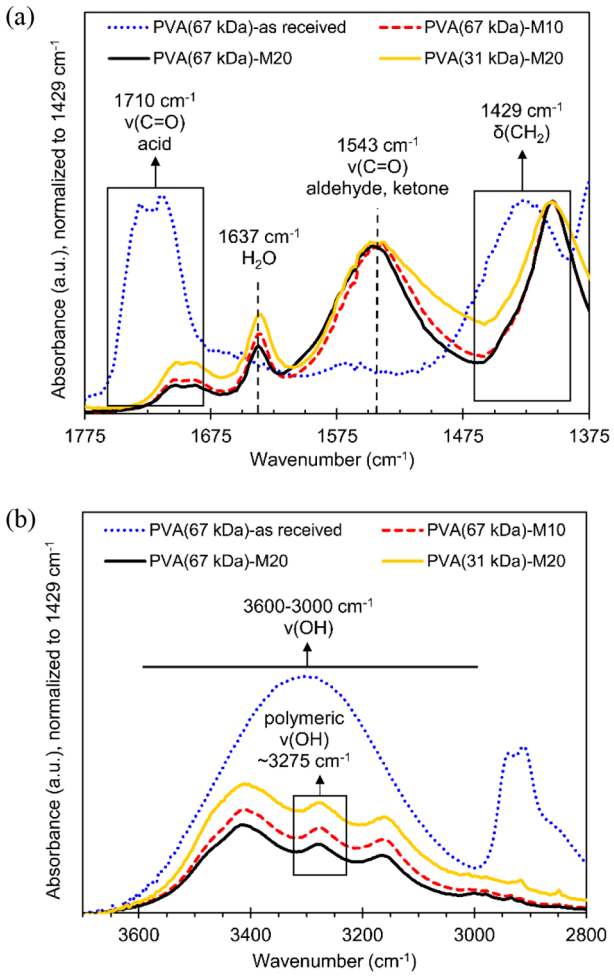


**Figure 5.** FTIR spectra for as-received PVA and the thermally processed PVA controls, comparing (a) stretching ($\nu$) and bending ($\delta$) modes for functional groups in the fingerprint region and (b) the hydrogen bonding region. Spectra normalized to the methylene bending mode, $\delta(CH_2)$, at 1429 $cm^{-1}$ (as-received) or 1403 $cm^{-1}$ (processed controls).

The major absorbances and assignments for the PVA FTIR spectrum are given in Figure 5.[71,72] Thermomechanical processing is known to degrade PVA, particularly in the absence of a plasticizer, and degradation can be identified in FTIR.[74] Degradation of the PVA phase was observed in two regions: (1) as a decreased absorbance and shifting in the $\nu$(OH) region (3600−3000 $cm^{-1}$) and (2) as a new absorbance at 1543 $cm^{-1}$. The $\nu$(OH) absorbance decreased with processing, indicating a loss of PVA hydroxyl groups as the origin of degradation (Figure 5b).[71] The central absorbance in the hydrogen bonding region shifted from 3270 $cm^{-1}$ in PVA(67 kDa)-M10 to 3278 $cm^{-1}$ in PVA(67 kDa)-M20, indicating a loss of PVA−PVA hydrogen bonding with processing.[71,73,75,76] All the changes in the hydrogen bonding region were characteristic of water loss. A new absorbance at 1543 $cm^{-1}$ was observed in the thermally processed PVA samples and assigned to the aldehyde and ketone degradation products of PVA.[58,75,76] The $\nu$(C═O) absorbance at ca. 1700 $cm^{-1}$ was assigned to residual acetate groups.[72,77] This absorbance was greatly reduced and shifted to a lower wavenumber in the thermally processed PVA samples, indicating continued hydrolysis of the as-received PVA, which was 88% hydrolyzed.[78,79] Compared to PVA(67 kDa)-M20, intermolecular hydrogen bonding was stronger in the PVA(31 kDa)-M20 control, observable as a shift of the $\nu$(OH) central absorbance to a lower wavenumber (3274 $cm^{-1}$) and as an increased absorbance area. This implied that stronger PVA−PVA hydrogen bonding was the origin of the modulus increase in the lower molecular weight PVA control.

To isolate the protein amide I region (1700−1600 $cm^{-1}$, $\nu$(C═O)) from the water contribution (1637 $cm^{-1}$, $\nu$(OH)), the samples were dried in vacuo for 3 days (Figure 6) and the FTIR spectra were normalized to the methylene rocking mode, $\gamma_r(CH_2)$, from 916 to 924 $cm^{-1}$, which was a region where the protein did not show significant absorbance.[72] Due to the similarity of the functional groups in PVA and THWG, the spectra were normalized based upon weight percent, where the controls had a maximum normalized absorbance of 67 wt %, THWG at 33 wt %, and the composites at 100 wt %. Fully aggregated THWG, self-assembled in aqueous solution, is given for reference. A water peak was observed in PVA(31 kDa)-M20 after vacuum drying. The absorbance at 1620 $cm^{-1}$ was characteristic of high-density $\beta$-sheet formation in THWG (Figure 6a).[42] As evidenced by the normalized 1620 $cm^{-1}$ absorbance in the amide I region, THWG can hydrogen bond to form $\beta$-sheets in water and in aqueous PVA solutions. The relative $\beta$-sheet content in the composites, quantitatively described by the normalized absorbance at 1620 $cm^{-1}$,[42,78] reflected the changes observed in SEM. The amide I region increased in absorbance and shifted to lower wavenumbers from THWG:PVA(67 kDa)-M10 to -M20, suggesting stronger $\beta$-sheet formation and hydrogen bonding in the aggregated protein phase with processing. The smallest amide I absorbance was observed in the low molecular weight composite, THWG:PVA(31 kDa)-M20, which was the composite with the smallest percent increase in modulus over the control. The trends were repeated in the hydrogen bonding region which, for the composites and THWG, included $\nu$(NH) contributions at ~3300 $cm^{-1}$ as well as $\nu$(OH) (Figure 6b).[80] Thus, the changes in the thermal and mechanical properties of the composites seemed to reflect changes in the PVA−protein interactions and the final protein aggregate size and morphology, as well as $\beta$-sheet content.

## CONCLUSIONS

Trypsin hydrolyzed wheat gluten (THWG) proteins were self-assembled in aqueous PVA solutions, and then the composite solutions were air-dried and compression molded into films. At 33 wt % THWG, the composites demonstrated elastic modulus increases of 89−241% over the controls. The addition of protein increased the PVA $T_g$. However, the onset of primary PVA degradation shifted to a lower temperature in the composites, suggesting protein compromised PVA thermal stability. As molding time and pressure increased from M10 to M20 conditions, the films exhibited earlier degradation. At constant molding conditions, the low molecular weight PVA composite, i.e., THWG:PVA(31 kDa)-M20, exhibited im-


DOI: 10.1021/acssuschemeng.7b03872
ACS Sustainable Chem. Eng. 2018, 6, 2422−2430

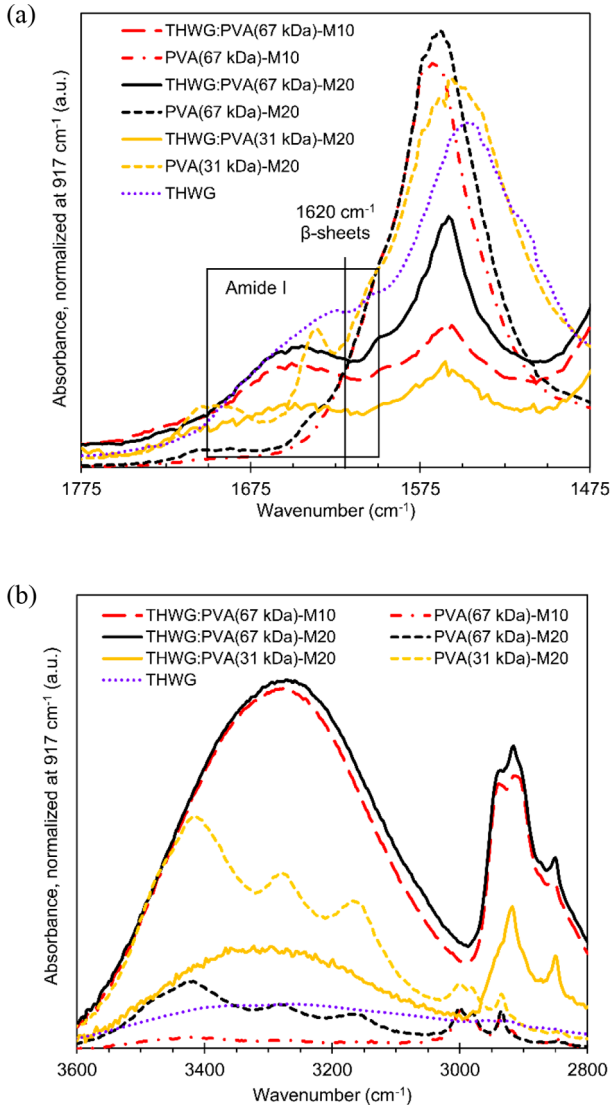


**Figure 6.** FTIR spectra normalized to the PVA methylene rocking mode, $\gamma_r(CH_2)$, at 917 $cm^{-1}$ for THWG:PVA composites, PVA controls, and neat THWG protein (dotted line). (a) Amide I region (inset, 1700−1600 $cm^{-1}$) is shown with a vertical line marking the high density $\beta$-sheet absorbance (1620 $cm^{-1}$). (b) Hydrogen bonding region, $\nu$(OH) and $\nu$(NH) (in the protein phase).

proved thermal stability from 20 to 200 °C compared to the control. Compression molding of the high molecular weight PVA composites, i.e., THWG:PVA(67 kDa), resulted in nanostructured anisotropic protein aggregates, which further aggregated into larger structures as molding time and pressure increased. The 31 kDa PVA composite resulted in nanoscale spikes which had densely aggregated into radially oriented micrometer-sized "pompon" structures. A greater processing time and pressure and/or a lower PVA molecular weight allowed for more protein aggregation. The larger protein structures provided less reinforcement, so these composites had a reduced modulus. Protein aggregates formed through a typical mechanism of $\beta$-sheet formation. The results showed an interesting concept: in-situ filler formation in polymer matrixes where the choice of polymer and processing conditions influenced the final morphology and composite properties.

## ■ ASSOCIATED CONTENT

### Supporting Information

The Supporting Information is available free of charge on the ACS Publications website at DOI: 10.1021/acssuschemeng.7b03872.

DSC second heat thermograms of PVA controls and 33% THWG:PVA composites comparing the effect of processing conditions at constant PVA molecular weight (Figure S1) and the effect of PVA molecular weight at constant processing conditions (Figure S2) on the thermal properties of the films (PDF)

## ■ AUTHOR INFORMATION


### Corresponding Author

*E-mail: jbarone@vt.edu.

### ORCID

Barbara L. DeButts: 0000-0002-7175-1069


### Author Contributions

The manuscript was written through contributions of all authors. All authors have given approval to the final version of the manuscript.


### Funding

This work was supported by the National Science Foundation Industry−University Cooperative Research Centers Program Center for Tire Research (NSF IUCRC CenTiRe) and the United States Department of Agriculture [Grant USDA-2016-67021-25006]. Cara Spivey performed parts of this research while participating in the NSF-Research Experience for Teachers (RET) program "Biomechanics from molecular to organismal scales" [Grant NSF-EEC-RET-1301037].


### Notes

The authors declare no competing financial interest.

## ■ ABBREVIATIONS

THWG:PVA, trypsin hydrolyzed wheat gluten in poly(vinyl alcohol); $T_g$, glass transition temperature; $T_m$, melting temperature; $\Delta H_f$, experimental heat of fusion; TGA, thermogravimetric analysis; DSC, differential scanning calorimetry; ATR FTIR, attenuated total reflectance Fourier transform infrared spectroscopy; SEM−EDX, scanning electron microscopy with energy dispersive X-ray spectroscopy; *E*, Young's modulus; UTS, ultimate tensile strength; EB, elongation to break; RT, room temperature; RH, relative humidity; PDMS, polydimethylsiloxane; CNT, carbon nanotubes; PLA, poly(lactic acid); PTFE, polytetrafluoroethylene

## ■ REFERENCES


(1) van Hest, J. C. M.; Tirrell, D. A. Protein-based materials, toward a new level of structural control. *Chem. Commun.* **2001**, 1897−1904.

(2) Ridgley, D. M.; Barone, J. R. Evolution of the amyloid fiber over multiple length scales. *ACS Nano* **2013**, *7*, 1006−1015.

(3) Sunde, M.; Serpell, L. C.; Bartlam, M.; Fraser, P. E.; Pepys, M. B.; Blake, C. C. F. Common core structure of amyloid fibrils by synchrotron X-ray diffraction. *J. Mol. Biol.* **1997**, *273*, 729−739.

(4) Makin, O. S.; Sikorski, P.; Serpell, L. C. Diffraction to study protein and peptide assemblies. *Curr. Opin. Chem. Biol.* **2006**, *10*, 417−422.

(5) Serpell, L. C.; Smith, J. M. Direct visualisation of the $\beta$-sheet structure of synthetic Alzheimer's amyloid. *J. Mol. Biol.* **2000**, *299*, 225−231.

(6) Adamcik, J.; Mezzenga, R. Adjustable twisting periodic pitch of amyloid fibrils. *Soft Matter* **2011**, *7*, 5437−5443.

(7) Eisenberg, D.; Weiss, R. M.; Terwilliger, T. C.; Wilcox, W. Hydrophobic moments and protein structure. *Faraday Symp. Chem. Soc.* **1982**, *17*, 109−120.
(8) Eisenberg, D.; Wilcox, W.; McLachlan, A. D. Hydrophobicity and amphiphilicity in protein structure. *J. Cell. Biochem.* **1986**, *31*, 11−17.
(9) Adamcik, J.; Jung, J.-M.; Flakowski, J.; De Los Rios, P.; Dietler, G.; Mezzenga, R. Understanding amyloid aggregation by statistical analysis of atomic force microscopy images. *Nat. Nanotechnol.* **2010**, *5*, 423−428.
(10) Fändrich, M.; Forge, V.; Buder, K.; Kittler, M.; Dobson, C. M.; Diekmann, S. Myoglobin forms amyloid fibrils by association of unfolded polypeptide segments. *Proc. Natl. Acad. Sci. U. S. A.* **2003**, *100*, 15463.
(11) Dunstan, D. E.; Hamilton-Brown, P.; Asimakis, P.; Ducker, W.; Bertolini, J. Shear flow promotes amyloid-$\beta$ fibrilization. *Protein Eng., Des. Sel.* **2009**, *22*, 741−746.
(12) Anand, G.; Sharma, S.; Dutta, A. K.; Kumar, S. K.; Belfort, G. Conformational Transitions of Adsorbed Proteins on Surfaces of Varying Polarity. *Langmuir* **2010**, *26*, 10803−10811.
(13) Sethuraman, A.; Vedantham, G.; Imoto, T.; Przybycien, T.; Belfort, G. Protein unfolding at interfaces: Slow dynamics of $\alpha$-helix to $\beta$-sheet formation. *Proteins: Struct., Funct., Genet.* **2004**, *56*, 669−678.
(14) Knowles, T. P. J.; Buehler, M. J. Nanomechanics of functional and pathological amyloid materials. *Nat. Nanotechnol.* **2011**, *6*, 469−479.
(15) Chiti, F.; Dobson, C. M. Protein misfolding, functional amyloid, and human disease. *Annu. Rev. Biochem.* **2006**, *75*, 333−366.
(16) Prusiner, S. B. Neurodegenerative diseases and prions. *N. Engl. J. Med.* **2001**, *344*, 1516−1526.
(17) Barlow, D. E.; Dickinson, G. H.; Orihuela, B.; Kulp, J. L., III; Rittschof, D.; Wahl, K. J. Characterization of the adhesive plaque of the barnacle *Balanus amphitrite*: Amyloid-like nanofibrils are a major component. *Langmuir* **2010**, *26*, 6549−6556.
(18) Gebbink, M. F. B. G.; Claessen, D.; Bouma, B.; Dijkhuizen, L.; Wosten, H. A. B. Amyloids-A functional coat for microorganisms. *Nat. Rev. Microbiol.* **2005**, *3*, 333−341.
(19) Adamcik, J.; Berquand, A.; Mezzenga, R. Single-step direct measurement of amyloid fibrils stiffness by peak force quantitative nanomechanical atomic force microscopy. *Appl. Phys. Lett.* **2011**, *98*, 193701.
(20) Adamcik, J.; Lara, C.; Usov, I.; Jeong, J. S.; Ruggeri, F. S.; Dietler, G.; Lashuel, H. A.; Hamley, I. W.; Mezzenga, R. Measurement of intrinsic properties of amyloid fibrils by the peak force QNM method. *Nanoscale* **2012**, *4*, 4426−4429.
(21) Athamneh, A. I.; Barone, J. R. Enzyme-mediated self-assembly of highly ordered structures from disordered proteins. *Smart Mater. Struct.* **2009**, *18*, 104024.
(22) Barone, J. R.; Athamneh, A. Large Self-Assembled Peptide Fibers. *MRS Online Proc. Libr.* **2011**, DOI: 10.1557/opl.2011.536.
(23) Ridgley, D. M.; Claunch, E. C.; Barone, J. R. The effect of processing on large, self-assembled amyloid fibers. *Soft Matter* **2012**, *8*, 10298−10306.
(24) Tuck, C. S.; Latham, A.; Lee, P. W.; Barone, J. R. Wheat Gluten Plasticized with Its Own Hydrolysate. *J. Polym. Environ.* **2014**, *22*, 430−438.
(25) Fändrich, M.; Dobson, C. M. The behaviour of polyamino acids reveals an inverse side chain effect in amyloid structure formation. *EMBO J.* **2002**, *21*, 5682−5690.
(26) Zubeldía, F.; Ansorena, M. R.; Marcovich, N. E. Wheat gluten films obtained by compression molding. *Polym. Test.* **2015**, *43*, 68−77.
(27) Sun, S.; Song, Y.; Zheng, Q. Morphologies and properties of thermo-molded biodegradable plastics based on glycerol-plasticized wheat gluten. *Food Hydrocolloids* **2007**, *21*, 1005−1013.
(28) Sun, S.; Song, Y.; Zheng, Q. Thermo-molded wheat gluten plastics plasticized with glycerol: effect of molding temperature. *Food Hydrocolloids* **2008**, *22*, 1006−1013.
(29) Gällstedt, M.; Mattozzi, A.; Johansson, E.; Hedenqvist, M. S. Transport and Tensile Properties of Compression-Molded Wheat Gluten Films. *Biomacromolecules* **2004**, *5*, 2020−2028.
(30) Claunch, E. C.; Ridgley, D. M.; Barone, J. R. Completely self-assembled fiber composites. *Compos. Sci. Technol.* **2015**, *117*, 1−8.
(31) Cheng, Q.; Wang, S.; Rials, T. G.; Lee, S.-H. Physical and mechanical properties of polyvinyl alcohol and polypropylene composite materials reinforced with fibril aggregates isolated from regenerated cellulose fibers. *Cellulose* **2007**, *14*, 593−602.
(32) Zhang, W.; Yang, X.; Li, C.; Liang, M.; Lu, C.; Deng, Y. Mechanochemical activation of cellulose and its thermoplastic polyvinyl alcohol ecocomposites with enhanced physicochemical properties. *Carbohydr. Polym.* **2011**, *83*, 257−263.
(33) Chiellini, E.; Corti, A.; D'Antone, S.; Solaro, R. Biodegradation of poly (vinyl alcohol) based materials. *Prog. Polym. Sci.* **2003**, *28*, 963−1014.
(34) Siddaramaiah; Raj, B.; Somashekar, R. Structure−property relation in polyvinyl alcohol/starch composites. *J. Appl. Polym. Sci.* **2004**, *91*, 630−635.
(35) Schroeder, G. O. Multi-layer barrier film. U.S. Patent US4254169 A, 1981.
(36) Cheng, A.; Rodriguez, F. Mechanical properties of borate crosslinked poly(vinyl alcohol) gels. *J. Appl. Polym. Sci.* **1981**, *26*, 3895−3908.
(37) Kim, H. M.; Lee, J. K.; Lee, H. S. Transparent and high gas barrier films based on poly(vinyl alcohol)/graphene oxide composites. *Thin Solid Films* **2011**, *519*, 7766−7771.
(38) Lagrain, B.; Goderis, B.; Brijs, K.; Delcour, J. A. Molecular basis of processing wheat gluten toward biobased materials. *Biomacromolecules* **2010**, *11*, 533−541.
(39) Vo Hong, N.; Pyka, G.; Wevers, M.; Goderis, B.; Van Puyvelde, P.; Verpoest, I.; Van Vuure, A. W. Processing rigid wheat gluten biocomposites for high mechanical performance. *Composites, Part A* **2015**, *79*, 74−81.
(40) Dicharry, R. M.; Ye, P.; Saha, G.; Waxman, E.; Asandei, A. D.; Parnas, R. S. Wheat Gluten− Thiolated poly (vinyl alcohol) blends with improved mechanical properties. *Biomacromolecules* **2006**, *7*, 2837−2844.
(41) Dong, J.; Dicharry, R.; Waxman, E.; Parnas, R. S.; Asandei, A. D. Imaging and Thermal Studies of Wheat Gluten/Poly(vinyl alcohol) and Wheat Gluten/Thiolated Poly(vinyl alcohol) Blends. *Biomacromolecules* **2008**, *9*, 568−573.
(42) Ridgley, D. M.; Claunch, E. C.; Barone, J. R. Characterization of large amyloid fibers and tapes with Fourier Transform Infrared (FT-IR) and raman spectroscopy. *Appl. Spectrosc.* **2013**, *67*, 1417−1426.
(43) Finch, C. A. *Polyvinyl Alcohol; Properties and Applications*; John Wiley & Sons: London, 1973.
(44) Lu, J.; Wang, T.; Drzal, L. T. Preparation and properties of microfibrillated cellulose polyvinyl alcohol composite materials. *Composites, Part A* **2008**, *39*, 738−746.
(45) Limpan, N.; Prodpran, T.; Benjakul, S.; Prasarpran, S. Properties of biodegradable blend films based on fish myofibrillar protein and polyvinyl alcohol as influenced by blend composition and pH level. *J. Food Eng.* **2010**, *100*, 85−92.
(46) Limpan, N.; Prodpran, T.; Benjakul, S.; Prasarpran, S. Influences of degree of hydrolysis and molecular weight of poly(vinyl alcohol) (PVA) on properties of fish myofibrillar protein/PVA blend films. *Food Hydrocolloids* **2012**, *29*, 226−233.
(47) Chiellini, E.; Cinelli, P.; Ilieva, V. I.; Martera, M. Biodegradable thermoplastic composites based on polyvinyl alcohol and algae. *Biomacromolecules* **2008**, *9*, 1007−1013.
(48) Srinivasa, P. C.; Ramesh, M. N.; Kumar, K. R.; Tharanathan, R. N. Properties and sorption studies of chitosan−polyvinyl alcohol blend films. *Carbohydr. Polym.* **2003**, *53*, 431−438.
(49) Zimmermann, T.; Pöhler, E.; Geiger, T. Cellulose Fibrils for Polymer Reinforcement. *Adv. Eng. Mater.* **2004**, *6*, 754−761.


DOI: 10.1021/acssuschemeng.7b03872
*ACS Sustainable Chem. Eng.* 2018, 6, 2422−2430

(50) Zimmermann, T.; Bordeanu, N.; Strub, E. Properties of nanofibrillated cellulose from different raw materials and its reinforcement potential. *Carbohydr. Polym.* **2010**, *79*, 1086−1093.
(51) Keten, S.; Xu, Z.; Ihle, B.; Buehler, M. J. Nanoconfinement controls stiffness, strength and mechanical toughness of β-sheet crystals in silk. *Nat. Mater.* **2010**, *9*, 359−367.
(52) Zhang, X.; Burgar, I.; Lourbakos, E.; Beh, H. The mechanical property and phase structures of wheat proteins/polyvinyl alcohol blends studied by high-resolution solid-state NMR. *Polymer* **2004**, *45*, 3305−3312.
(53) Tang, X.; Alavi, S. Recent advances in starch, polyvinyl alcohol based polymer blends, nanocomposites and their biodegradability. *Carbohydr. Polym.* **2011**, *85*, 7−16.
(54) Sudhamani, S. R.; Prasad, M. S.; Udaya Sankar, K. DSC and FTIR studies on Gellan and Polyvinyl alcohol (PVA) blend films. *Food Hydrocolloids* **2003**, *17*, 245−250.
(55) Maria, T. M.; De Carvalho, R. A.; Sobral, P. J.; Habitante, A. M. B.; Solorza-Feria, J. The effect of the degree of hydrolysis of the PVA and the plasticizer concentration on the color, opacity, and thermal and mechanical properties of films based on PVA and gelatin blends. *J. Food Eng.* **2008**, *87*, 191−199.
(56) Alexy, P.; Káchová, D.; Kršiak, M.; Bakoš, D.; Šimková, B. Poly(vinyl alcohol) stabilisation in thermoplastic processing. *Polym. Degrad. Stab.* **2002**, *78*, 413−421.
(57) Tian, H.; Yan, J.; Rajulu, A. V.; Xiang, A.; Luo, X. Fabrication and properties of polyvinyl alcohol/starch blend films: Effect of composition and humidity. *Int. J. Biol. Macromol.* **2017**, *96*, 518−523.
(58) Holland, B. J.; Hay, J. N. The thermal degradation of poly(vinyl alcohol). *Polymer* **2001**, *42*, 6775−6783.
(59) Kieffer, R.; Schurer, F.; Köhler, P.; Wieser, H. Effect of hydrostatic pressure and temperature on the chemical and functional properties of wheat gluten: studies on gluten, gliadin and glutenin. *J. Cereal Sci.* **2007**, *45*, 285−292.
(60) Apichartsrangkoon, A.; Ledward, D. A.; Bell, A. E.; Brennan, J. G. Physicochemical properties of high pressure treated wheat gluten. *Food Chem.* **1998**, *63*, 215−220.
(61) Jansens, K. J. A.; Lagrain, B.; Rombouts, I.; Brijs, K.; Smet, M.; Delcour, J. A. Effect of temperature, time and wheat gluten moisture content on wheat gluten network formation during thermomolding. *J. Cereal Sci.* **2011**, *54*, 434−441.
(62) Cano, A.; Fortunati, E.; Cháfer, M.; Kenny, J.; Chiralt, A.; González-Martínez, C. Properties and ageing behaviour of pea starch films as affected by blend with poly (vinyl alcohol). *Food Hydrocolloids* **2015**, *48*, 84−93.
(63) Wang, W.; Nema, S.; Teagarden, D. Protein aggregation—Pathways and influencing factors. *Int. J. Pharm.* **2010**, *390*, 89−99.
(64) Meyer, E. P.; Ulmann-Schuler, A.; Staufenbiel, M.; Krucker, T. Altered morphology and 3D architecture of brain vasculature in a mouse model for Alzheimer's disease. *Proc. Natl. Acad. Sci.* **2008**, *105*, 3587−3592.
(65) Jung, J.-M.; Savin, G.; Pouzot, M.; Schmitt, C.; Mezzenga, R. Structure of Heat-Induced β-Lactoglobulin Aggregates and their Complexes with Sodium-Dodecyl Sulfate. *Biomacromolecules* **2008**, *9*, 2477−2486.
(66) Meersman, F.; Dobson, C. M. Probing the pressure−temperature stability of amyloid fibrils provides new insights into their molecular properties. *Biochim. Biophys. Acta, Proteins Proteomics* **2006**, *1764*, 452−460.
(67) Morris, A. M.; Watzky, M. A.; Finke, R. G. Protein aggregation kinetics, mechanism, and curve-fitting: A review of the literature. *Biochim. Biophys. Acta, Proteins Proteomics* **2009**, *1794*, 375−397.
(68) Cohen, S. I. A.; Vendruscolo, M.; Dobson, C. M.; Knowles, T. P. J. From Macroscopic Measurements to Microscopic Mechanisms of Protein Aggregation. *J. Mol. Biol.* **2012**, *421*, 160−171.
(69) Fändrich, M. Oligomeric Intermediates in Amyloid Formation: Structure Determination and Mechanisms of Toxicity. *J. Mol. Biol.* **2012**, *421*, 427−440.
(70) Lee, J.; Lee, K. J.; Jang, J. Effect of silica nanofillers on isothermal crystallization of poly (vinyl alcohol): In-situ ATR-FTIR study. *Polym. Test.* **2008**, *27*, 360−367.
(71) Otsuka, E.; Sugiyama, M.; Suzuki, A. Formation and destruction of physical crosslinks by mild treatments in chemically crosslinked poly (vinyl alcohol) gels. *Polym. Bull.* **2011**, *67*, 1215−1226.
(72) Krimm, S.; Liang, C. Y.; Sutherland, G. B. B. M. Infrared spectra of high polymers. V. Polyvinyl alcohol. *J. Polym. Sci.* **1956**, *22*, 227−247.
(73) Hinterstoisser, B.; Åkerholm, M.; Salmén, L. Effect of fiber orientation in dynamic FTIR study on native cellulose. *Carbohydr. Res.* **2001**, *334*, 27−37.
(74) Alexy, P.; Lacík, I.; Šimková, B.; Bakoš, D.; Prónayová, N. a.; Liptaj, T.; Hanzelová, S.; Várošová, M. Effect of melt processing on thermo-mechanical degradation of poly(vinyl alcohol)s. *Polym. Degrad. Stab.* **2004**, *85*, 823−830.
(75) Coates, J. *Interpretation of Infrared Spectra, a Practical Approach*; John Wiley & Sons Ltd: Chichester, U.K., 2000.
(76) Miya, M.; Iwamoto, R.; Mima, S. FT-IR study of intermolecular interactions in polymer blends. *J. Polym. Sci., Polym. Phys. Ed.* **1984**, *22*, 1149−1151.
(77) Max, J.-J.; Chapados, C. Infrared Spectroscopy of Aqueous Carboxylic Acids: Comparison between Different Acids and Their Salts. *J. Phys. Chem. A* **2004**, *108*, 3324−3337.
(78) Yu, Y.-H.; Lin, C.-Y.; Yeh, J.-M.; Lin, W.-H. Preparation and properties of poly(vinyl alcohol)−clay nanocomposite materials. *Polymer* **2003**, *44*, 3553−3560.
(79) Tubbs, R. K. Sequence distribution of partially hydrolyzed poly (vinyl acetate). *J. Polym. Sci., Part A-1: Polym. Chem.* **1966**, *4*, 623−629.
(80) Barth, A. Infrared spectroscopy of proteins. *Biochim. Biophys. Acta, Bioenerg.* **2007**, *1767*, 1073−1101.


DOI: 10.1021/acssuschemeng.7b03872
*ACS Sustainable Chem. Eng.* 2018, 6, 2422−2430

# CHAPTER III. PROTEIN-POLYISOPRENE RUBBER COMPOSITES

DeButts, B. L., Hanzly, L. E., & Barone, J. R. (2018). Protein-polyisoprene rubber composites. *Journal of Applied Polymer Science, 135*(12), 46026.

Journal of Applied Polymer Science

# Protein-polyisoprene rubber composites

**Barbara L. DeButts**,[1,2] **Laura E. Hanzly**,[2] **Justin R. Barone**[1,2,3]

[1]Macromolecular Science and Engineering and Macromolecules Innovation Institute, Virginia Tech, Blacksburg, Virginia 24061
[2]Biological Systems Engineering, Virginia Tech, 301 Human and Agricultural Biosciences Building 1, 1230 Washington St. SW, Blacksburg, Virginia 24061
[3]Center for Soft Matter and Biological Physics, Virginia Tech, Blacksburg, Virginia 24061
Correspondence to: J. R. Barone (E-mail: jbarone@vt.edu)

**ABSTRACT:** Hydrolyzed proteins previously shown to aggregate in aqueous solution were compounded into synthetic polyisoprene rubber (IR). Modulus increases of up to 232% resulted from protein reinforcement of IR. Increased hydrogen bonding on amine groups and the presence of β-sheets in the protein phase were observed via Fourier transform infrared (FTIR) spectroscopy. The total β-sheet amount relative to the IR content strongly correlated to the modulus and varied with the protein concentration, protein aggregation state, and compounding conditions. Isotropic protein aggregates on the order of hundreds of nanometers were observed by scanning electron microscopy with energy dispersive x-ray spectroscopy (SEM-EDX). The aggregates were evenly dispersed throughout the rubber matrix after compounding. The composite glass transition temperature ($T_g$) was unchanged from the control, which indicated that the protein and rubber existed as two discrete phases. Remarkably, protein β-sheet structures were observed in FTIR even after rubber compounding under harsh conditions. © 2017 Wiley Periodicals, Inc. J. Appl. Polym. Sci. **2018**, *135*, 46026.

**KEYWORDS:** composites; mechanical properties; microscopy; proteins; rubber

Received 8 August 2017; accepted 7 November 2017
**DOI: 10.1002/app.46026**

## INTRODUCTION

Nanofillers offer unique increases in mechanical and barrier properties at very low concentration.[1] The problem with nanocomposites is that the high surface area creates surface forces between the particles, causing agglomeration. Even weak van der Waals forces become impactful because they are summed many times. This makes nanofillers very difficult to disperse into polymers using typical polymer processing equipment.[2,3] A variety of methods have been used to promote nanofiller dispersion but are generally not adaptable to large scale production.[4–7] Thus, despite the huge advantages of nanocomposites reported for the past 20 years, a large volume practical application has not been realized.

Rubber nanocomposites are of interest, especially in the tire industry, because nanofillers can increase tear strength while decreasing viscoelastic losses and gas permeability.[8,9] Early rubber nanocomposite research focused on nanoclay, i.e., layered silicates, to reinforce natural or synthetic rubbers such as polyisoprene and styrene-butadiene.[10–14] More recently, other nanofillers have been studied, including nanocellulose, carbon nanotubes, and graphene oxide.[15–26] Natural rubber (NR), which is a product of the coagulation of the latex obtained from the *Hevea brasiliensis* tree, contains a few percent natural proteins and lipid. NR is used in demanding applications like airplane and truck tires because it has superior properties to synthetically-derived polyisoprene. It has long been believed the combination of protein, lipid, and high molecular weight polyisoprene is the origin of NR's superior properties, but no definitive mechanism has been found.[27–29] Recently, NR's rubber elongation factor (REF) protein has been shown to self-assemble into a high β-sheet content material called an "amyloid."[30] Amyloids are an emerging nanomaterial with properties similar to silk but form via self-assembly rather than extrusion.[31] It can be hypothesized that a highly reinforcing amyloid phase formed during rubber compounding would confer a significant property advantage to NR over other rubbers that do not contain the protein.[32]

Protein molecules can be aggregated or self-assembled into nanostructures in aqueous solution.[33,34] A very common and easy aggregation motif is when a protein molecule or "chain" unravels, straightens, and hydrogen bonds to a nearby straightened protein molecule to form a β-sheet. β-sheets are the crystalline regions of silk and other high performance natural proteins that provide them with extraordinary properties.[35] In a self-assembled β-sheet, hydrogen bonding happens between the main chain carbonyl (—C═O) on one protein and the main

chain secondary amine (—NH) on another chain. The characteristic distance between two protein chains in a self-assembled β-sheet is ~0.47 nm.[36–39] Hydrolyzing full proteins to short chain peptides is one way to straighten chains and foster β-sheet formation.[40,41] Denaturing conditions, such as applied stress or changes in solution pH, ionic strength, and temperature, also encourage β-sheet self-assembly.[42–45] Exposing protein molecules to various denaturing surfaces allows β-sheet formation.[46,47] In aqueous solution, protein β-sheet formation is thermodynamically driven by hydrophobic groups on amino acid side chains packing together to hide from water.[48–51]

Given that the protein in NR is known to contribute to its superior properties and that it can form an amyloid, it was hypothesized that introducing known aggregating proteins into IR could create a composite that matched the properties of NR. This would be important to the use of synthetic rubber since NR is used in more demanding applications. Protein powders ground to particle sizes of tens to hundreds of microns have been used before to reinforce rubber, but they were not aggregated or necessarily highly structured proteins.[52–54] Here, the hypothesis was that hydrolyzed proteins could aggregate into rigid β-sheet nanostructures to reinforce the rubber. Specifically, that largely unstructured coiled proteins like wheat gluten and its component protein, gliadin, could be coaxed into aggregation. In this paper, hydrolyzed proteins were compounded into synthetic polyisoprene rubber and the effects of protein structure and compounding conditions on composite properties were investigated. The β-sheet containing protein acted as a reinforcing nanofiller to realize *in situ* formed amyloid-rubber composites.

## EXPERIMENTAL

### Materials

Wheat gluten (WG) was purchased from MP Biomedicals, LLC, (Solon, OH). Gliadin from wheat (Gd), trypsin enzyme (Type I from bovine pancreas), β-mercaptoethanol (BME), and slab synthetic polyisoprene rubber (IR, 97% cis-1,4-polyisoprene) were purchased from Sigma-Aldrich (St. Louis, MO). CV60 grade natural rubber was graciously provided by Ford Motor Company (Dearborn, MI).

### Methods

**Protein Preparation.** ***Method 1: Trypsin hydrolyzed wheat gluten (THWG) and trypsin hydrolyzed gliadin (THGd).*** WG (20 g) or Gd (20 g) was slowly added to distilled water (800 mL) rapidly stirring at 37 °C. Trypsin (0.3 g) was added, then the dispersion was gently stirred at 60 rpm and 37 °C for 72 h to completely hydrolyze the protein without aggregating the peptides.[41,45] Over the 72 h, NaOH (1 M or 4 M) was added to achieve pH 8. At 72 h, the THWG or THGd hydrolysate was poured into polytetrafluoroethylene (PTFE)-coated aluminum foil and dried to ~85% solids content under a fume hood at room temperature (RT).

***Method 2: Solution aggregated THGd (THGd-SA).*** Gd was hydrolyzed for 72 h with trypsin as described in method 1. To encourage protein self-assembly into β-sheets, the hydrolysate dispersion was incubated at 37 °C for an additional 72 h. During the incubation period, the dispersion was not stirred and the pH was allowed to fluctuate. At 144 h, the solution-incubated hydrolysate was poured into PTFE-coated aluminum foil and dried to ~85% solids content under a fume hood at room temperature (RT).

***Method 3: THGd reduced with β-mercaptoethanol (THGd-BME).*** After 24 h of hydrolysis by method 1, BME (41.2 mg, 2 eqiv. per mole S-S) was added to the THGd dispersion to reduce the sulfur–sulfur bonds.[48] The reaction continued for an additional 48 h to reach the 72 h total hydrolysis time. The moles of S—S bonds in the protein were calculated using the Gd sequence from UniProt (P04721). At 72 h, the hydrolysate was poured into PTFE-coated aluminum foil and dried to ~85% solids content under a fume hood at room temperature (RT).

**Compounding.** All hydrolyzed protein was compounded into IR in 30 g batches on a Prep-Center with an internal mixing head (Brabender, Hackensack, NJ) using typical rubber compounding conditions of 150 °C and 30–60 rpm. The concentration of THWG or THGd hydrolysate was systematically varied from 5% to 30% w/w. The hydrolysate was approximately 85% solids with the remainder being residual water. This was determined by running thermogravimetric analysis (TGA) on the hydrolysate after drying under the hood and then after removing all water by vacuum drying for 7 days. IR was mixed for 30 s prior to adding the protein hydrolysate. Composite compounding times ranged from 1–15 min after addition of the protein. The water in the hydrolysate evaporated upon introduction to the internal mixing head. A 30 g batch of as-received NR was compounded at 60 rpm for 15 min.

**Rheology.** Unvulcanized rubber composites were pressed for approximately 30 s with 1000 lb force using a Carver bench top manual press. Flattened samples were equilibrated for 2 min under ambient conditions, followed by a stress sweep from 100–1000 Pa at 1 Hz, equilibrated for an additional 2 min, then a frequency sweep from 0.1 to 100 Hz at 150 Pa was conducted with 25 mm parallel plates (AR2000, TA Instruments, New Castle, DE). A fixed gap of $3.2 \pm 0.2$ mm was maintained. The storage modulus ($G'$) and the loss modulus ($G''$) were measured in the dynamic rheology experiment. The $G'$ and loss tangent ($\tan \delta = G''/G'$) were reported. Replicate runs of NR and IR controls and 17% THWG and THGd composites were conducted and no change in flow behavior was observed.

**Fourier Transform Infrared (FTIR) Spectroscopy.** Spectra were acquired from 4000–525 $cm^{-1}$ with 128-scans at a resolution of 4 $cm^{-1}$ on a Nicolet 6700 equipped with a Smart Orbit attenuated total reflectance (ATR) diamond crystal (Thermo Fisher Scientific Inc., Madison, WI). Spectra were collected in triplicate for each compound and a standard error was calculated from the absorbance average at a specific wavenumber. Spectra were analyzed using OMNIC v. 8.1.0.10 software.

**Scanning Electron Microscopy with Energy Dispersive X-ray Spectroscopy (SEM-EDX).** Samples were freeze fractured in liquid nitrogen then sputter-coated with 5 nm iridium at a 45° angle. Scanning electron micrographs were imaged using a FEI

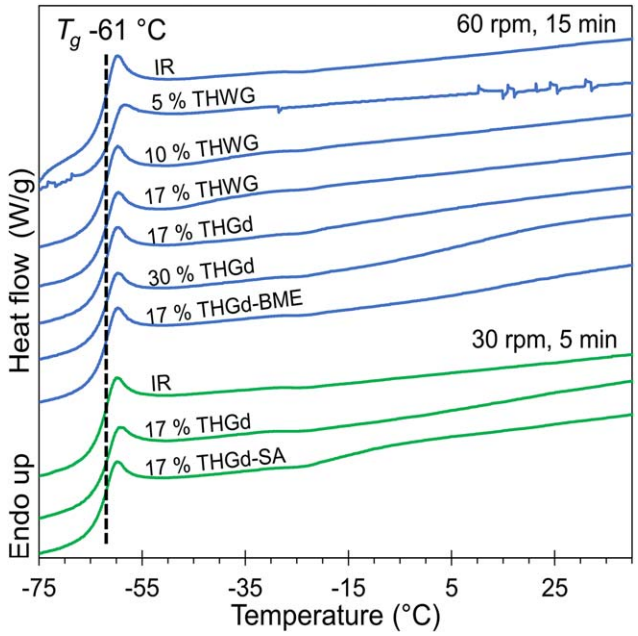


**Figure 1.** DSC thermograms for controls and composites compounded at 150 °C. The thermograms were stacked in the order given in Table I, where the top samples (black lines) were compounded at 60 rpm for 15 min and the bottom samples (green lines) were compounded at 30 rpm for 5 min. [Color figure can be viewed at wileyonlinelibrary.com]

Quanta 600 FEG environmental SEM equipped with a Bruker EDX Silicon Drifted Detector (Thermo Fischer Scientific, Waltham, MA). Backscattered electron (BSE) images were obtained with a 12.4 mm working distance and 10 kV accelerating voltage. During imaging, the electron beam induced rubber relaxation which cracked and puckered the iridium coating. While some surface features were obscured by the cracking phenomenon, the elemental distribution was unaffected. Therefore, elemental maps were used to identify protein aggregation within the sample. Oxygen was exclusive to the protein phase and any Z-contrast arising from oxygen identified the protein phase. A corresponding decrease in the carbon signal intensity confirmed a protein phase domain. Protein aggregates smaller than 1 $\mu m^2$ could not be resolved by the EDX detector. Measurements of the size of protein aggregates were made using ImageJ software.

**Thermal Characterization.** Differential scanning calorimetry (DSC, Q1000, TA Instruments, Waltham, MA) was performed on unvulcanized compounds. Samples (16–17 mg, TZero aluminum pans) were subjected to a cool-heat-cool-heat cycle from −90 to 90 °C at 10 °C/min. The first heating cycle was reported. Thermogravimetric analysis (TGA) of the samples (16–17 mg, alumina sample cups) was performed on a SDT-Q600 Simultaneous TGA/DSC (TA Instruments, New Castle, D-E) at 10 °C/min from 25 to 600 °C in a nitrogen atmosphere.

## RESULTS AND DISCUSSION

### Composite Thermal Properties

The glass transition temperature ($T_g$) of the IR phase remained constant at −61 °C in both the controls and composites, and was also unaffected by the compounding time and speed and the protein concentration (Figure 1). At higher protein loadings, there was evidence of a second step transition induced by the protein phase, most likely a protein $T_g$. This was most apparent for the 30% THGd composite, but smaller transitions appeared in the 17% THGd composites, particularly in the 17% THGd-SA compounds. This transition was broader than the IR $T_g$ and the transition midpoint occurred between −7 and 20 °C and varied between composites. Protein $T_g$s are complex and are affected by degree of aggregation, as well as molecular weight, protein-polymer interactions, and the presence of plasticizers.[55] The magnitude and temperature at which the thermal transitions occurred remained the same for both heating cycles of a given sample, and only the first heat was represented graphically in Figure 1. The TGA data in Figure 2 showed two discrete degradation events: one for the protein centered at 270 °C (Figure 2, inset) and one for the IR centered at 380 °C. The IR degradation did not shift to lower temperature with the addition of rubber. Both the DSC and TGA data suggested that the protein and rubber existed as two separate phases.

### Protein Concentration: Effect on Properties

The storage modulus, $G'$, of the composite compounds was increased at hydrolyzed protein concentrations of 10 wt % or greater [Figure 3(a)]. As THWG or THGd concentration increased, modulus increased. At 30 wt % THGd, $G'$ exceeded that of NR compounded at the same conditions. It was hypothesized that the rigid β-sheet nanostructures were responsible for the reinforcement of the IR matrix. The relative protein β-sheet content in each compound was quantified by FTIR spectroscopy. To describe the protein β-sheet content in the composite with respect to a fixed concentration of IR, the absorbance peak at 1620 $cm^{-1}$ was compared to the absorbance peak at 1375 $cm^{-1}$ (Figure 4). β-sheets appeared in the 1605–

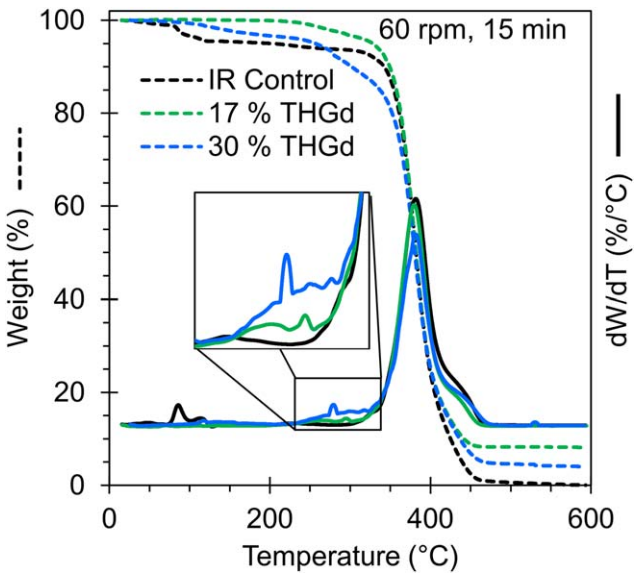


**Figure 2.** TGA weight loss (dashed lines) and the first derivative of the weight loss with respect to temperature, $dW/dT$ (solid lines), for controls and composites compounded at 150 °C. Inset: Major protein degradation event from 235–320 °C. [Color figure can be viewed at wileyonlinelibrary.com]

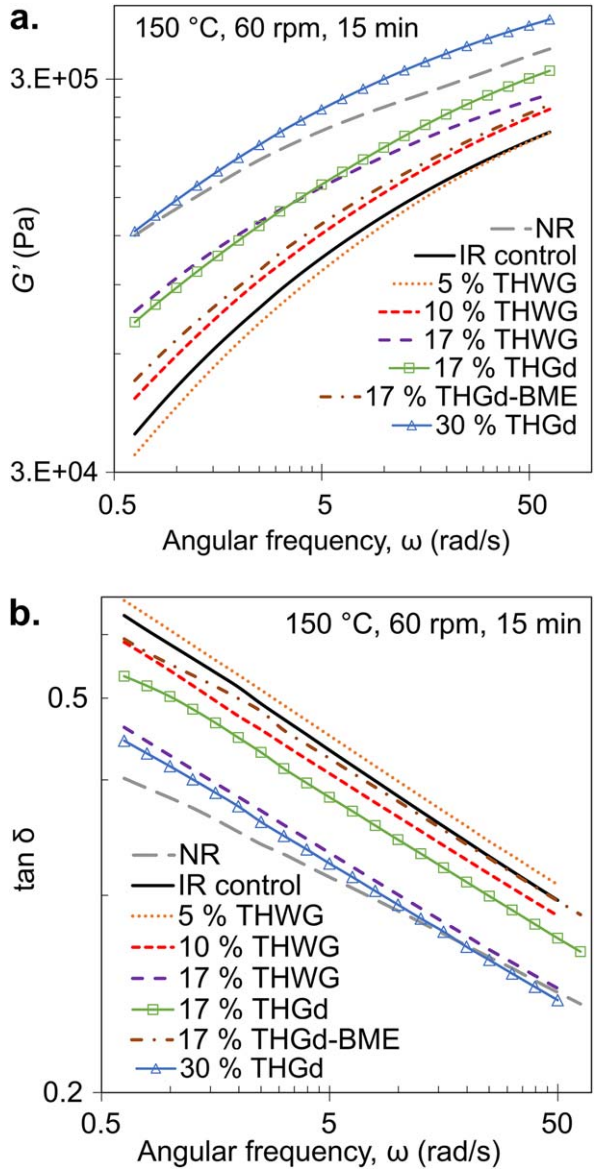


**Figure 3.** (a) Log-log plot of storage modulus, $G'$, versus angular frequency for control and composites compounded at 150 °C, 60 rpm, and 15 min. (b) Loss tangent, tan δ, versus angular frequency. [Color figure can be viewed at wileyonlinelibrary.com]

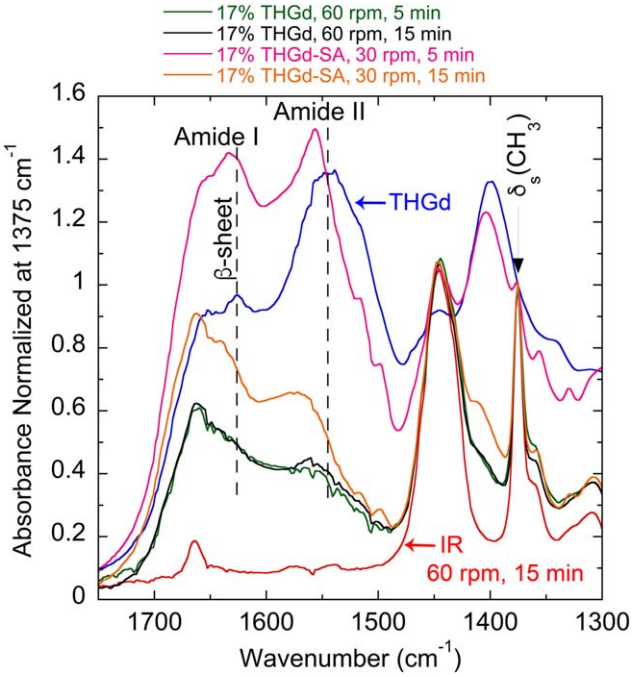


**Figure 4.** FTIR spectra of IR control, fully aggregated THGd, and composites compounded at 150 °C at various conditions. The 1665 $cm^{-1}$ (C═C) and 1375 $cm^{-1}$ $\delta_s(CH_3)$ absorbance peaks originated in IR while β-sheets at the 1620 $cm^{-1}$ ν(C═O) absorbance peak originated in aggregated protein. The spectra were normalized to constant IR content at the 1375 $cm^{-1}$ $\delta_s(CH_3)$ absorbance peak. [Color figure can be viewed at wileyonlinelibrary.com]

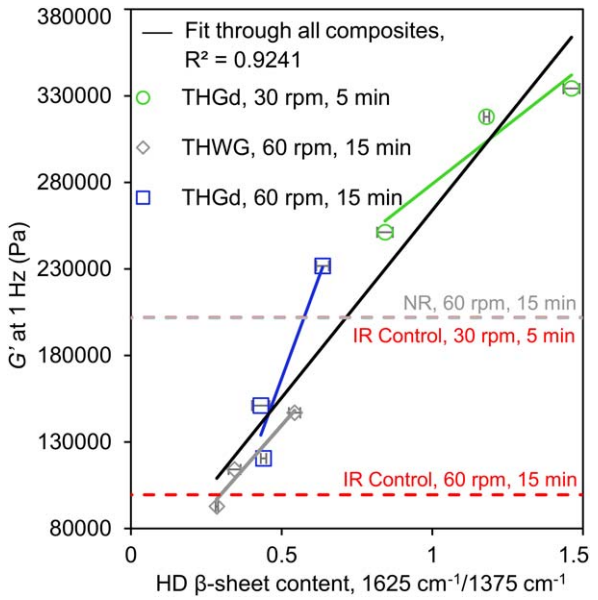


**Figure 5.** Correlation between storage modulus, $G'$, at 1 Hz (=6.28 rad/s) and high density β-sheet content relative to IR. All compounds were prepared at 150 °C Compounding conditions and numerical data used to produce the graph are contained in Table I. [Color figure can be viewed at wileyonlinelibrary.com]

1635 $cm^{-1}$ region of the Amide I absorbance peak, with the 1620 $cm^{-1}$ absorbance peak indicative of high density (HD) β-sheets in amyloids.[56] The 1620 $cm^{-1}$ absorbance peak was resolved from the rubber absorbance peak at ~1660 $cm^{-1}$ (C═C), so it did not convolute the interpretation. A strong signal at 1375 $cm^{-1}$ was attributed to $\delta_s(CH_3)$ found in synthetic polyisoprene rubber.[57] Therefore, the ratio of 1620 $cm^{-1}$/1375 $cm^{-1}$ described the amount of aggregated β-sheets in the protein phase relative to IR in the composite. While it was not possible to measure the total amount of protein converted to β-sheet relative to the original amount, it was possible to show the amount of β-sheets in the protein portion of the composites relative to the IR portion. The total β-sheet content increased with protein concentration, suggesting that β-sheets contributed

**Table I.** Storage Modulus ($G'$) and β-Sheet Content

| Compound, compounding speed, compounding time | $G'$ @ 1 Hz (Pa) | β-Sheet to rubber ratio from FTIR (1620 $cm^{-1}$/1375 $cm^{-1}$ ± standard error) |
|---|---|---|
| IR control, 60 rpm, 15 min | 99,475.2 | 0.096 ± 0.011 |
| 5% THWG, 60 rpm, 15 min | 92,813.2 | 0.285 ± 0.004 |
| 10% THWG, 60 rpm, 15 min | 114,115 | 0.344 ± 0.020 |
| 17% THWG, 60 rpm, 15 min | 146,848 | 0.543 ± 0.019 |
| 17% THGd, 60 rpm, 15 min | 150,984 | 0.431 ± 0.029 |
| 30% THGd, 60 rpm, 15 min | 231,746 | 0.636 ± 0.021 |
| 17% THGd+BME, 60 rpm, 15 min | 120,440 | 0.440 ± 0.009 |
| IR control, 30 rpm, 5 min | 201,896 | 0.097 ± 0.011 |
| 17% THGd, 30 rpm, 5 min | 251,138 | 0.843 ± 0.026 |
| 17% THGd - SA, 30 rpm, 5 min | 334,190 | 1.462 ± 0.027 |

The values are given by the FTIR absorbance peak intensity ratio of 1625 $cm^{-1}$/1375 $cm^{-1}$, for protein-rubber composites prepared under different parameters.
All samples were compounded at 150 °C.
Table I was used to construct Figure 5.

to IR reinforcement. In fact, there was a strong correlation between G' and the amount of β-sheet protein secondary structure in the composite and this was independent of protein composition, protein preparation, and the composite processing method (Figure 5 and Table I). Cellulose whiskers and nanocrystals are other natural biopolymer nanostructures that have been used to reinforce natural rubber. Those composites also showed no change in $T_g$ upon introduction of the filler to the NR. Modulus increased 100%–900% at 7.5–10 wt % whisker content.[17] Swelling of unvulcanized and lightly vulcanized NR decreased by over 100% when chitin whiskers were added at 20 wt %, which would be indicative of a modulus increase. Cellulose nanocrystals increased the storage modulus of unvulcanized NR by up to 195 MPa depending on the nanocrystal preparation conditions and loading.[26] The modulus increases observed here were more modest probably because of the presence of unassembled protein.[41,45]

To confirm that protein aggregates were present in the composite, EDX was first used to resolve the protein phase from the rubber phase. In areas with high oxygen content, i.e., protein, the SEM images showed a surface morphology dominated by smooth, bright globular structures. This morphology was consistent with high oxygen content across all composites imaged. The globules were generally surrounded by striations, or puckering, in the surface, consistent with a relaxing rubber phase (Figure 6). The striations were most apparent in the composites compounded at 60 rpm, where shear forces would theoretically induce greater chain scission and a more severe relaxation phenomenon. A distribution of globule sizes was apparent in many of the composites, with the smallest visible globules on the order of 100–300 nm in diameter.

**Protein Composition: Effect on Properties**

To investigate the protein structures responsible for this reinforcing effect, two different fillers were used: THWG and THGd. At 17% loading, THGd increased the composite $G'$ more than THWG in the high frequency region [Figure 3(a)]. The increased modulus in the high frequency region occurred in the THGd composite, which had slightly lower β-sheet content (Table I). Therefore, there may be other factors that contribute to the modulus, particularly at high frequency where the complex modulus [$G^* = (G'^2 + G''^2)^{1/2}$] behavior approaches the rubbery plateau.[58] Wheat gluten was composed of three full proteins: gliadin (Gd, UniProt P04721, 0.49 mole fraction, 30,403 g/mol), high molecular weight glutenin (GtH, UniProt P08488, 0.06 mole fraction, 70,867 g/mol), and low molecular weight glutenin (GtL, UniProt P10386, 0.45 mole fraction, 34,928 g/mol). We have previously shown that GtL and GtH get hydrolyzed to different lengths compared to Gd with some hydrolysis resistant fractions remaining in the hydrolysate.[59–61]

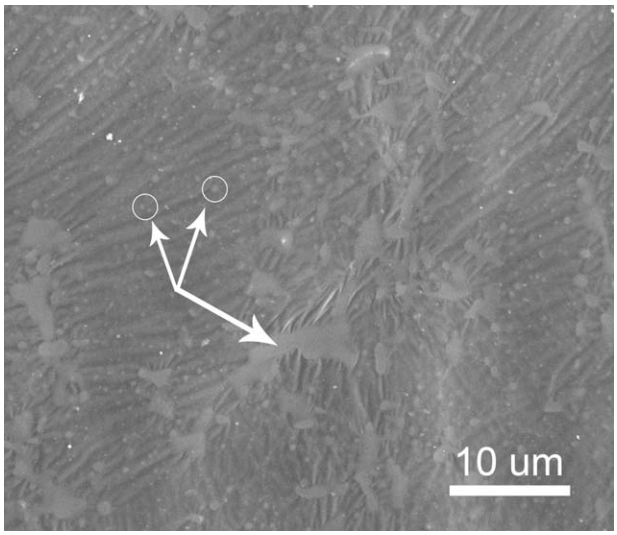


**Figure 6.** SEM micrograph of 30% THGd composite compounded at 60 rpm, 150 °C, 5 min. The arrows identify the protein phase, with some of the smallest visible aggregates circled.

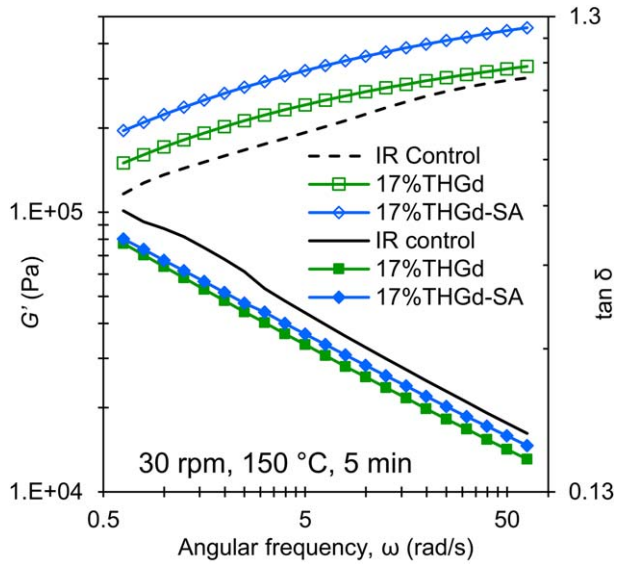


**Figure 7.** $G'$ (open symbols), and tan δ (solid symbols), for control and composites compounded at 150 °C, 30 rpm, and 5 min. [Color figure can be viewed at wileyonlinelibrary.com]

In other words, THWG contained more high molecular weight fraction proteins. Although the THWG composite had more protein molecules assembled into β-sheets, there were enough unassembled high molecular weight proteins contributing to the modulus response as the transition to the rubbery plateau was much earlier for the THWG composite than for the THGd composite. The frequency transition to the rubbery plateau, ω*, can be considered a measure of the overall relaxation time, $\tau \sim 1/\omega^*$, of the polymer molecules and scales with the weight average molecular weight, $M_w$, as $\tau \sim M_w^{3.4}$.[62] Therefore, the 17% THWG compound had a longer overall relaxation time than the 17% THGd compound most likely from the higher molecular weight fraction components from wheat gluten.

The loss tangent, tan δ, defined as the loss modulus over the storage modulus, characterized the elastic storage capacity of the composite. From Figure 3(b), the general trend was that as protein concentration increased, the composite tan δ decreased. This was indicative of more elastic storage and less viscous dissipation of the applied strain energy. However, at the same loading, the 17% THWG compound had a lower loss tangent than the 17% THGd compound and it approached the loss tangent of the 30% THGd compound. Wheat gluten is known to be a highly elastic protein with the elasticity originating in the highest molecular weight fractions.[63,64] The longer overall relaxation time and lower loss tangent data implied that residual high molecular weight protein contributed to these properties. The 17% THWG and 30% THGd compounds approached the loss tangent values for NR especially at high frequency. NR is valued for its high elasticity and low viscous dissipation and the presence of protein is known to contribute to these properties.[27]

### Effect of S—S Bonds in THGd

Sulfur–sulfur bonds between cysteine amino acids in THGd were reduced by BME according to Method 3 and compounds were mixed at 150 °C, 60 rpm, and 15 min. The composite with reduced S—S bonds (THGd-BME) exhibited a lower complex modulus than the THGd composite, suggesting that S—S bonds were important to protein reinforcement of rubber. S—S bonds did not affect THGd β-sheet formation since THGd-BME and THGd had comparable β-sheet content at the same compounding conditions (Table I). In this case, S—S bonds may be between unassembled protein chains or between regions containing β-sheet structures. Disulphide bonds have been shown to stabilize large protein aggregates through intermolecular crosslinking.[65,66] Unlike the unassembled higher molecular weight protein molecules that seemed to plasticize THWG, the S—S bonds must have formed larger networks of protein molecules and β-sheets that acted to reinforce the composite structure such that removing them decreased the reinforcement.

### Solution-Aggregation of THGd: Effect on Composite Properties

Protein aggregation into β-sheet nanostructures is a facile and straightforward process.[67] The successful compounding of hydrolyzed THWG and THGd into IR with resulting reinforcement showed that this simple biological process could be adapted to a polymer processing application. In another preparation method, THGd was pre-aggregated in solution into β-sheet nanostructures (denoted as THGd-SA) prior to compounding. THGd-SA, prepared according to Method 2, achieved the highest composite modulus, as well as the largest β-sheet content (Figure 7 and Table I). However, the increased β-sheet content did not translate to a lower viscous dissipation. Clearly, there were other factors that should be controlled for less

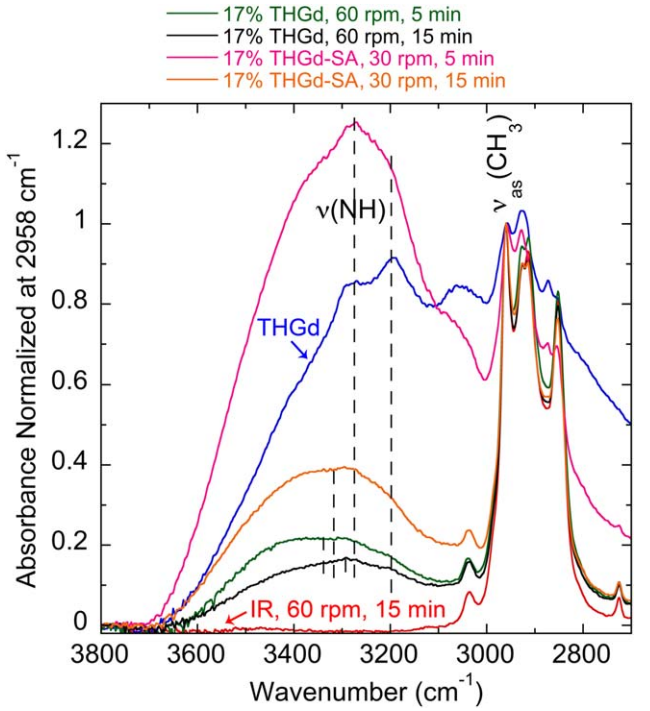


**Figure 8.** FTIR for control and composites investigating the development of protein hydrogen bonding on amines using the amine stretching absorbance peak, ν(NH). [Color figure can be viewed at wileyonlinelibrary.com]

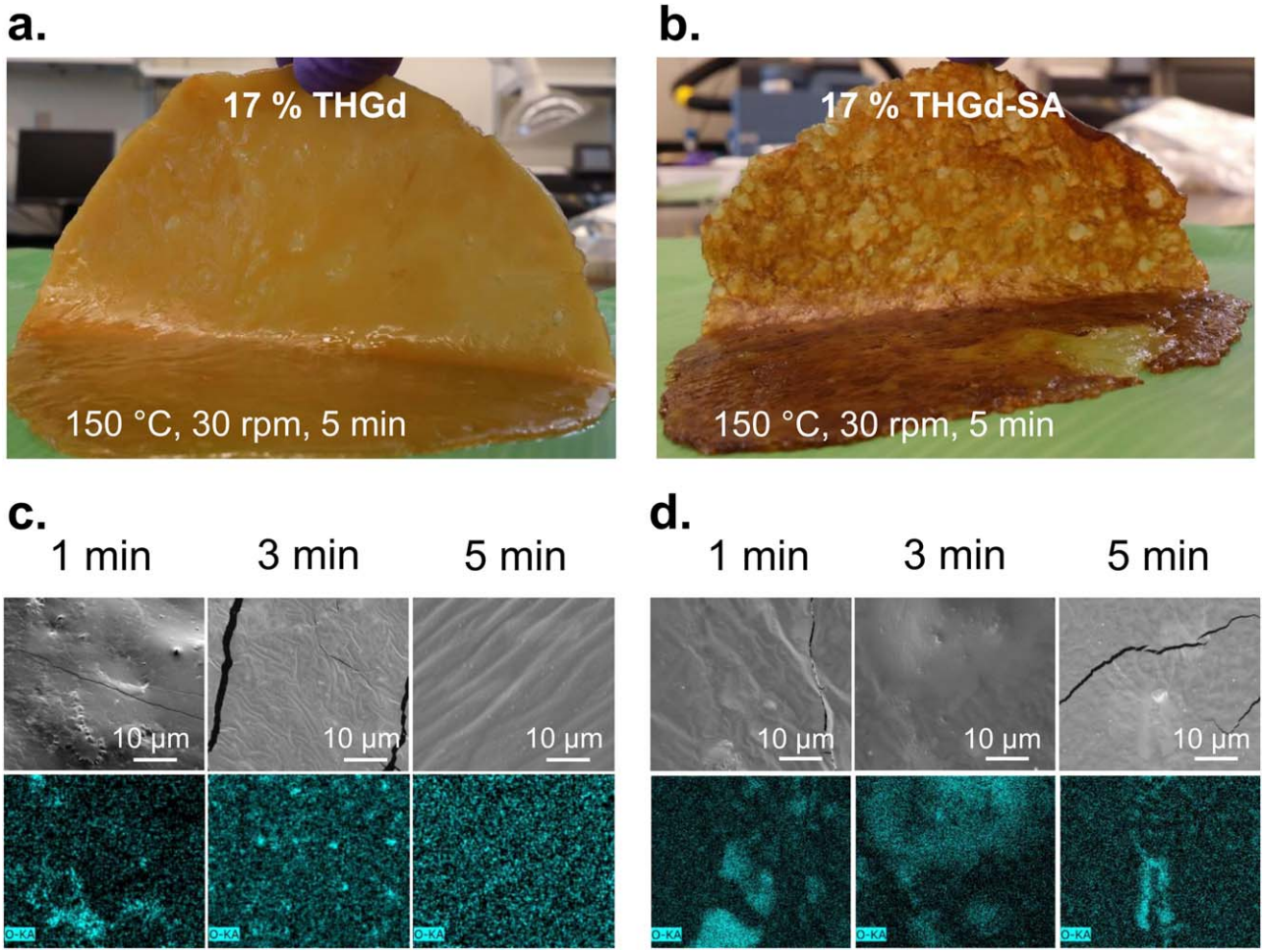


**Figure 9.** Macroscopic view of (a) 17% THGd and (b) 17% THGd-SA compounds prepared at 150 °C, 30 rpm, and 5 min. Time-dependent morphological development of (c) 17% THGd and (d) 17% THGd-SA during compounding at 150 °C, 30 rpm, for 1, 3, and 5 min. SEM images (top row) and corresponding EDX oxygen maps (bottom row). [Color figure can be viewed at wileyonlinelibrary.com]

viscous dissipation, such as the incorporation of unassembled high molecular weight protein fractions, as noted above.

Solution aggregation of THGd resulted in stronger Amide I (1700–1600 $cm^{-1}$) and Amide II (1600–1500 $cm^{-1}$) absorbance peaks than the composites that were not solution aggregated (Figure 4). The Amide I region described the state of backbone carbonyl stretching ν(C═O) and the Amide II region described the δ(N─H) and ν(C─N) modes of the protein backbone and amino acid side chain amines.[68–71] After 5 min of compounding at 150 °C and 30 rpm, the FTIR spectrum of 17% THGd-SA largely resembled the unprocessed, fully-aggregated THGd with both having very strong β-sheet absorbance peaks. After 15 min of compounding, the Amide I and II absorbance peaks in 17% THGd-SA decreased, but were still greater than 17% THGd at any compounding time. The decrease in the Amide II absorbance peak for 17% THGd-SA with compounding time was coupled with a shift to higher wavenumber, which may have indicated decreased hydrogen bonding on the protein backbone (an increase in vibrational energy).[72] It was difficult to say conclusively since there are contributions from the side chain and the main chain amines in Amide II, which is why it is not as sensitive an indicator of protein secondary structure as Amide I.[73] Concurrently, the β-sheet region in the Amide I absorbance peak around 1620–1635 $cm^{-1}$ lost intensity while intensities greater than 1650 $cm^{-1}$ gained intensity, suggesting loss of β-sheets in favor of other structures with compounding time.

In the amine stretching, ν(NH), region around 3300 $cm^{-1}$, 17% THGd-SA increased in wavenumber with compounding time (Figure 8), suggesting a loss of hydrogen bonding coincident with the breakup of self-assembled protein structures (Figure 4). Whereas the 17% THGd compound did not show much change in Amide I and II with compounding time (Figure 4), ν(NH) shifted to lower wavenumber with compounding time (Figure 8). This suggested that protein secondary structure was not affected by compounding time, but that the amine side chains started hydrogen bonding with increased compounding. Since the most abundant amino acids in THGd were glutamine (Q) and proline (P) amino acids, at 35.1% and 13.7%, respectively, it was possible that these were the sites of the increased hydrogen bonding. Unlike THGd-SA, where β-sheets formed in water through a known, thermodynamically favorable hydrophobic mechanism,[48] assembly mechanisms in THGd may form

structures differently in the hydrophobic IR environment. As compounding proceeded, existing β-sheets in THGd-SA began to break up. In contrast, individual protein chains and existing β-sheets in THGd randomly aggregated through amino acid side group hydrogen bonding in the hydrophobic IR environment.

It was clear that protein aggregation in solution prior to compounding resulted in highly reinforcing nanostructures that persisted during compounding. While solution aggregating the protein into β-sheets prior to compounding had maximized β-sheet formation and modulus, it had also adversely affected processability. THGd-SA was difficult to disperse, which was typical of nanofillers in general. Upon addition into the compounder, THGd-SA coated the rubber surface, causing the mixer blades to rotate past one another without shearing the material. With manual intervention, moderate mixing was obtained after 5 min. However, continued mixing beyond 5 min caused the sample to darken in color, indicating degradation. Compared with THGd at the same compounding time, compounds containing THGd-SA were more heterogeneous in appearance, indicating poor protein structure dispersion (Figure 9). This was macroscopic evidence of the molecular phenomena observed in FTIR spectroscopy. Compounding moderately dispersed, but broke apart, the large pre-aggregated β-sheet structures in 17% THGd-SA while encouraging the unaggregated structures in 17% THGd to interact in a more random way, i.e., through amino acid side chain hydrogen bonding rather than the systematic main chain hydrogen bonding characteristic of β-sheet formation.

The above findings were corroborated by SEM elemental maps. SEM images and complementary EDX oxygen maps for 17% THGd and 17% THGd-SA after 1, 3, and 5 min at 150 °C and 30 rpm showed that the dispersion of the solution-aggregated protein was delayed compared to the non-solution-aggregated protein (Figure 9). After 1 min of compounding, both samples showed the presence of isotropic protein agglomerates greater than 10 μm in size. Beyond the first minute, the protein dispersion in 17% THGd and 17% THGd-SA differed. After 3 min of compounding 17% THGd, large agglomerates became smaller isotropic aggregates a few μm in size and, by 5 min, the protein was evenly dispersed as circular aggregates less than 1 μm in size. Conversely, in 17% THGd-SA, agglomerates larger than 10 μm persisted until 5 min of compounding. This result confirmed that compounding effectively dispersed THGd in IR, but that aggregated protein required more energy to achieve a homogeneous state.

Collectively, the molecular structure from FTIR, molecular morphology from SEM-EDX, and visual observations of the macroscopic compound showed evidence that well-aggregated protein β-sheet structures, or amyloids, could remarkably survive very harsh temperature and shear conditions. The temperatures encountered were well above those where hydrogen bonding would be weakened or possibly eliminated.[74] Amyloids have shown high stability to organic solvents and high temperature and pressure conditions. β-sheets have been shown to be more thermally stable than other protein secondary structures because of the shorter bond length between protein chains.[75–79] The amyloids formed here from wheat gluten proteins were no different and were shown to be amenable to rubber compounding conditions.

## CONCLUSIONS

Self-assembling proteins were dispersed and aggregated in synthetic polyisoprene rubber during compounding to form nanocomposites. Composite moduli and protein β-sheet content increased with increasing protein concentration. Trypsin hydrolyzed gliadin (THGd) protein–rubber composites exhibited a higher modulus in the high frequency region than trypsin hydrolyzed wheat gluten (THWG) protein–rubber composites. Reducing the number of sulfur–sulfur bonds in THGd with β-mercaptoethanol (BME) decreased the storage modulus but did not alter the β-sheet content, suggesting that S-S bonds played a role in holding protein molecules and/or β-sheets together. The modulus and β-sheet content was increased with solution-aggregation of THGd prior to compounding, but the solution aggregated protein caused compounding difficulty. Scanning electron microscopy with energy dispersive x-ray spectroscopy (SEM-EDX) results confirmed that THGd could be optimally dispersed within 5 min of compounding but large protein agglomerates remained in the solution aggregated protein (THGD-SA)-rubber composites at the same conditions. The primary rubber glass transition temperature ($T_g$) and degradation temperature were unchanged by the addition of protein indicating the protein and rubber existed as discrete phases and were weakly interacting at most.

## ACKNOWLEDGMENTS

This work was supported by the National Science Foundation (NSF) Industry-University Cooperative Research Centers Program (IUCRC) Center for Tire Research (CenTiRe); and the United States Department of Agriculture [grant number USDA-2016–67021-25006].

## REFERENCES

1. Vaia, R. A.; Giannelis, E. P. *MRS Bull.* **2001**, *26*, 394.
2. Sinha Ray, S.; Okamoto, M. *Prog. Polym. Sci.* **2003**, *28*, 1539.
3. Pavlidou, S.; Papaspyrides, C. D. *Prog. Polym. Sci.* **2008**, *33*, 1119.
4. Ou, Y.; Yang, F.; Yu, Z.-Z. *J. Polym. Sci. Part B: Polym. Phys.* **1998**, *36*, 789.
5. Zeng, C.; Lee, L. J. *Macromolecules* **2001**, *34*, 4098.
6. Sun, T.; Garcés, J. M. *Adv. Mater.* **2002**, *14*, 128.
7. Podsiadlo, P.; Choi, S.-Y.; Shim, B.; Lee, J.; Cuddihy, M.; Kotov, N. A. *Biomacromolecules* **2005**, *6*, 2914.
8. Sengupta, R.; Chakraborty, S.; Bandyopadhyay, S.; Dasgupta, S.; Mukhopadhyay, R.; Auddy, K.; Deuri, A. S. *Polym. Eng. Sci.* **2007**, *47*, 1956.
9. Bhattacharya, M.; Biswas, S.; Bhowmick, A. K. *Polymer* **2011**, *52*, 1562.

10. Galimberti, M. In Advanced Elastomers—Technology, Properties, and Applications; Boczkowska, A., Ed.; InTech: Rijeka, Croatia, 2012; Chapter 4.
11. Liu, Q.; Zhang, Y.; Xu, H. *Appl. Clay Sci.* **2008**, *42*, 232.
12. Varghese, S.; Karger-Kocsis, J. *J. Appl. Polym. Sci.* **2004**, *91*, 813.
13. Wang, Y.; Zhang, L.; Tang, C.; Yu, D. *J. Appl. Polym. Sci.* **2000**, *78*, 1879.
14. Zhang, L. Q.; Wang, Y.; Wang, Y.; Sui, Y.; Yu, D. *J. Appl. Polym. Sci.* **2000**, *78*, 1873.
15. Bokobza, L. *Polymer* **2007**, *48*, 4907.
16. Bouthegourd, E.; Rajisha, K. R.; Kalarical, N.; Saiter, J. M.; Thomas, S. *Mater. Lett.* **2011**, *65*, 3615.
17. Bras, J.; Hassan, M. L.; Bruzesse, C.; Hassan, E. A.; El-Wakil, N. A.; Dufresne, A. *Ind. Crops Prod.* **2010**, *32*, 627.
18. De Falco, A.; Goyanes, S.; Rubiolo, G. H.; Mondragon, I.; Marzocca, A. *Appl. Surf. Sci.* **2007**, *254*, 262.
19. Deng, F.; Ito, M.; Noguchi, T.; Wang, L.; Ueki, H.; Niihara, K-i.; Kim, Y. A.; Endo, M.; Zheng, Q.-S. *ACS Nano* **2011**, *5*, 3858.
20. Fakhru'l-Razi, A.; Atieh, M. A.; Girun, N.; Chuah, T. G.; El-Sadig, M.; Biak, D. R. A. *Compos. Struct.* **2006**, *75*, 496.
21. Montesdeoca-Esponda, S.; Sosa-Ferrera, Z.; Kabir, A.; Furton, K.; Santana-Rodríguez, J. *Anal. Bioanal. Chem.* **2015**, *1*,
22. Gopalan Nair, K.; Dufresne, A. *Biomacromolecules* **2003**, *4*, 657.
23. Kueseng, K.; Jacob, K. I. *Eur. Polym. J.* **2006**, *42*, 220.
24. Le, H. H.; Parsaker, M.; Sriharish, M. N.; Henning, S.; Menzel, M.; Wiessner, S.; Das, A.; Do, Q. K.; Heinrich, G.; Radusch, H.-J. *eXPRESS Polym. Lett.* **2015**, *9*, 960.
25. Potts, J. R.; Shankar, O.; Du, L.; Ruoff, R. S. *Macromolecules* **2012**, *45*, 6045.
26. Siqueira, G.; Tapin-Lingua, S.; Bras, J.; da Silva Perez, D.; Dufresne, A. *Cellulose* **2011**, *18*, 57.
27. Tanaka, Y.; Tarachiwin, L. *Rubber Chem. Technol.* **2009**, *82*, 283.
28. Sansatsadeekul, J.; Sakdapipanich, J.; Rojruthai, P. *J. Biosci. Bioeng.* **2011**, *111*, 628.
29. Rattanasom, N.; Thammasiripong, U.; Suchiva, K. *J. Appl. Polym. Sci.* **2005**, *97*, 1139.
30. Berthelot, K.; Lecomte, S.; Estevez, Y.; Coulary-Salin, B.; Bentaleb, A.; Cullin, C.; Deffieux, A.; Peruch, F. *PLoS ONE.* **2012**, *7*, e48065.
31. Knowles, T. P. J.; Buehler, M. J. *Nat. Nanotechnol.* **2011**, *6*, 469.
32. Berthelot, K.; Lecomte, S.; Estevez, Y.; Peruch, F. *Biochimie* **2014**, *106*, 1.
33. van Hest, J. C. M.; Tirrell, D. A. *Chem. Commun.* **2001**, *1897*.
34. Ridgley, D. M.; Barone, J. R. *ACS Nano* **2013**, *7*, 1006.
35. Keten, S.; Xu, Z.; Ihle, B.; Buehler, M. J. *Nat. Mater.* **2010**, *9*, 359.
36. Sunde, M.; Serpell, L. C.; Bartlam, M.; Fraser, P. E.; Pepys, M. B.; Blake, C. C. F. *J. Mol. Biol.* **1997**, *273*, 729.
37. Serpell, L. C.; Smith, J. M. *J. Mol. Biol.* **2000**, *299*, 225.
38. Makin, O. S.; Sikorski, P.; Serpell, L. C. *Curr. Opin. Chem. Biol.* **2006**, *10*, 417.
39. Nelson, R.; Sawaya, M. R.; Balbirnie, M.; Madsen, A. Ø.; Riekel, C.; Grothe, R.; Eisenberg, D. *Nature* **2005**, *435*, 773.
40. Adamcik, J.; Jung, J.-M.; Flakowski, J.; De Los Rios, P.; Dietler, G.; Mezzenga, R. *Nat. Nanotechnol.* **2010**, *5*, 423.
41. Ridgley, D. M.; Ebanks, K. C.; Barone, J. R. *Biomacromolecules* **2011**, *12*, 3770.
42. Dunstan, D. E.; Hamilton-Brown, P.; Asimakis, P.; Ducker, W.; Bertolini, J. *Prot. Eng. Des. Sel.* **2009**, *22*, 741.
43. Chiti, F.; Dobson, C. M. *Annu. Rev. Biochem.* **2006**, *75*, 333.
44. Fändrich, M.; Forge, V.; Buder, K.; Kittler, M.; Dobson, C. M.; Diekmann, S. *Proc. Natl. Acad. Sci. USA* **2003**, *100*, 15463.
45. Ridgley, D. M.; Claunch, E. C.; Barone, J. R. *Soft Matter* **2012**, *8*, 10298.
46. Anand, G.; Sharma, S.; Dutta, A. K.; Kumar, S. K.; Belfort, G. *Langmuir* **2010**, *26*, 10803.
47. Sethuraman, A.; Vedantham, G.; Imoto, T.; Przybycien, T.; Belfort, G. *Proteins* **2004**, *56*, 669.
48. Ridgley, D. M.; Claunch, E. C.; Lee, P. W.; Barone, J. R. *Biomacromolecules* **2014**, *15*, 1240.
49. Adamcik, J.; Mezzenga, R. *Soft Matter* **2011**, *7*, 5437.
50. Eisenberg, D.; Weiss, R. M.; Terwilliger, T. C.; Wilcox, W. *Faraday Symp. Chem. Soc* **1982**, *17*, 109.
51. Eisenberg, D.; Wilcox, W.; McLachlan, A. D. *J. Cell. Biochem.* **1986**, *31*, 11.
52. Jong, L. *Polym. Int.* **2005**, *54*, 1572.
53. Jong, L. *Compos. Part A: Appl. Sci. Manuf.* **2005**, *36*, 675.
54. Hergenrother, W. L.; Shultz, L. L.; Lin, C. J. Office, U. P. a. T., Ed.; Bridgestone Corporation, USA: **2015**.
55. Micard, V.; Guilbert, S. *Int. J. Biol. Macromol.* **2000**, *27*, 229.
56. Ridgley, D. M.; Claunch, E. C.; Barone, J. R. *Appl. Spectrosc.* **2013**, *67*, 1417.
57. Binder, J. L. *J. Polym. Sci. Part A: Polym. Chem.* **1963**, *1*, 37.
58. Ferry, J. D. Viscoelastic Properties of Polymers, Wiley: New York, **1980**.
59. Athamneh, A.; Barone, J. R. *Smart Mater. Struct.* **2009**, *18*, 104024.
60. Tuck, C. S.; Latham, A.; Lee, P. W.; Barone, J. R. *J. Polym. Environ.* **2014**, *22*, 430.
61. Ahmad, I. A.; Justin, R. B. *Smart Mater. Struct.* **2009**, *18*, 104024.
62. Rubinstein, M.; Colby, R. H. Polymer Physics; **2003**, Oxford University Press: Oxford, UK.
63. Tatham, A. S.; Hayes, L.; Shewry, P. R.; Urry, D. W. *Biochim. Biophys. Acta.* **2001**, *1548*, 187.
64. Tatham, A. S.; Shewry, P. R. *Philos. Trans. R. Soc. Lond., Ser. B: Biol. Sci.* **2002**, *357*, 229.

65. Tilley, K. A.; Benjamin, R. E.; Bagorogoza, K. E.; Okot-Kotber, B. M.; Prakash, O.; Kwen, H. *J. Agric. Food. Chem.* **2001**, *49*, 2627.

66. Shewry, P.; Tatham, A. *J. Cereal Sci.* **1997**, *25*, 207.

67. MacPhee, C. E.; Dobson, C. M. *J. Am. Chem. Soc.* **2000**, *122*, 12707.

68. Gunzler, H.; Gremlich, H.-U. IR Spectroscopy, Wiley-VCH: Weinheim, Germany; **2002**

69. Barth, A. *Biochim. Biophys. Acta* **2007**, *1767*, 1073.

70. Curley, D. M.; Kumosinski, T. F.; Unruh, J. J.; Farrell, H. M. *J. Dairy Sci.* **1998**, *81*, 3154.

71. Mejri, M.; Rogé, B.; BenSouissi, A.; Michels, F.; Mathlouthi, M. *Food Chem.* **2005**, *92*, 7.

72. Coates, J. Interpretation of Infrared Spectra, a practical approach; John Wiley & Sons Ltd: Chichester, UK; **2000**.

73. Kong, J.; Yu, S. *Acta Biochim. Biophys. Sin.* **2007**, *39*, 549.

74. Vogt, G.; Woell, S.; Argos, P. *J. Mol. Biol.* **1997**, *269*, 631.

75. Safar, J.; Roller, P. P.; Gajdusek, D. C.; Gibbs, C. J. *Prot. Sci.* **1993**, *2*, 2206.

76. Dirix, C.; Meersman, F.; MacPhee, C. E.; Dobson, C. M.; Heremans, K. *J. Mol. Biol.* **2005**, *347*, 903.

77. Meersman, F.; Dobson, C. M. *Biochim. Biophys. Acta* **2006**, *1764*, 452.

78. Adler-Abramovich, L.; Reches, M.; Sedman, V. L.; Allen, S.; Tendler, S. J. B.; Gazit, E. *Langmuir* **2006**, *22*, 1313.

79. Cordier, F.; Grzesiek, S. *J. Mol. Biol.* **2002**, *317*, 739.

# CHAPTER IV. PROCESSING-PROPERTY RELATIONSHIPS IN WHEAT PROTEIN-ISOPRENE RUBBER COMPOSITES

DeButts, B. L. & Barone, J. R. (2019). Processing-property relationships in wheat protein-isoprene rubber composites. *Rubber Chemistry and Technology*, (in review).

Chapter IV has been submitted to and is under review by the following peer-reviewed journal: *Rubber Chemistry and Technology* published by the Rubber Division, American Chemical Society (ACS). The chapter is formatted according to the journal guidelines set forth by the publishers.

# PROCESSING-PROPERTY RELATIONSHIPS IN WHEAT PROTEIN-ISOPRENE RUBBER COMPOSITES

BARBARA L. DEBUTTS[a,b] AND JUSTIN R. BARONE[a-c*]

[a]MACROMOLECULAR SCIENCE AND ENGINEERING AND MACROMOLECULES INNOVATION INSTITUTE, VIRGINIA TECH, BLACKSBURG, VA 24061

[b]BIOLOGICAL SYSTEMS ENGINEERING, VIRGINIA TECH, 301D HUMAN AND AGRICULTURAL BIOSCIENCES BUILDING 1, 1230 WASHINGTON ST. SW, BLACKSBURG, VA 24061

[c]CENTER FOR SOFT MATTER AND BIOLOGICAL PHYSICS, DEPARTMENT OF PHYSICS, VIRGINIA TECH, 850 W. CAMPUS DR., BLACKSBURG, VA 24061

*Corresponding author. Email: jbarone@vt.edu (J. R. Barone).

## ABSTRACT

An optimized set of processing parameters were determined for trypsin hydrolyzed gliadin protein (THGd, from wheat) and synthetic isoprene rubber (IR) composite compounds. The compounding temperature, time, and shear dependency of the THGd:IR compounds were investigated with rheology, Fourier transform infrared spectroscopy (FTIR), and scanning electron microscopy with energy dispersive x-ray spectroscopy (SEM-EDX). Individual protein aggregates measuring ~64x280 nm, with a length-to-width aspect ratio of ~4.3, were agglomerated within the IR matrix, as measured in SEM-EDX micrographs. A higher compounding temperature (T=150 °C) was favorable for good protein aggregate dispersion and deagglomeration, which resulted in IR reinforcement, as demonstrated by up to a 65% increase in storage modulus (G'). The tan δ was lowered by the addition of the THGd protein to IR, indicating less mechanical energy was lost as

heat in the composites. As the compounding speed, i.e., shear rate, was increased from 30 to 60 rpm at constant temperature (T=150°C), the average agglomerate size and G' were minimally affected, but the loss tangent (tan δ) was increased, indicating an increase in IR degradation with shear rate. By drying the THGd hydrolysate at a slower rate or to a greater solids content, the composite G' was increased and tan δ was decreased. In the slow-dried THGd hydrolysate, protein aggregates were less resistant to breakup during processing, indicating that the protein preparation was an important processing parameter.

## INTRODUCTION

Biological fillers for polymer composites offer many benefits, including cost reduction, environmental sustainability and recyclability, lower density, and the possibility of diverting material from the agricultural waste stream.[1] Not all biological fillers are equally sustainable and some, such as cotton, have high land and pesticide usage, which decrease sustainability.[2] Furthermore, some biological fillers have been shown to have inferior properties, require low-processing temperatures, exhibit poor filler-polymer adhesion, or have a shortened composite life cycle compared to synthetic fillers.[2, 3] For a biological filler to be industrially viable it must maintain or exceed the properties of the synthetic filler, be relatively low cost, and be processable with industry standard methods. Thus, it is important to understand the biofiller-polymer composite properties as a function of processing conditions.

Biological fillers typically begin to degrade between 150 and 220 °C, which restricts the type of processing conditions as well as the type of polymer matrices that can be used to those with low thermal transitions.[3, 4] Synthetic polyisoprene rubber (IR) is a polymer matrix that is a melt, i.e., viscous polymer liquid, at room temperature and is typically processed at temperatures ≤ 150 °C.[5] Thus, IR represents an ideal matrix for use with biological fillers. Approximately 60-

70% of worldwide rubber consumption is relegated to tire applications.[6, 7] Commonly investigated biofillers for rubber tires include cellulose nanofibers, bio-silica, and lignin, amongst others.[8-11] The use of compatibilizers with hydrophilic natural fibers/fillers is common. In addition to natural rubber, bio-based elastomers have been synthesized and offer the possibility of a completely "green" tire where both the filler and polymer matrix have biological origins.[12] Since end-of-life applications for scrap tires can include granulation and use as infill for synthetic turf, the desorption of volatile filler compounds from the rubber matrix is also of concern.[13]

The automotive industry is interested in new materials that will reduce weight, thereby improving fuel efficiency and reducing $CO_2$ emissions.[14, 15] Additionally, legislation from the European Union and some Asian countries specify end-of-use guidelines that require a high percentage (95% target) of automotive parts to be reusable or recyclable.[16, 17] Natural fibers, such as bamboo, cotton, flax, jute, pineapple, and sugarcane bagasse, have been incorporated into composites primarily used in the automotive interior.[2, 18] Lignocellulosic natural fibers can be incorporated into rubber using standard processing techniques.[19] However, the most common rubber reinforcing fillers are carbon black (CB), which is petroleum-based and non-degradable, and silica (clay), which can be difficult to disperse in rubber.[20] Additionally, to effectively reinforce rubber, CB and silica must be present in high quantities, typically 50-70 parts per hundred rubber (phr).[21]

Conventional manufacturing of rubber involves either a two-roll mill or internal mixer to compound fillers into rubber. Curing or thermosetting processes include compression molding, injection molding, and extrusion. In cured rubber, reinforcement results in improved stiffness and hardness, as well as improved resistance to abrasion, tear, cutting, and rupture.[22] In the uncured compounds, reinforcing fillers can have a significant effect on flow properties. To achieve optimal

reinforcement, aggregate size and size distribution, surface area, and dispersion must be optimized.[23] Processing-induced flow is an important mode of dispersing and deagglomerating filler particles in filled-polymer systems. Three types of flow-induced dispersion have been studied: 1) agglomerate rupture, which occurs when the applied hydrodynamic stress is greater than the agglomerate cohesive strength, 2) erosion of small filler fragments from the agglomerate surface, and 3) collision-induced fragmentation.[24] Modeling of these dispersion mechanisms shows a linear shear rate dependency.[24, 25] Thus, shear rate is another important processing parameter to consider.

Wheat proteins can aggregate into larger structures. The aggregation behavior can be controlled to encourage the formation of preferred structures, resulting in designed functional nanomaterials with high moduli on the order of GPa.[26-28] Under denaturing conditions in aqueous solution, proteins hierarchically self-assemble into supramolecular structures consisting of perpendicularly stacked rigid β-sheet nanostructures. The conversion of low-density random coil (RC) structures to α-helical intermediates, then into high density β-sheet structures, is thought to be the universal aggregation pathway for many proteins.[29-31] A pair of stacked β-sheets is the elementary "particle" from which larger structures form. In aqueous solution, hydrophobic interactions drive the packing of β-sheet structures into larger oligomeric or fibrillar structures.[32, 33] α to β transitions have also been shown to occur spontaneously at air-water interfaces due to hydrophobic interactions with the gas phase.[34] Protein unfolding and refolding is a dynamic process which is heavily impacted by external conditions. A change in protein secondary structure has been shown to result from 1) pressure, 2) an increase in conformational entropy with heat application, 3) pH changes, 4) the introduction of denaturants, such as alcohols, 5) increasing salt concentration and, 6) interfacial denaturing conditions.[34-36]

The self-assembly of trypsin hydrolyzed wheat gluten (THWG) proteins in aqueous solution,[28, 29, 37-39] in an aqueous polymer environment,[40] and in a hydrophobic IR environment[41] has been previously studied. The focus of these studies was to confirm the existence of β-sheet aggregated structures from gliadin (Gd, a component protein of wheat gluten) and optimize the self-assembly process. Here, the composite processing was optimized to maximize the reinforcement potential, while minimizing the viscous losses, of a self-assembled wheat protein filler in a rubber composite. This was done largely by optimizing the dispersion of protein in a synthetic isoprene rubber (IR) matrix using typical rubber compounding techniques. The compounding time, temperature, and speed were varied. The protein batch preparation was also varied and the effect of the protein aggregate structure on the composite processing was determined.

## EXPERIMENTAL

### MATERIALS

Gliadin from wheat (Gd), trypsin enzyme (Type I from bovine pancreas), and slab synthetic polyisoprene rubber (IR, 97 % cis-1,4-polyisoprene) were purchased from Sigma-Aldrich (St. Louis, MO).

### METHODS

*Protein preparation: trypsin hydrolyzed gliadin (THGd).* — An aqueous dispersion of Gd (20 g in 800 mL $H_2O$) was hydrolyzed by trypsin enzyme (0.3 g) according to a previously used procedure.[41] The dispersion was gently stirred for 72 h at 37 °C and pH 8 to completely hydrolyze the protein without aggregating the peptides.[28, 38] At 72 h, the THGd hydrolysate was poured into polytetrafluoroethylene (PTFE)-coated trays and dried under a fume hood at room temperature (RT). Three different protein batches were prepared by varying the drying time and % solids in the THGd filler. Protein batches P1 and P3 contained 85% solids and differed in their

drying time; P1 was dried for 13 days and P3 was dried for 29 days. The residual water content was kept consistent in P1 and P3 by wrapping the protein trays in several layers of plastic wrap. The additional drying time for P3 was intended to increase the aggregation of THGd peptides into β-sheets and potentially larger structures, similar to a solution aggregation procedure used previously.[40, 41] Protein batch P4 contained 97% solids and was air dried at an accelerated rate by increasing the surface area of the tray. The total drying time for P4 was 5 days. The protein drying time ($t_d$) and % solids for P1, P3, and P4 batches are summarized in Table **I**, along with the composite compounding conditions.

*Compounding*. — THGd:IR composite compounds (40 g) were prepared using the following compounding temperatures and speeds: 1) 105 °C and 30 rpm, 2) 150 °C and 30 rpm, and 3) 150 °C and 60 rpm (Brabender Prep-Center with internal mixing head, Hackensack, NJ) (Table **I**). IR was mixed for 30 s prior to adding THGd. Composite compounding times ranged from 1-5 min after addition of the protein and 2 g of compounded material was removed every minute for further characterization. The temperature range (105-150 °C) was chosen so that residual water in the hydrolysate evaporated upon introduction to the internal mixing head.

*Rheology*. — Unvulcanized rubber composites were pressed under 35 kPa of pressure for 30 min prior to rheological testing. Rheological properties were characterized on AR2000 and DHR3 rheometers (TA Instruments, New Castle, DE) using 25 mm parallel plates with a fixed gap of 3 mm. Flattened samples were equilibrated for 3 min under ambient conditions then a stress sweep from 100-1000 Pa at 1 Hz was conducted to find the linear viscoelastic region. The samples were then equilibrated for an additional 3 min and a frequency sweep from 0.1 to 100 Hz at 150 Pa was conducted in the linear viscoelastic region. The storage modulus (G') and loss tangent (tan δ= G"/G') are reported where G" is the loss modulus.

*Fourier transform infrared (FTIR) spectroscopy*. — Attenuated total reflectance (ATR) FTIR spectra were acquired from 4000-525 $cm^{-1}$ with 128-scans at a resolution of 4 $cm^{-1}$ (SmartOrbit Nicolet 6700, Thermo Fisher Scientific Inc., Madison, WI). Spectra were collected in triplicate for each compound and a standard error was calculated from the absorbance average at a specific wavenumber. A 2-point baseline correction was manually performed using OMNIC v.8.1.0.10 software by setting the absorbances at 3800 and 1850 $cm^{-1}$ to zero, which were regions where neither the THGd nor IR produced an absorbance.[42]

*Scanning electron microscopy with energy dispersive X-ray spectroscopy (SEM-EDX).* — Compounds were fractured using liquid nitrogen, then sputter-coated with 5 nm iridium at a 45 ° angle. Micrographs were obtained with a 12.4 mm working distance and 10 kV accelerating voltage (FEI Quanta 600 FEG environmental SEM with a Bruker EDX Silicon Drifted Detector, Thermo Fisher Scientific, Waltham, MA). Rubber relaxation during imaging caused the iridium coating to crack and pucker, observable as black lines and striations in the SEM images. While some surface features were obscured by the cracking phenomenon, the elemental distribution was unaffected. Oxygen was exclusive to the protein phase and any Z-contrast arising from oxygen identified the protein phase. A corresponding decrease in the carbon signal intensity confirmed a protein phase domain. Protein aggregates smaller than 1 $\mu m^2$ could not be resolved by the EDX detector but could be distinguished as bright areas in the backscatter electron (BSE) micrographs using a BSE detector. Therefore, EDX elemental maps and BSE micrographs were used in conjunction to identify protein dispersion and aggregate morphology. Protein aggregates and agglomerates were measured using ImageJ software. Measurements were made in BSE micrographs of the fracture surface at four magnifications (100x, 500x, 1000x, 5000x). The agglomerate sizes did not follow a normal distribution and so outliers were removed. Outliers

were defined as any measurements that fell below $Q_1$-1.5*IQR or above $Q_3$+1.5*IQR, where $Q_1$ and $Q_3$ were the first and third quartile, respectively, and IQR was the interquartile range. A mean agglomerate length (L), width (w), and aspect ratio (AR=L/w), were calculated for the remaining measurements and reported with standard error.

## RESULTS AND DISCUSSION

### RHEOLOGICAL PROPERTIES AS A FUNCTION OF PROCESSING CONDITIONS

The effect of the processing parameters, such as compounding speed, time, and temperature, on the IR controls and THGd:IR composites was evaluated. In the IR control compounded at 150 °C and 30 rpm, i.e., IR(150/30), storage modulus (G') decreased and tan δ increased as a function of compounding time (Figure 1). The decrease in G' with compounding time was most pronounced at low angular frequencies ($\omega < 5$ rad/s), and was nearly negligible at high values of ω. The loss of stiffness and increase in the loss tangent, i.e., viscous dissipation, with compounding time was indicative of rubber degradation or loss of molecular weight through a chain scission mechanism.[43, 44] Degradation in the IR control was increased with compounding speed and temperature, leading to a lower G' and higher tan δ (Figure 2). In the IR control compounded for 5 minutes at high temperature (150 °C) and speed (60 rpm), i.e., IR(150/60), the G' was the lowest and tan δ was the highest of the IR controls (Figure 2). As temperature and speed were lowered to 105 °C and 30 rpm, the IR(105/30) control G' was increased and tan δ decreased. For the composites compounded at an elevated temperature of 150 °C, i.e., THGd-P1(150/30), THGd-P4(150/30), THGd-P1(150/60), and THGd-P3(150/60), THGd had a reinforcing effect on the IR modulus.[41] However, compounding of the filled system at a low temperature of 105 °C, i.e., THGd-P1(105/30), resulted in a modulus decrease with the addition of the protein to the rubber matrix. This has been shown to occur in systems where the filler

aggregate size is large.[45] Since minimal rubber degradation was observed for low temperature compounding of the IR(105/30) control, the modulus decrease in the THGd-P1(105/30) composite could have resulted from poor dispersion of the THGd phase through the high molecular weight IR matrix. The morphology of the protein agglomerates in THGd-P1(105/30) and other composites was analyzed by SEM-EDX and corroborated this hypothesis (see section below: Morphological changes as a function of processing conditions.). It is well known that the rheological properties of filled rubbers are sensitive to filler volume fraction, structure, shape, dispersion, and surface properties.[46]

The effect of the compounding temperature (T) on the rheological properties of the THGd:IR composites was evaluated at a constant compounding speed of 30 rpm using the protein processing method, P1 (85% solids, $t_d$ = 13 d) (Figure 3a). At a low compounding temperature of 105 °C in the composite, G' was increased and tan δ was decreased as a function of compounding time. This was opposite the behavior observed in the IR control (Figure 1). However, the G' of the composite THGd-P1(105/30) at 5 min compounding was still inferior to the neat rubber compounded at T = 105 °C (Figure 2a). Conversely, at a high compounding temperature of T = 150 °C, the rheological behavior of the THGd-P1(150/30) composite followed that of the IR control, where G' generally decreased and tan δ increased as a function of compounding time. Thus, a shorter compounding time of 1-2 minutes was favorable to G' and tan δ at a high compounding temperature (T = 150 °C), while a longer compounding time of 3-5 min was preferred at a lower compounding temperature (T = 105 °C). These results suggested that an interaction effect existed between the compounding time and temperature, i.e., one parameter was dependent upon the other. It is also important to note that only high temperature compounding resulted in a reinforced IR matrix. At a higher compounding temperature, where greater IR

degradation was observed, the addition of the THGd protein filler maintained the composite storage modulus, while a loss of properties in the IR matrix occurred.

The effect of compounding speed on the rheological properties of the THGd:IR composites was evaluated at a constant temperature of 150 °C using protein processing method P1 (Figure 3b). Similar trends in modulus and tan δ were observed for compounding speeds of 30 and 60 rpm, where G' generally decreased and viscous dissipation increased as a function of compounding time. A maximum G' was observed after 2 minutes of compounding for both composites, i.e., THGd-P1(150/30) and THGd-P1(150/60). Overall, the change in G' as it related to compounding speed was minor compared to other processing-related changes in modulus. However, the change in tan δ as it related to compounding speed was significant, where a faster compounding speed increased viscous dissipation. Tan δ is an important parameter in tire rubber applications, where a low tan δ is necessary to reduce heat build-up in the tire, which lowers fuel economy.[47] In all cases, the THGd:IR composites had lower viscous dissipation than the IR control compounded at the same speed and temperature (Figure 2b), which was a desirable result.[48] Tan δ was mainly found to increase as a function of compounding temperature, time, and speed. The increase in tan δ was consistent with degradation in the rubber matrix because lower molecular weight IR chains increased the molecular mobility, allowing for more viscous dissipation.[49, 50] Therefore, the addition of THGd protein was able to mitigate the unfavorable effects of processing on the IR phase, such as loss of storage modulus and increase in tan δ. The modulus was primarily affected by compounding temperature, with a lesser impact from compounding time and speed. For all compounds, regardless of compounding temperature and speed, the rheological properties decreased by 5 minutes of compounding.

The protein preparation, i.e. batch P1, P3, or P4, was also influential on the modulus (Figures 2, 3c and 3d). By increasing the %solids, as in the case of P4 (97% solids, $t_d$ = 5 d), or encouraging protein aggregation, as in the case of P3 (85% solids, $t_d$ = 29 d), an increase in modulus and decrease in viscous dissipation was observed. An increase in protein aggregation was achieved by allowing THGd-P3 to "self-assemble" in aqueous solution (85% solids) for an additional 16 days at room temperature (compared to P1, 85% solids, $t_d$=13 d).

The ease of compounding was affected by the protein batch preparation. A decrease in the residual water content and a higher %solids in the filler (P4, 97% solids, compared to P1, 85% solids) improved ease of compounding. THGd-P4 protein was incorporated into the IR phase readily and good mixing was achieved upon introduction of THGd into the compounder. The increase in residual water in the P1 protein increased the mixing difficulty, and THGd-P1 initially coated the rubber surface without any mixing/shearing occurring during the first minute, which is why the storage modulus for THGd-P1(150/30) was similar to the IR(150/30) control (Figure 3c). The aggregated P3 protein batch (85% solids, $t_d$=29 d) was the most difficult to incorporate into IR, even with high temperature (T = 150 °C) and shear (60 rpm) conditions. To achieve good mixing, the THGd-P3(150/60) composite compound was removed and re-fed into the mixing bowl during the first 2 minutes until shearing was observed. Despite the processing difficulties, the final properties of THGd-P3(150/60) were favorable, and the composite had a higher G' and lower tan δ than THGd-P1(150/60). To see if the composite properties would continue to decline beyond 5 minutes of compounding, THGd-P3(150/60) was mixed for an additional minute. A steeper decline in G' and increase in tan δ from 5-6 minutes confirmed that any favorable processing-induced effects on the composite properties had occurred during the initial 4 minutes of compounding. The improved IR reinforcement of dry P4 protein was eliminated by 5 minutes of

compounding, where a sharp decline in G' occurred. An optimal compounding time of 2 minutes produced the best combination of good mixing, high G' and low tan δ for composites compounded at T=150 °C. From these results, it can be concluded that drying THGd at a slower rate to a high %solids would produce the greatest reinforcing effect on IR while also improving the ease of compounding.

### MORPHOLOGICAL CHANGES AS A FUNCTION OF PROCESSING CONDITIONS

The protein dispersion throughout the fracture surface was best assessed in low magnification SEM micrographs using the oxygen EDX maps, where contrast in the oxygen EDX map, i.e., bright blue spots, were indicative of protein agglomerates. As the protein phase dispersed and the agglomerates approached nanoscale dimensions, the EDX detector was unable to map individual aggregates. Thus, micrographs obtained using the backscatter electron (BSE) detector were used to resolve aggregates and small agglomerates, in which the protein phase appeared brighter than the rubber due to the presence of higher atomic number elements (mainly oxygen). Additionally, protein domains were often surrounded by surface puckering as the adjacent rubber phase relaxed under the electron beam. The morphological differences between the minor (protein) phase and major (rubber) phase were used to identify the protein domains in high magnification images.

The composite morphology was analyzed as a function of compounding time for THGd-P1(105/30), THGd-P1(150/30), THGd-P1(150/60), and THGd-P3(150/60) (Figures 4-5). From Figure 4, it was apparent that protein dispersion increased as a function of compounding time for all composites. In general, the majority of protein dispersion in the composites occurred from 1-2 minutes of compounding and, by 3-5 minutes, a well-dispersed protein phase was observed. During the initial 2-minute compounding period, large agglomerates were progressively broken

into smaller agglomerates and dispersed within the rubber matrix. The largest agglomerates were observed in the composite compounded at low temperature, i.e., THGd-P1(105/30) (Figure 4a), and in the composite compounded with the highly aggregated protein phase, i.e., THGd-P3(150/60) (Figure 4d). Both still had larger agglomerates than the other composites at 5 minutes of compounding. At a compounding temperature of 150 °C, both compounding speeds (30 and 60 rpm) resulted in good protein dispersion by 5 min of compounding, as observed by the uniform distribution of bright spots in the oxygen EDX maps (Figures 4b and 4c, right column). In addition to deagglomeration and dispersion, changes in agglomerate aspect ratio were observed with compounding time (Figure 5). After 1-2 minutes of compounding THGd-P1(150/60), large anisotropic protein agglomerates were observed (Figure 5, 1 and 2 minutes). By 3 minutes of compounding, the agglomerates were ellipsoidal and much of the anisotropy in the protein phase was gone (Figure 5, 3 minutes). At 5 minutes of compounding, the protein domains were approximately isotropic and well-dispersed throughout the surface (Figure 5, 5 minutes).

To quantitatively analyze the evolution of protein dispersion with compounding time, measurements of the average agglomerate and aggregate sizes for the samples in Figure 4 were obtained from SEM micrographs using Image J software (Figure 6). Average agglomerate width, length (not shown, same trend as width), and aspect ratio (AR = length/width) were calculated (Figure 7). Measurements were made in multiple micrographs of different magnifications collected from different areas of the fracture surface. Agglomerates were defined as protein domains on the order of 1-100 μm.[22] During the initial compounding stage (t =1-2 min), the largest agglomerates were observed in THGd-P1(105/30) (Figure 7a), which was compounded at the lowest temperature and had the lowest elastic modulus. In the above section, “Rheological properties as a function of processing conditions,” it was hypothesized that a decrease in the composite G' relative to the

IR(105/30) control arose from poor dispersion of THGd in IR. These SEM-EDX results corroborate that hypothesis. By increasing the compounding temperature from 105 °C to 150 °C, a 70% reduction in the initial (1 min) and final (5 min) agglomerate width was observed. There was no definitive effect of compounding speed on the composite morphology or the protein domain size for THGd-P1(150/30) and THGd-P1(150/60) by 5 min of compounding (Figures 4b, 4c, and 7a). In the sample containing aggregated protein, i.e., THGd-P3(150/60), a 150% increase in agglomerate size over THGd-P1(150/60), compounded at the same temperature and speed, was observed. The P3 aggregated protein was the most resistant to deagglomeration. From 1 to 5 minutes of compounding, an 80% reduction in protein agglomerate size was observed in THGd-P3(150/60), compared to a 90% agglomerate size reduction in the composites with the less aggregated protein, P1. Additionally, THGd-P3(150/60) was the only compound where an increase in agglomerate width was observed during compounding (from 2 to 3 minutes) (Figure 7a). In general, the agglomerate aspect ratio (AR) was found to increase with every 2 minutes of compounding (Figure 7b). The cyclical increase/decrease in AR with compounding time, combined with the increase in agglomerate width at 3 minutes for THGd-P3(150/60), suggested a dynamic network of aggregates, where rearrangements were possible.

Individual nanoscale aggregates with an average width of 64±11 nm, length of 276±9 nm, and AR of 4.3±0.1 were observed in THGd-P1(105/30) at 4 and 5 minutes of compounding (Figure 6). The aggregates, or "primary particles," shown in Figure 6 were agglomerated into larger, heterogeneous structures, or "agglomerates", which were characterized in Figure 7. In a previous report[41], and in the composites compounded at 150 °C in this report, it was not possible to resolve individual aggregates within an agglomerate. The degraded rubber phase relaxed quickly, obscuring the protein surface, cracking the Iridium coating, and causing the image to drift. In

THGd-P1(105/30), degradation of the IR matrix was mitigated by the low compounding temperature and high magnification micrographs were obtained at different compounding times. As shown in the inset of Figure 6, aggregates were oriented in different directions and area density varied throughout the fracture surface. The smallest agglomerates contained as few as 2-3 aggregates, while the largest had hundreds or thousands of aggregates. Although the agglomerates were heterogeneous in size and shape, the protein aggregates were very uniform in size, shape, and AR.

### PROTEIN STRUCTURE AND CONFORMATION AS A FUNCTION OF PROCESSING CONDITIONS

The FTIR spectra were normalized to the γ(C=C-H) absorbance at 840 $cm^{-1}$, which absorbed strongly in the IR phase and was attributed to the wagging deformation of the cis-1,4-addition in isoprene rubber (Figure 8).[51-55] The protein absorbances, i.e., Amide A, I, and II, were largely unencumbered by IR absorbances, except for a small absorbance at 1664 $cm^{-1}$ which was attributed to ν(C=C) in the $C(CH_3)$=CH- group of IR.[53, 55] The Amide A stretching ν(NH) absorbance at 3300-3270 $cm^{-1}$ arose from hydrogen bonding in the NH group and was independent of any conformational changes in the protein backbone.[56] Information about the protein secondary structure conformation (e.g., α-helix, β-sheet, β-turn, and random coil) was contained in the Amide I and II vibrational modes because peptide groups with different through-space and through-bond coupling absorb differently.[57] The Amide I mode (1700-1600 $cm^{-1}$) was attributed to carbonyl stretching (ν(C=O), 80%) and, to a lesser extent, stretching of the C-N bond (ν(CN), 20%). The Amide II mode was more convoluted, with primary contributions from N-H bending (δ(NH), 60%) and secondary contributions from C-N stretching (ν(CN), 40%).[58] The Amide I mode is more reliable because it has much less influence from protein side chains, and so was used for secondary structure determination.[56]

Contributions from peptide aggregation were also contained in the Amide I mode.[59] Intermolecular β-sheet packing absorbs from 1630-1610 $cm^{-1}$ and this region has been termed the "aggregation band".[60, 61] In the neat THGd protein, the strongest Amide I absorbance was at 1625 $cm^{-1}$, indicating a fully-aggregated protein (Figure 8).[39] The IR control did not absorb in the aggregated β-sheet band at 1625 $cm^{-1}$. Therefore, an average of the 1625 $cm^{-1}$ absorbance intensity ($I_{1625}$ ± standard error) after normalization to the IR 840 $cm^{-1}$ γ(C=C-H) absorbance was calculated as a function of compounding time and used to assess changes in protein β-sheet aggregation with processing (Figure 9). A decrease in THGd aggregation was observed as a function of compounding time, which confirmed the SEM/EDX observations that large protein agglomerates break-down and that those agglomerates were largely composed of aggregated β-sheets. β-sheet agglomerate breakup was most aggressive during the initial 1-2 minutes of compounding. By 3 minutes of compounding, $I_{1625}$ generally plateaued, indicating a threshold beyond which protein β-sheets resisted breakup. β-sheets have been shown to be very thermally stable[62-66] and rubber compounding has been shown to preserve β-sheet structure.[41] The $I_{1625}$ threshold indicated that large protein agglomerates were composed of strongly cohesive "primary particles".[67] In this case, only primary particles composed of aggregated β-sheets were retained and unchanged during compounding and, as SEM/EDX shows, these particles were on the nanometer scale (Figure 4).

The processing parameters had a significant effect on the amount of β-sheet aggregation. In the THGd-P3(150/60) composite containing pre-aggregated protein (85% solids, $t_d$=29 d), $I_{1625}$ did not plateau at 3 minutes but, instead, increased at 3 minutes, showing a processing induced reaggregation that eventually disappeared at longer compounding times (Figures 9 and 10). The reaggregation behavior was also observed as an increase in average agglomerate width in SEM-EDX (Figure 7a). The reaggregated state negatively impacted the rheological properties of the

compound and a decrease in modulus was observed for THGd-P3(150/60) at 3 minutes (Figure 3d). THGd-P3(150/60) at 1 minute had a lower amount of β-sheet aggregation than THGd-P1(150/60) compounded at the same conditions, but the P3 compound maintained a higher β-sheet content later in compounding. Combined with the SEM-EDX data this suggested that THGd-P3(150/60) did have a fair amount of peptide aggregation from the P3 preparation conditions that persisted through compounding. The P4 protein batch (97% solids, $t_d$ = 5 d) behaved most consistently throughout the compounding period and was more resistant to aggregate breakdown than the P1 protein batch (85% solids, $t_d$ = 13 d) compounded under the same conditions. This suggested that a short drying time was kinetically favorable to forming many smaller protein agglomerates that were closer to the primary particle size, while a longer drying time allowed the formation of much larger agglomerates of primary β-sheet particles that eventually broke down. Lower temperature compounding (105 °C) preserved β-sheet aggregates more than compounding at 150 °C for the 5-minute processing period, confirming the SEM/EDX results that showed larger agglomerates for this compound. The compounding speed had a negligible effect on β-sheet aggregation past the first minute, which was also observed in SEM-EDX.

## CONCLUSIONS

The mechanical, structural, and morphological properties of trypsin hydrolyzed gliadin-synthetic isoprene rubber (THGd:IR) compounds were characterized with rheology, Fourier transform infrared spectroscopy (FTIR), and scanning electron microscopy with energy dispersive x-ray spectroscopy (SEM-EDX). The composite properties were primarily governed by the processing temperature, compounding time, and protein batch preparation. The compounding speed had a minor effect on the properties. A highly agglomerated protein phase negatively impacted the composite rheological properties, as seen by a decrease in elastic modulus. Good

dispersion and deagglomeration of THGd in IR was observed for those compounds processed at 150 °C, resulting in an elastic modulus greater than the IR control. In all compounds, the addition of THGd was found to decrease viscous dissipation over the control, observable as a decrease in tan δ in the composite compounds. The protein aggregate aspect ratio (AR) cyclically increased/decreased as a function of compounding time as agglomerate size decreased, suggesting dynamic rearrangements of protein aggregates was occurring during compounding. The protein agglomerates were made of nanoscale "primary particles", which contained aggregated protein β-sheets, as observed in SEM-EDX and FTIR. The protein reinforcement of IR was improved by increasing the %solids in the THGd hydrolysate or by aggregating THGd through an extended drying process. The THGd protein with a high %solids (batch P4) was easily incorporated into the IR phase during compounding, while the aggregated THGd (batch P3) was difficult to compound. Thus, a combination of slow drying THGd to a high %solids would likely produce the greatest reinforcing effect on IR while also improving the ease of compounding. This study demonstrated that, through the careful selection of processing parameters, uniform protein dispersion and optimal IR reinforcement were achievable.

## ACKNOWLEDGEMENT

This work was supported by United States Department of Agriculture National Institute of Food and Agriculture, AFRI project [grant number USDA-2016-67021-25006].

## REFERENCES

1. S. Rwawiire, B. Tomkova, J. Militky, A. Jabbar and B. M. Kale, *Composites Part B* **81**, 149, (2015).

2. R. Dunne, D. Desai, R. Sadiku and J. Jayaramudu, *J. Reinf. Plast. Compos.* **35**, 1041, (2016).

3. J. Holbery and D. Houston, *JOM* **58**, 80, (2006).

4. F. X. Espinach, L. A. Granda, Q. Tarrés, J. Duran, P. Fullana-i-Palmer and P. Mutjé, *Composites Part B* **116**, 333, (2017).

5. *D3182-16 Standard Practice for Rubber-Materials, Equipment, and Procedures for Mixing Standard Compounds and Preparing Standard Vulcanized Sheets*, ASTM International, West Conshohocken, PA, 2016.

6. E. Warren-Thomas, P. M. Dolman and D. P. Edwards, *Conserv. Lett.* **8**, 230, (2015).

7. K. Soratana, D. Rasutis, H. Azarabadi, P. L. Eranki and A. E. Landis, *J. Clean. Prod.* **159**, 271, (2017).

8. T. Phakkeeree, Y. Ikeda, H. Yokohama, P. Phinyocheep, R. Kitano and A. Kato, *J. Fiber Sci. Technol.* **72**, 160, (2016).

9. A. Kato, A. Tohsan, S. Kohjiya, T. Phakkeeree, P. Phinyocheep and Y. Ikeda, "12 - Manufacturing and Structure of Rubber Nanocomposites," in *Progress in Rubber Nanocomposites*, Woodhead Publishing, 2017.

10. W. Smitthipong, S. Suethao, D. Shah and F. Vollrath, *Polym. Test.* **55**, 17, (2016).

11. N. Hariwongsanupab, S. Thanawan, T. Amornsakchai, M.-F. Vallat and K. Mougin, *Polym. Test.* **57**, 94, (2017).

12. R. Wang, J. Zhang, H. Kang and L. Zhang, *Composites Sci. Technol.* **133**, 136, (2016).

13. S. Canepari, P. Castellano, M. L. Astolfi, S. Materazzi, R. Ferrante, D. Fiorini and R. Curini, *Environ. Sci. Pollut. Res.* **25**, 1448, (2018).

14. B. Kc, O. Faruk, J. A. M. Agnelli, A. L. Leao, J. Tjong and M. Sain, *Composites Part A* **83**, 152, (2016).

15. G. Park and H. Park, *Compos. Struct.* **184**, 800, (2018).

16. S. S. Yang, N. Nasr, S. K. Ong and A. Y. C. Nee, *J. Clean. Prod.* **153**, 570, (2017).

17. M. Despeisse, Y. Kishita, M. Nakano and M. Barwood, *Procedia CIRP* **29**, 668, (2015).

18. F. M. Al-Oqla, S. Sapuan, M. Ishak and A. Nuraini, *J. Compos. Mater.* **50**, 543, (2016).

19. Y. Zhou, M. Fan, L. Chen and J. Zhuang, *Composites Part B* **76**, 180, (2015).

20. J. Ma, L.-Q. Zhang and L. Geng, "Manufacturing Techniques of Rubber Nanocomposites," in *Rubber Nanocomposites: Preparation, Properties, and Applications*, S. Thomas and R. Stephen, Eds., John Wiley & Sons (Asia) Pte Ltd, Singapore, 2009.

21. L. Tzounis, S. Debnath, S. Rooj, D. Fischer, E. Mäder, A. Das, M. Stamm and G. Heinrich, *Mater. Des.* **58**, 1, (2014).

22. J. L. Leblanc, *Prog. Polym. Sci.* **27**, 627, (2002).

23. B. Erman, J. E. Mark and C. M. Roland, *The Science and Technology of Rubber*, 4 edn., Elsevier Academic Press, Boston, 2013.

24. O. Seyvet and P. Navard, *J. Appl. Polym. Sci.* **78**, 1130, (2000).

25. B. Olalla, C. Carrot, R. Fulchiron, I. Boudimbou and E. Peuvrel-disdier, *Rheol. Acta* **51**, 235, (2012).

26. T. P. J. Knowles and M. J. Buehler, *Nat. Nanotechnol.* **6**, 469, (2011).

27. D. M. Ridgley, E. C. Claunch, P. W. Lee and J. R. Barone, *Biomacromolecules* **15**, 1240, (2014).

28. D. M. Ridgley, K. C. Ebanks and J. R. Barone, *Biomacromolecules* **12**, 3770, (2011).

29. E. C. Claunch, D. M. Ridgley and J. R. Barone, *Composites Sci. Technol.*, (2015).

30. A. Nabers, J. Ollesch, J. Schartner, C. Kötting, J. Genius, U. Haußmann, H. Klafki, J. Wiltfang and K. Gerwert, *J. Biophotonics* **9**, 224, (2016).

31. A. D. Surowka, M. Pilling, A. Henderson, H. Boutin, L. Christie, M. Szczerbowska-Boruchowska and P. Gardner, *Analyst* **142**, 156, (2017).

32. E. Cerf, R. Sarroukh, S. Tamamizu-Kato, L. Breydo, S. Derclaye, Y. F. Dufrêne, V. Narayanaswami, E. Goormaghtigh, J.-M. Ruysschaert and V. Raussens, *Biochem. J.* **421**, 415, (2009).

33. D. Ghosh, P. K. Singh, S. Sahay, N. N. Jha, R. S. Jacob, S. Sen, A. Kumar, R. Riek and S. K. Maji, *Sci. Rep.* **5**, 9228, (2015).

34. F. Y. Yohko, *J. Phys.: Condens. Matter* **24**, 503101, (2012).

35. Y. L. Jeyachandran, E. Mielczarski, B. Rai and J. A. Mielczarski, *Langmuir* **25**, 11614, (2009).

36. L. Yu, L. Zhang and Y. Sun, *J. Chromatogr. A* **1382**, 118, (2015).

37. A. I. Athamneh and J. R. Barone, *Smart Mater. Struct.* **18**, 104024, (2009).

38. D. M. Ridgley, E. C. Claunch and J. R. Barone, *Soft Matter* **8**, 10298, (2012).

39. D. M. Ridgley, E. C. Claunch and J. R. Barone, *Appl. Spectrosc.* **67**, 1417, (2013).

40. B. L. DeButts, C. R. Spivey and J. R. Barone, *ACS Sustain. Chem. Eng.* **6**, 2422, (2018).

41. B. L. DeButts, L. E. Hanzly and J. R. Barone, *J. Appl. Polym. Sci.* **135**, 46026, (2018).

42. H. Yang, S. Yang, J. Kong, A. Dong and S. Yu, *Nat. Protoc.* **10**, 382, (2015).

43. X. Cheng, P. Song, X. Zhao, Z. Peng and S. Wang, *Waste Manage.* **71**, 301, (2018).

44. J. Zhao, R. Yang, R. Iervolino, B. van der Vorst and S. Barbera, *Polym. Degrad. Stab.* **115**, 32, (2015).

45. A. Dufresne, "Natural Rubber Green Nanocomposites," in *Rubber Nanocomposites: Preparation, Properties, and Applications*, S. Thomas and R. Stephen, Eds., John Wiley & Sons (Asia) Pte Ltd, Singapore, 2009.

46. P. Cassagnau and C. Barrès, "Rheological Behavior of Rubber Nanocomposites," in *Rubber Nanocomposites: Preparation, Properties, and Applications*, S. Thomas and R. Stephen, Eds., John Wiley & Sons (Asia) Pte Ltd, Singapore, 2009.

47. S. Kawasaki and T. Hattori, *U.S. Pat.*, 7919553, 2011.

48. H. M. Laun, *Rheol. Acta* **42**, 295, (2003).

49. R. Chollakup, P. Suwanruji, R. Tantatherdtam and W. Smitthipong, *J. Polym. Res.* **26**, 37, (2019).

50. R. Daik, S. Bidol and I. Abdullah, *Malays. Polym. J.* **2**, 29, (2007).

51. G. Craciun, E. Manaila and M. D. Stelescu, *Materials* **9**, 999, (2016).

52. S. Gunasekaran, R. K. Natarajan and A. Kala, *Spectrochim. Acta, Part A* **68**, 323, (2007).

53. S. Rolere, S. Liengprayoon, L. Vaysse, J. Sainte-Beuve and F. Bonfils, *Polym. Test.* **43**, 83, (2015).

54. J. L. Binder, *J. Polym. Sci., Part A: Polym. Chem.* **1**, 37, (1963).

55. D. Agostini, C. Constantino and A. E. Job, *J. Therm. Anal. Calorim.* **91**, 703, (2008).

56. A. Barth, *Biochim. Biophys. Acta* **1767**, 1073, (2007).

57. H. Torii, *J. Phys. Chem. Lett.* **3**, 112, (2012).

58. Q. Peng, N. A. Khan, Z. Wang and P. Yu, *J. Dairy Sci.* **97**, 446, (2014).

59. A. Adochitei and G. Drochioiu, *Rev. Roum. Chim.* **56**, 783, (2011).

60. F.-X. Theillet, A. Binolfi, T. Frembgen-Kesner, K. Hingorani, M. Sarkar, C. Kyne, C. Li, P. B. Crowley, L. Gierasch and G. J. Pielak, *Chem. Rev.* **114**, 6661, (2014).

61. K. Nyemb, C. Guérin-Dubiard, S. Pézennec, J. Jardin, V. Briard-Bion, C. Cauty, S. M. Rutherfurd, D. Dupont and F. Nau, *Food Hydrocoll.* **54**, 315, (2016).

62. J. Safar, P. P. Roller, D. C. Gajdusek and C. J. Gibbs, *Protein Sci.* **2**, 2206, (1993).

63. C. Dirix, F. Meersman, C. E. MacPhee, C. M. Dobson and K. Heremans, *J. Mol. Biol.* **347**, 903, (2005).

64. F. Meersman and C. M. Dobson, *Biochim. Biophys. Acta* **1764**, 452, (2006).

65. L. Adler-Abramovich, M. Reches, V. L. Sedman, S. Allen, S. J. Tendler and E. Gazit, *Langmuir* **22**, 1313, (2006).

66. F. Cordier and S. Grzesiek, *J. Mol. Biol.* **317**, 739, (2002).

67. S. Bar-Chaput and C. Carrot, *Rheol. Acta* **45**, 339, (2006).

**Table 1.** THGd-IR composite processing parameters.

| Compound | Compounding temp., (°C) | Compounding speed (rpm) | THGd drying time, $t_d$ (d) | Solids content in THGd (%) |
|---|---|---|---|---|
| THGd-P1(105/30) | 105 | 30 | 13 | 85 |
| THGd-P1(150/30) | 150 | 30 | 13 | 85 |
| THGd-P4(150/30) | 150 | 30 | 5 | 97 |
| THGd-P1(150/60) | 150 | 60 | 13 | 85 |
| THGd-P3(150/60) | 150 | 60 | 29 | 85 |

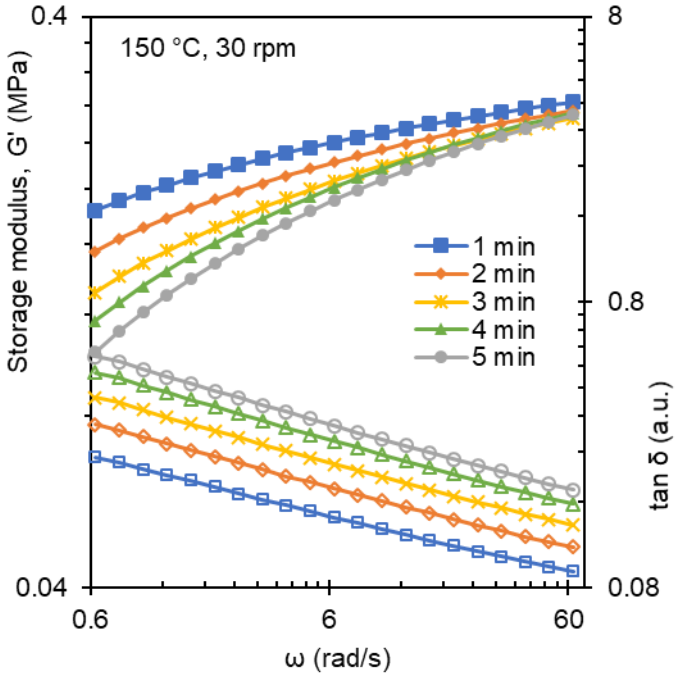


**Figure 1.** – Storage modulus (G', solid symbols) and viscous dissipation (tan δ, open symbols) as a function of angular frequency (ω) in the IR control compounded at 30 rpm and 150 °C from 1-5 minutes.

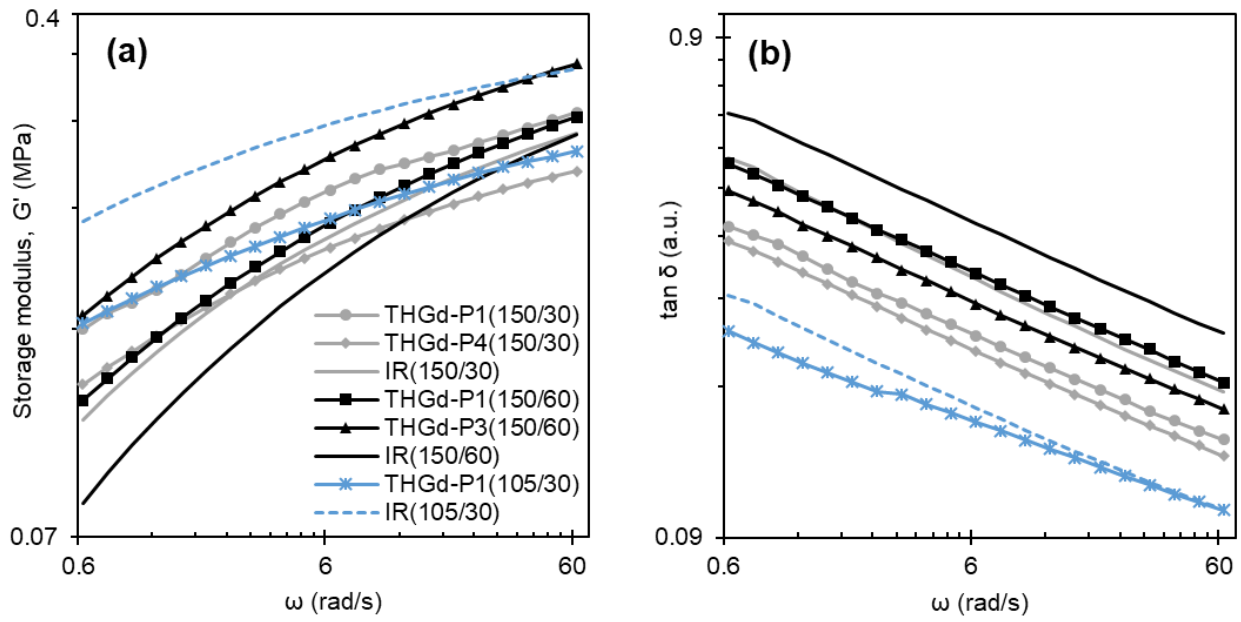


**Figure 2.**– (a) Storage modulus (G') and (b) tan δ as a function of angular frequency (ω) for IR controls (lines only) and THGd composites (lines with markers) compounded for 5 minutes at different speeds and/or temperatures.

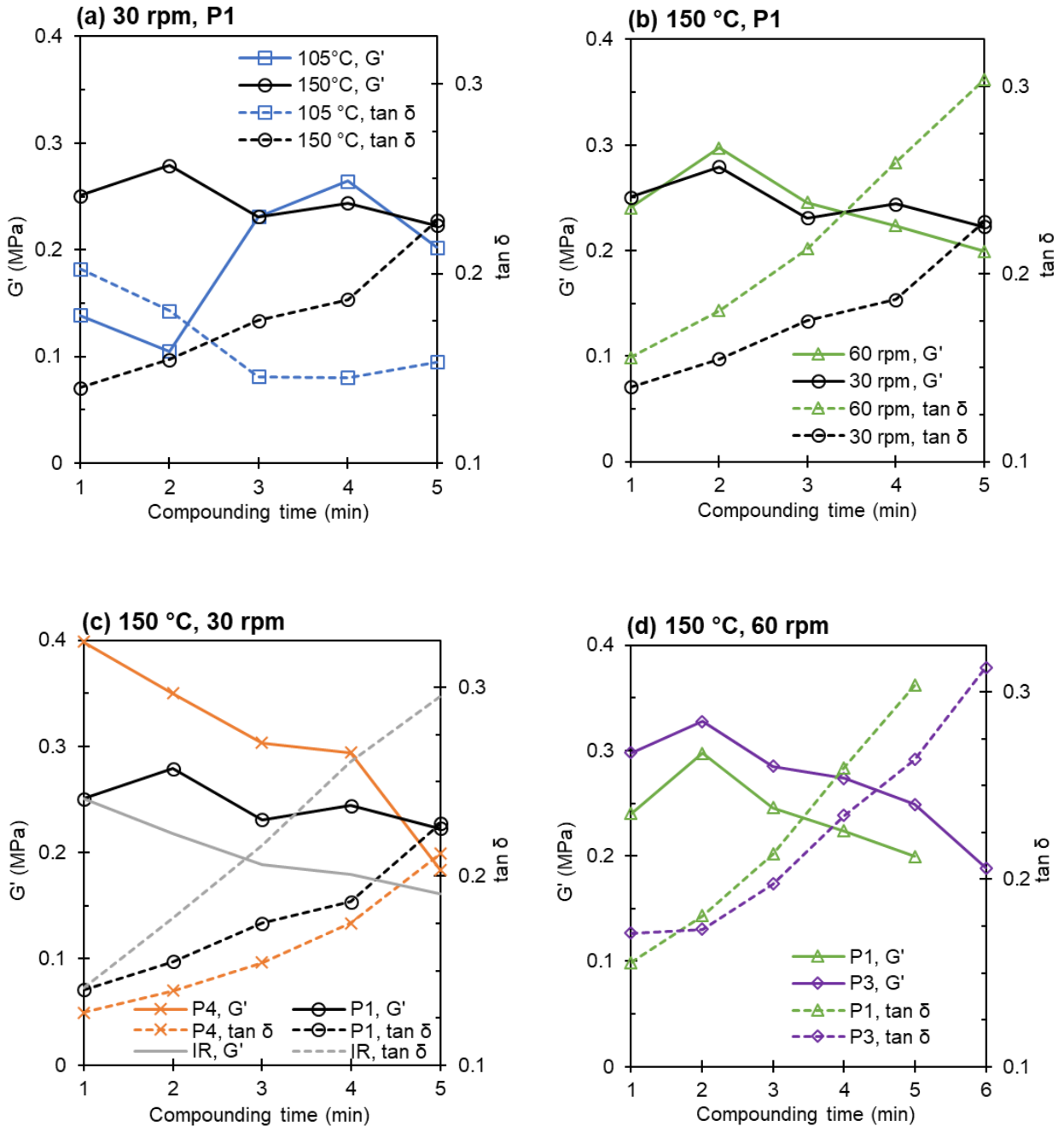


**Figure 3.** – Storage modulus, G' (solid lines), and tan δ (dashed lines) at 6.28 rad/s=1 Hz versus compounding time for THGd:IR composites compounded at constant: (a) speed (30 rpm) and protein batch (P1), (b) temperature (150 °C) and protein batch (P1), (c) temperature (150 °C) and speed (30 rpm), and (d) temperature (150°C) and speed (60 rpm).

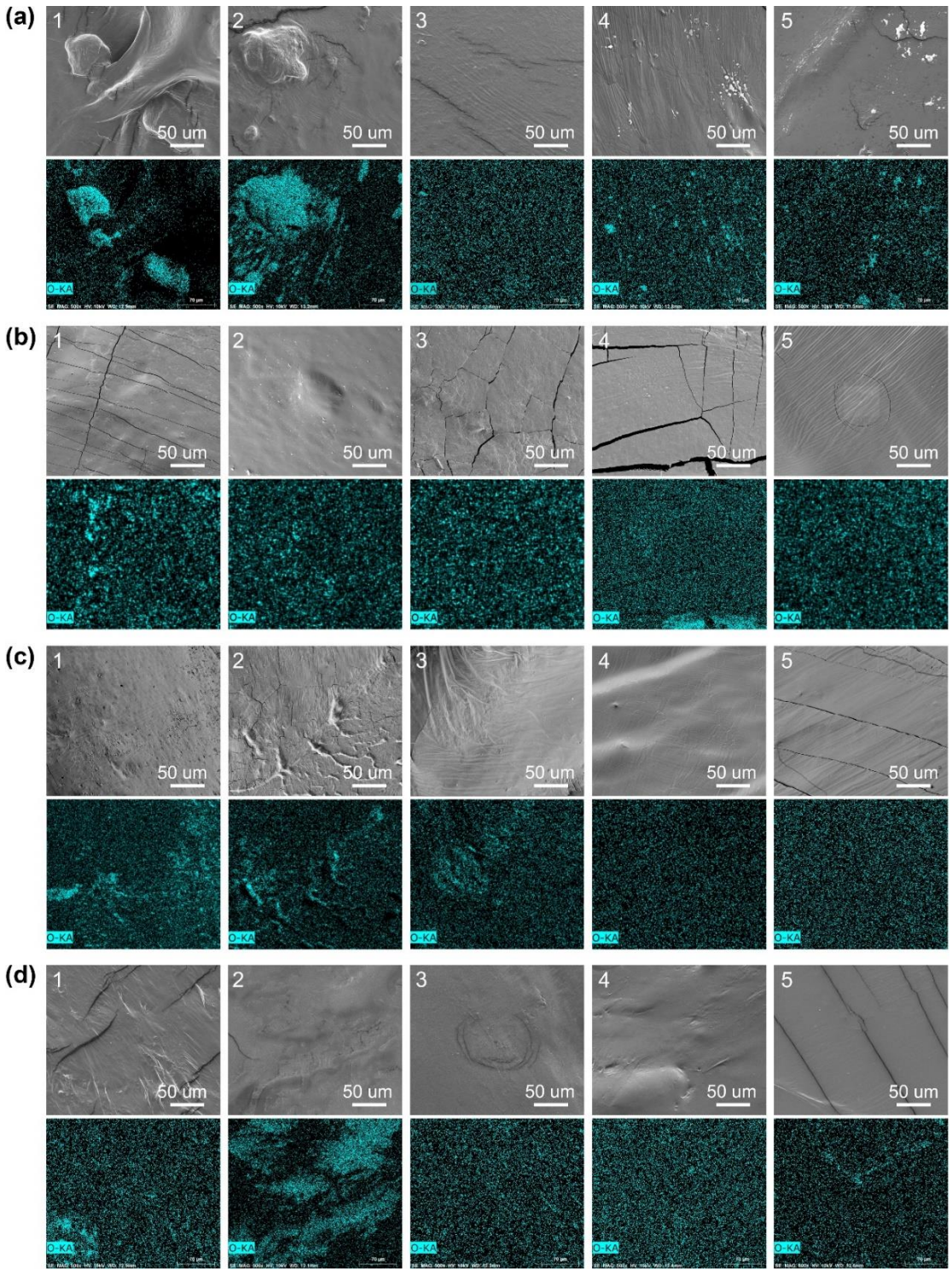


**Figure 4.** – SEM and EDX oxygen maps for: (a) THGd-P1(105/30), (b) THGd-P1(150/30), (c) THGd-P1(150/60) and, (d) THGd-P3(150/60), compounded for 1-5 minutes (from left to right).

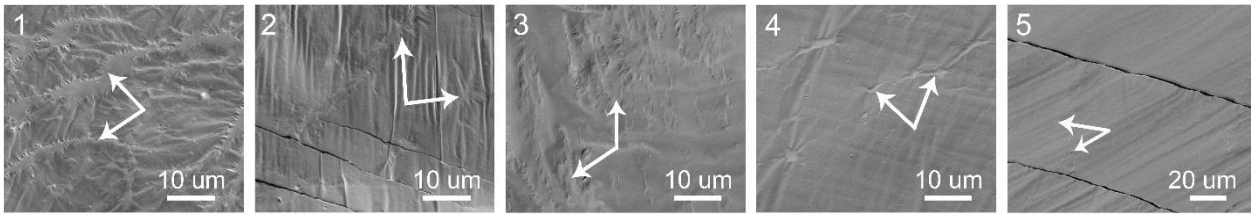


**Figure 5.** – SEM micrographs of THGd-P1(150/60 rpm) after compounding for 1, 2, 3, 4, and 5 minutes (from left to right) with arrows identifying typical protein domains. Note the scale bar change for 5 minutes of compounding.

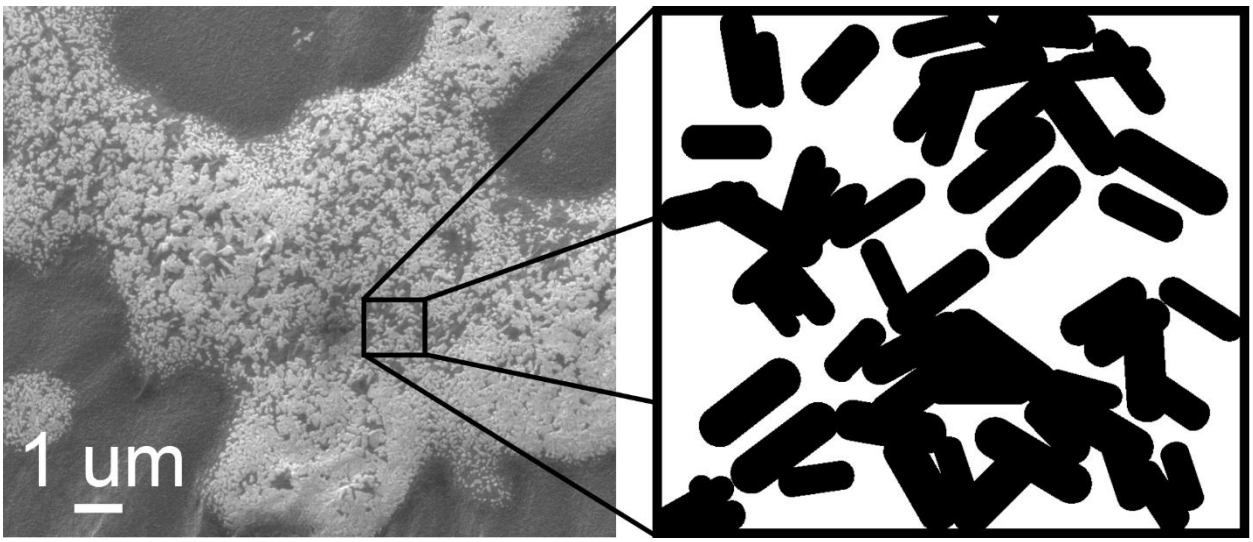


**Figure 6.** – High magnification SEM micrograph of THGd-P1(105/30), compounded for 5 minutes. Black ellipses represent individual aggregates populating a surface area of 1 $\mu m^2$ within a larger THGd agglomerate.

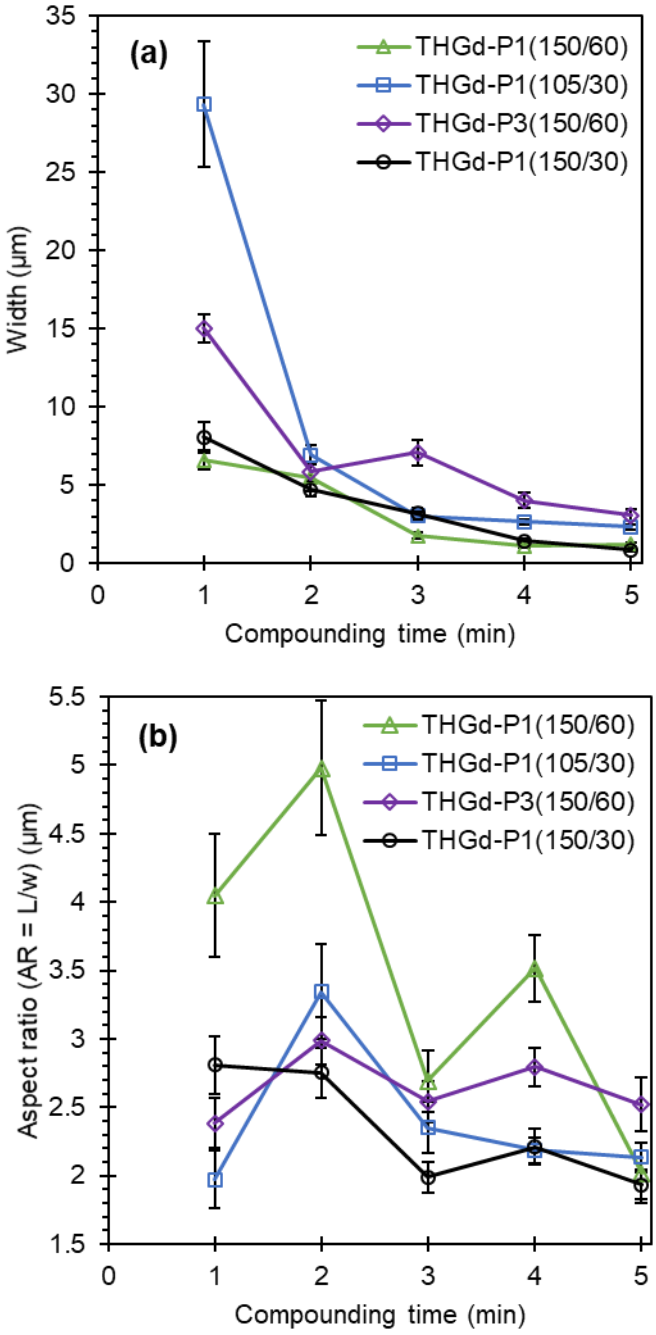


**Figure 7.** – Average agglomerate (a) width, and, (b) aspect ratio (AR=length/width), with standard error, as measured in SEM micrographs.

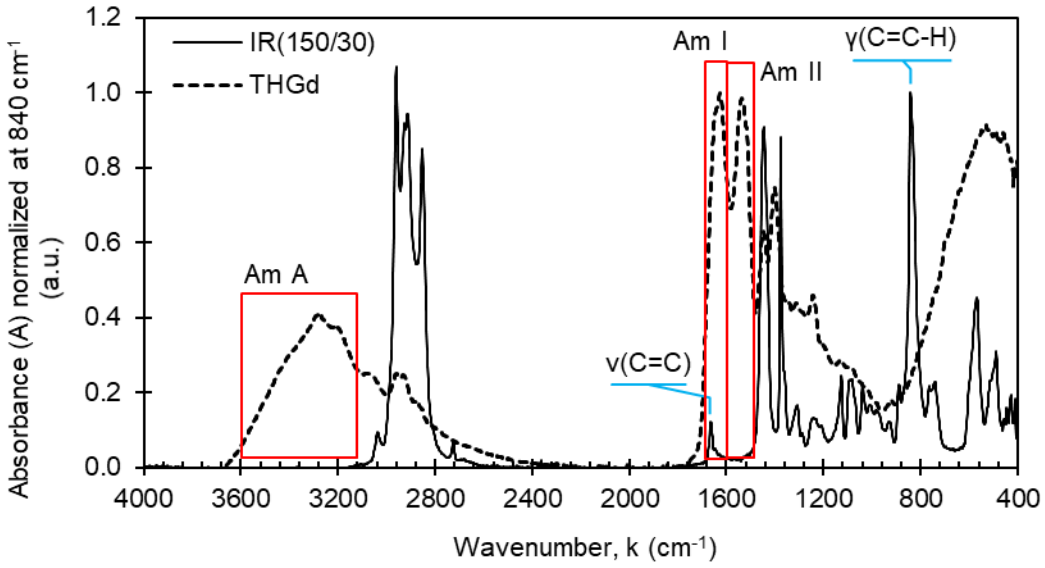


**Figure 8.** – FTIR spectra for neat THGd protein (dashed line) and an IR control compounded for 150 °C and 30 rpm (solid line). The major protein absorbances include the Amide A, I, and II modes (red insets). Spectra were normalized to the γ(C=C-H) absorbance in IR.

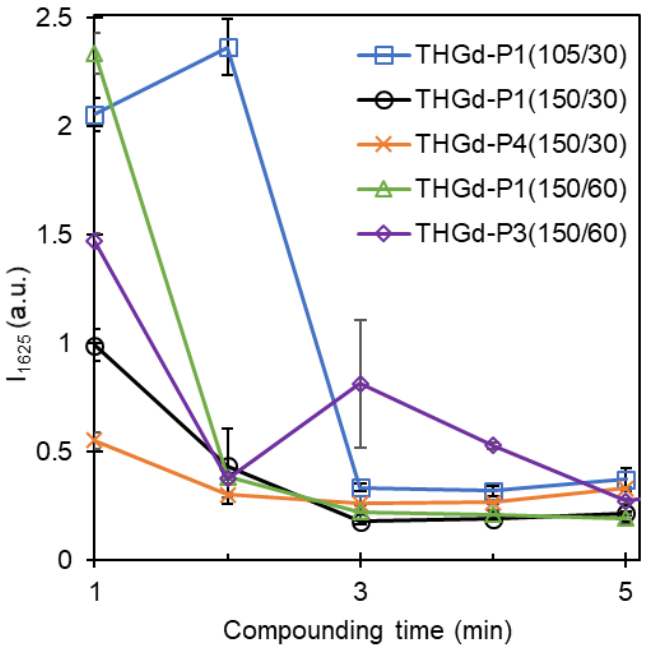


**Figure 9.** – Average normalized intensity at 1625 $cm^{-1}$ ($I_{1625}$ ± standard error) as a function of compounding time for compounds processed using different parameters. $I_{1625}$ was calculated from the spectra normalized to the γ(C=C) absorbance at 840 $cm^{-1}$.

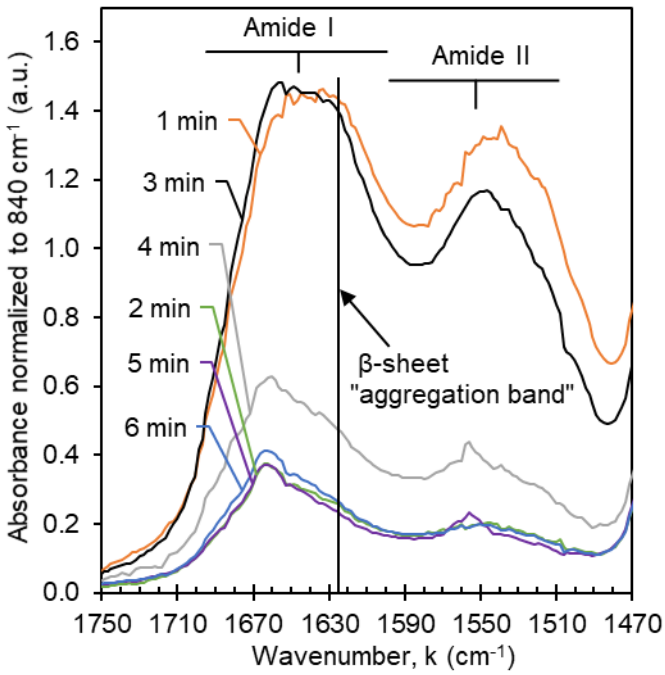


**Figure 10.** – FTIR spectra, normalized to the γ(C=C) absorbance at 840 $cm^{-1}$ in IR, showing the Amide I and II modes for THGd-P3(150/60) as a function of compounding time.

# CHAPTER V. HYDROLYZED WHEAT PROTEIN AS A SELF-ASSEMBLED REINFORCING FILLER IN SYNTHETIC ISOPRENE RUBBER VULCANIZATES

DeButts, B. L., Thompson, R.V., & Barone, J. R. (2019). Hydrolyzed wheat protein as a self-assembled reinforcing filler in synthetic isoprene rubber vulcanizates. *Ind. Crops Prod.*, (in review).

Chapter V has been submitted to and is under review by the following peer-reviewed journal: *Industrial Crops and Products* published by Elsevier B.V. The chapter is formatted according to the journal guidelines set forth by the publishers.

# Hydrolyzed wheat protein as a self-assembled reinforcing filler in synthetic isoprene rubber vulcanizates

Barbara L. DeButts[a,b], Renee V. Thompson[c], Justin R. Barone[a-e*]

[a]*Macromolecular Science and Engineering,* [b]*Macromolecules Innovation Institute, Virginia Tech, Blacksburg, VA 24061*

[c]*NSF RET: Biomechanics from molecular to organismal scales*

[d]*Biological Systems Engineering, Virginia Tech, 301D Human and Agricultural Biosciences Building 1, 1230 Washington St. SW, Blacksburg, VA 24061*

[e]*Center for Soft Matter and Biological Physics, Department of Physics, 850 W. Campus Dr., Virginia Tech, Blacksburg, VA 24061*

*Corresponding author.

*E-mail address:* jbarone@vt.edu (J.R. Barone).

ARTICLE INFO

*Keywords:* Polymer composite; β-sheets; protein self-assembly; curing kinetics; mechanical properties; molecular structure

ABSTRACT

Trypsin hydrolyzed gliadin (THGd) from wheat protein is utilized as a reinforcing filler in synthetic rubber. THGd self-assembles into a reinforcing filler phase during sulfur vulcanization of synthetic cis-1,4-polyisoprene rubber (IR), as observed by an increase in the β-sheet aggregation absorbance in Fourier transform infrared spectroscopy (FTIR). The curing kinetics are studied using differential scanning calorimetry (DSC). Compared to the IR Control, the THGd-filled compounds have slower curing kinetics, owing to a shorter scorch time, and more incomplete cure. Young's modulus (E) increases with protein concentration, curing time, and silane coupling agent concentration. Moduli comparable to or greater than the IR Control are achieved at all tested protein loadings of 4-16 parts per hundred rubber (phr). Hysteresis decreases with curing time showing the formation of a more elastic network and increases with filler and silane concentration showing energy dissipation through filler re-arrangement and rubber molecule-filler particle detachment, respectively. Swelling generally decreases with increasing filler content. The results suggest that quantities of THGd greater than 4 phr reinforce the rubber phase through continued aggregation into protein β-sheet nanostructures.

## 1. Introduction

Fillers are added to rubber compounds to reduce cost and/or modify properties. The most common cost reducing, i.e., inert, fillers are kaolin clay and calcium carbonate. The most common property enhancing fillers are carbon black and precipitated silica, which primarily offer reinforcement (Thomas and Stephen, 2010). However, carbon black is derived from petroleum, while silica requires extensive processing to effectively disperse in rubber. Biofillers derived from wood, cellulose, chitin, husk, lignin, and agricultural waste have also been incorporated into rubber matrices (Bhattacharya et al., 2011; Bhattacharyya et al., 2012; Bras et al., 2010; Da Costa et al.,

2003a; Gopalan Nair and Dufresne, 2003a, b; Jong, 2005; Masłowski et al., 2017; Zhou et al., 2015). Biofillers are relatively inexpensive, low density, biodegradable, and sustainable (Rwawiire et al., 2015). The automotive industry must meet increasingly stringent standards for fuel efficiency, $CO_2$ emissions, and end-of-vehicle-life reusability/recyclability (Despeisse et al., 2015; Kc et al., 2016; Park and Park, 2018; Yang et al., 2017). Since 70% of worldwide rubber production is used for tire applications, rubber biofillers and "green tires" represent an important part of the sustainability effort (Soratana et al., 2017; Warren-Thomas et al., 2015).

Rubber fillers are typically added during the rubber compounding stage, where the processability of the filled rubber compound must be optimized (Erman et al., 2013). The filler properties, such as concentration, surface chemistry, dispersion, and matrix compatibility have been shown to affect the cure kinetics and the final properties of the rubber vulcanizate (Chough and Chang, 1996). Some natural reinforcing fillers have been found to have a beneficial effect on rubber curing kinetics (Da Costa et al., 2003a; Da Costa et al., 2003b). For example, a filler derived from eggshell particles was effective at improving the mechanical properties and increasing the cure rate and crosslink density of natural and guayule rubber (Barrera and Cornish, 2016, 2017). Hydrolyzed wheat gluten protein has been successfully used as a reinforcing filler for various polymer matrices (Claunch et al., 2015; DeButts et al., 2018a; DeButts et al., 2018b). It is hypothesized that trypsin hydrolyzed gliadin (THGd) from wheat gluten protein could reinforce rubber through a known β-sheet self-assembly mechanism (Ridgley et al., 2012, 2013; Ridgley et al., 2014) and that the curing process would facilitate self-assembly.

In 2016, the worldwide crop production of wheat was 750 Mt, which was surpassed only by maize and rice (www.fao.org, 2016; Asseng et al., 2017). The protein content (10-13%) of wheat, i.e., wheat gluten, is high compared to maize and rice (2-8% protein), so a significant amount of

protein can be obtained from wheat production even if less is grown (Weegels et al., 1992). The gliadin fraction of wheat gluten is approximately 40% of the total wheat grain protein (Daniel and Triboi, 2000). Thus, the total gliadin protein available globally in 2016 was 30-34 Mt, which exceeded the 13.2 Mt of carbon black consumed in 2015 (Van Genderen et al., 2016). A comparative cost analysis for wheat and carbon black reveals that there is an advantage to using a wheat-based filler. As of March 2018, the World Bank listed the cost of wheat grain as $190.6 per metric ton (www.worldbank.org, 2018). Current bulk pricing of carbon black available online is in the range of $800-1200/ton. Thus, there are environmental and economic advantages to replacing the carbon black in cured rubber.

In this work, THGd protein is used as a filler in a typical rubber compound. The effects of protein concentration, curing time, and protein-rubber compatibility are assessed using differential scanning calorimetry (DSC), Fourier transform infrared spectroscopy (FTIR), tensile testing, and swelling experiments. The vulcanization kinetics, mechanical and structural properties, and crosslink density of THGd-IR vulcanizates demonstrate that THGd can successfully provide IR reinforcement at concentrations > 4 phr THGd.

## 2. Experimental

### *2.1. Materials*

Gliadin from wheat (Gd), trypsin enzyme (Type I from bovine pancreas), slab synthetic polyisoprene rubber (IR, 97 % cis-1,4-polyisoprene), and (3-mercaptopropyl)triethoxysilane (SIL) were purchased from Sigma-Aldrich (St. Louis, MO). Elemental sulfur (S) and N-tert-butyl-benzothiazole sulfonamide (TBBS) were graciously provided by Hankook Tire.

### *2.2. Methods*

#### *2.2.1. Preparation of trypsin hydrolyzed gliadin (THGd) protein-IR composites.*

THGd was hydrolyzed according to a procedure used previously,(Ridgley et al., 2013) in which Gd (20 g) was dispersed in water (800 mL), trypsin enzyme (0.3 g) was added, and the dispersion was maintained at 37 °C and pH 8 using NaOH (1M or 4M) for 72 h. The hydrolysate was characterized and contained mostly low-molecular weight peptides (≤ 10 kDa) (Athamneh and Barone, 2009; Tuck et al., 2014). The hydrolysate was dried to a thin, solid film containing 97 % solids under a fume hood at room temperature (RT) and manually broken into small flakes approximately 2-5 mm in diameter. The protein hydrolysate, curatives, and IR were compounded in 45-50 g batches on a Prep-Center with an internal mixing head (Brabender, Hackensack, NJ) according to the formulations in Table I. Single-stage compounding was performed at 60 rpm for 7 min as specified in ASTM D3182 and outlined in Table II, with an initial temperature of 50 °C. The final dump temperature was 88 ± 5 °C. Samples were manually mixed for an additional 2 min using a rolling pin.

*2.2.2. Preparation of vulcanized sheets.*

Compounds were compression molded at 145 °C on an Auto Series hydraulic laboratory press (Carver, Wabash, IN) at 2.5 MPa pressure for 50 or 80 min. The ASTM D3182 recommended cure time (50 min) was extended to 80 min for some of the protein-containing samples. Steel shims (1 mm thickness) were used to achieve a uniform film thickness.

*2.2.3. Differential scanning calorimetry (DSC).*

Unvulcanized samples (17.0-18.0 mg, TZero pans) were heated at 150, 160, 170, and 180 °C in triplicate under nitrogen until a post-cure stable baseline was achieved (Q2000 DSC, TA Instruments, Waltham, MA). Calculations were performed using TA Instruments Universal Analysis software.

*2.2.4. Tensile testing.*

ASTM D412 Die D tensile specimens were uniaxially extended at a rate of 500 mm/min on a Texture Analyzer TA.HD*Plus* (Texture Technologies Corp., Hamilton, MA) equipped with a 100-kg load cell and self-tightening crosshatched grips. Young's moduli (E) were calculated from a sample size of 3 by linear regression analysis of the low-strain Hookean region of the stress-strain plots in Excel.

*2.2.5. Tensile hysteresis.*

ASTM D412 Die D specimens with a reduced gauge length of 16 mm were uniaxially deformed to 250 % and 1000 % elongation for 12 cycles at 500 mm/min. Tests were performed in triplicate. Hysteresis was calculated (Equation 1), where $A_{loading}$ and $A_{unloading}$ were the area under the loading and unloading curves, respectively.

$$\%Hysteresis = \left(\frac{A_{loading} - A_{unloading}}{A_{loading}}\right) * 100 \quad (1)$$

*2.2.6. Swelling tests.*

The swelling experiment was based on ASTM D6814 (www.astm.org, 2013). A 30-mm diameter sample was cut from each vulcanized sheet and its weight ($w_i$) and dimensions were recorded. The sample was submerged at 23 °C for 72 h in 100 mL toluene, with the solvent replaced daily. Every 24 h, the sample was removed, gently patted with a paper towel to remove extra solvent adhering to the surface, and its mass and dimensions were recorded. Vulcanizate swelling of several hundred percent was observed in the first 24 h. An incremental increase in swelling of a few percent every 24 h was observed after the initial 24 h. Valentin et al. (Valentín et al., 2008) studied this behavior and found that equilibrium swelling occurred at 20-30 h, after which the diffusive swelling process was replaced by a slow swelling due to network degradation. It was also found that photo-oxidative degradation of the sulfur bridges continued until complete

dissolution of the network at ~1 month. For our purposes, equilibrium swelling was achieved at t=24 h. The initial weight and the weight of the swollen sample at 24 h ($w_s$) were used to find the volume fraction of rubber in the swollen network ($\phi_r$)

$$\phi_r = \frac{\frac{w_i}{\rho_r}}{\frac{w_i}{\rho_r} + \frac{w_s - w_i}{\rho_t}} \quad (2)$$

where $\rho_r$ is the density of cis-1,4-polyisoprene (0.91 g/cm$^3$) and $\rho_t$ is the density of toluene (0.87 g/cm$^3$). The equilibrium volume swelling ratio, $Q_s$, was defined as (Rubinstein and Colby, 2003):

$$Q_s = \frac{1}{\phi_r} \quad (3)$$

The amount of swelling was affected by the crosslink density of the material and the presence of fillers in the vulcanizate (Bilgili et al., 2001; Choi, 2000; Messori et al., 2009; Valentín et al., 2008). For these samples, the filler was THGd protein which was insoluble in toluene.

*2.2.7. Fourier Transform Infrared (FTIR) Spectroscopy.*

Attenuated total reflectance (ATR) FTIR spectra of the pre-cure compounds and post-cure vulcanizates were collected in triplicate (Nicolet 6700 FTIR spectrometer with a Smart Orbit ATR diamond crystal, Thermo Fisher Scientific Inc., Madison, WI) at ambient conditions. Spectra were averaged from 128 scans at 4 cm$^{-1}$ resolution from 4000-400 cm$^{-1}$, then baseline corrected, normalized, and analyzed using OMNIC v8.1 software.

## 3. Results and discussion

*3.1. Curing kinetics*

A general kinetic model (MacCallum and Tanner, 1970) for the degree of cure as a function of time, dα/dt, is defined below:

$$\frac{d\alpha}{dt} = K(T)f(\alpha) \tag{4}$$

$$K(T) = K_0 \mathrm{e}^{-E_\alpha/RT} \tag{5}$$

The temperature dependent kinetic function, K(T), (Equation 5) follows an Arrhenius relationship, where the pre-exponential factor, $K_0$, and activation energy, $E_\alpha$, required to achieve degree of cure, α, are material dependent parameters, R is the universal gas constant, and T is absolute temperature. Many different variations of the curing function, f(α), have been used to describe sulfur curing (Ding and Leonov, 1996; López-Manchado et al., 2003; Nie et al., 2010; Wan and Isayev, 1996). For this work, the form of the kinetic curing function, f(α), is inconsequential because f(α) is temperature-independent.

The cure rate, dα/dt, is obtained experimentally by DSC, which measures heat flow (Q) with time. The degree of cure, α, is described by Equation 6, where $Q_t$ is the heat flow at time, t, and $Q_\infty$ is the heat flow at the end of the reaction (Choi, 2000; Torre et al., 2013).

$$\alpha(t) = \frac{\int_0^t Q_t \, dt}{\int_0^\infty Q_\infty \, dt} \tag{6}$$

Since the data sets are discrete a numerical approximation method is used to find α(t). The trapezoid rule is used to approximate an integral, where the width is the time step between data points, Δt, and the height is the midpoint of the heat flow difference (Equation 7). The summation bounds are the time at which curing starts ($t_i$) and ends ($t_f$):

$$\alpha(t) \approx \frac{\sum_{t=t_i}^{t} \left( \frac{|Q(t+\Delta t) - Q(t)|}{2} \right) (\Delta t)}{\sum_{t=t_i}^{t_f} \left( \frac{|Q(t+\Delta t) - Q(t)|}{2} \right) (\Delta t)} \quad (7)$$

Since the data is collected over many time steps ($\Delta t > 10{,}000$), this produces a good approximation. The summation bounds are chosen to isolate the curing stage from the pre-cure and post-cure behavior. Using the method proposed by Arrillaga et al. (Arrillaga et al., 2007), a horizontal baseline originating from the heat flow plateau after curing is drawn. The summation bounds are located at the intersection of the baseline with the experimental data (Supporting Information, Figure S1). The total area between the cure curve and the baseline, i.e., the denominator of Equation 7, is used to normalize the data, with the assumption that each vulcanizate cures completely ($\alpha=1$) according to its formulation at all curing temperatures (Ishida and Rodriguez, 1995). Additionally, it is assumed that the reaction exotherm represents the formation of crosslinks and any competing side reactions are negligible compared to the curing reaction (López-Manchado et al., 2003).

Figure 1a shows typical reaction exotherms for the IR Control and THGd-IR compounds isothermally held at 150 °C. The compounds exhibit an induction period, which is typical of delayed-action accelerators such as TBBS (Ghosh et al., 2003). The induction period, also called the scorch time, is the pre-cure elapsed time during which the compound can be processed (Engels et al., 2011). An increase in heat flow (Q) is observed at 15 min in the IR Control and 5-10 min in the THGd-IR compounds, which indicates the onset of curing (Figures 1a and S1). THGd suppresses the induction period observed in the control even at concentrations as low as 4 phr THGd (Figure 1a). A shorter induction time can be problematic in tire processing, where the material must fill a mold before curing (Engels et al., 2011). Other fillers have been shown to

decrease the induction period with varying and sometimes conflicting effects on the overall kinetics (Wu et al., 2013). The THGd-IR compounds exhibit single exothermic peaks, which is typical of sulfur-cured rubber. The exotherms for THGd-4 and THGd-8 are skewed, where $d\alpha/dt$ initially increases quickly, reaches a maximum, then trails off for the remainder of the reaction (Figure 1a). The skewed isotherms indicate faster reaction kinetics during early curing and suggest that an initial reaction occurs between the protein and curatives and the formation of an initial product aids the primary curing reaction (Michaelsen et al., 1997). As the protein and/or silane coupling agent concentration increases, the induction time increases and heat of reaction ($\Delta H$) decreases, indicating slower curing kinetics and less crosslink formation. These results suggest the excess fillers (e.g., THGd protein and silane coupling agent) hinder crosslink formation.

By integrating the reaction exotherms in Figure 1a with respect to time (Equation 7), the degree of cure, $\alpha(t)$, is calculated (Figure 1b). The shape of the cure curves is similar for the THGd-IR compounds but differ from the steeper curve observed in the IR Control. Earlier reactivity, which is assumed to be crosslink formation (López-Manchado et al., 2003), is observed in the THGd-containing samples. At the 50-minute ASTM D3182 recommended curing time, the compounds are 60-80% cured. The incomplete curing is attributed to the elimination of the ZnO and stearic acid activator package from the cure recipe. On average, an additional 30 minutes of curing, i.e., 80 minutes total, is required to reach a desired 90% cure in the compounds, where the time to 90% cure ($t_{90}$) increases as protein or silane concentration increases.

The average apparent activation energy, $\overline{E}_\alpha$ is calculated for three degrees of cure: $\alpha$=25%, 55%, and 95%. To calculate $E_\alpha$, the temperature-dependent kinetic function (Equation 5) is substituted into the general kinetic curing expression (Equation 4) and integrated to produce an equation for a line. The time to reach a degree of cure, $t_\alpha$, is used to calculate $E_\alpha$ (Ishida and

Rodriguez, 1995). On a plot of ln $t_\alpha$ versus 1/RT, $E_\alpha$ is the slope of the line (Equation 8) (Leroy et al., 2013). The model is a good fit for the data, with $R^2 \geq 0.97$ for all $E_\alpha$ calculations.

$$\ln t_\alpha = \frac{E_\alpha}{RT} - \ln\left[\frac{\int_0^{\alpha_j} d\alpha/f(\alpha)}{K_0}\right] \tag{8}$$

This method assumes a constant activation energy for the curing reaction and so an average $E_\alpha$ ($\overline{E}_\alpha$) is calculated. Due to the assumptions used in calculating $\overline{E}_\alpha$, it is used to assess the relative trends in reaction kinetics rather than taken as an absolute quantitative value. The time to reach a degree of cure, $t_\alpha$, at a constant temperature, is defined for $\alpha$=5% ($t_{05}$) and $\alpha$=90% ($t_{90}$). The elapsed curing time ($\Delta t = t_{90} - t_{05}$) is calculated and used to find the Cure Rate Index (CRI = $100/\Delta t$). The average values ± standard error for $t_{05}$, $t_{90}$, $\Delta t$, CRI, $\Delta H$, and $\overline{E}_\alpha$ are given in Table III. The THGd-containing compounds generally exhibit slower curing kinetics, i.e., lower CRI values, and higher $\overline{E}_\alpha$, than the IR Control. The kinetics and activation energies are most favorable at 8 phr THGd. As the concentration of THGd increases, $\Delta H$ generally decreases, implying that fewer crosslinking reactions occur and that lower protein loadings exhibit greater network formation than higher protein loadings. The increase in $\overline{E}_\alpha$ and decrease in $\Delta H$ at ≥12 phr THGd demonstrate that the additional protein hinders crosslinking.

It is hypothesized that the partially hydrophilic THGd protein filler and hydrophobic rubber matrix may have poor compatibility. Poor filler-matrix compatibility can lead to phase separation in polymer composites. Since the dispersion of protein throughout the rubber matrix is important to the vulcanizate mechanical properties, a silane coupling agent is added in quantities of 4 and 8 phr to THGd-8, called THGd-8/SIL-4 and THGd-8/SIL-8, to improve protein-rubber compatibility. Triethoxy-based silane coupling agents have been used in natural fiber polymer

nanocomposites and coupling agents with mercapto organofunctionality have been used to preferentially target rubber (Xie et al., 2010). In Table III, $t_{05}$, $t_{90}$, and $\Delta t$ increase as a function of silane coupling agent, and $\Delta H$ decreases. This suggests that the coupling agent impedes crosslinking and compatibilizing the protein and rubber phases is found to negatively impact the reaction kinetics.

*3.2. Mechanical properties*

The Young's modulus (E) as a function of the total filler loading is given in Figure 2. E increases as a function of protein concentration (Figure 2). At 8 phr THGd loading, an increase in modulus is observed with the addition of silane coupling agent, where E for THGd-8/SIL-4 (0.65 ±0.01 MPa) is 10% higher than THGd-8, and E for THGd-8/SIL-8 (0.71±0.02 MPa) is 20% higher than THGd-8. Given the DSC curing kinetics (Figure 1), THGd-8 is subjected to two different curing times: (1) a 50-min cure to match the ASTM D3182 cure time, and, (2) an 80-min cure to complete curing ($\alpha \cong 90\%$). It is hypothesized that a longer curing time should promote network formation in the THGd-activated vulcanizates, thereby improving crosslink density and modulus. The modulus for THGd-8 cured for 80 minutes (E=0.60±0.01 MPa; +10% over the IR Control, i.e., 0 phr filler) is only slightly greater than THGd-8 cured for 50 minutes (E=0.56±0.01 MPa; no change from IR Control). THGd-12 (E=0.91±0.04 MPa; +65% over the IR Control) and THGd-16 (E=1.37±0.05 MPa; +150% over the IR Control) exceed the modulus of the IR Control (E=0.55±0.01 MPa). Since these samples exhibit the lowest $\Delta H$, it is concluded that the modulus increase is a result of protein reinforcement rather than a greater crosslink density.

*3.3. Hysteresis*

Hysteresis describes the energy dissipated of cured rubber upon repeated extension/retraction. In filled rubbers, hysteresis is generally higher because of: (1) the relatively

large amount of stress required to induce deformation and, (2) the energy dissipated during destruction and reformation of the filler network (Bergstrom and Boyce, 1999; Wang, 1999). The reinforcing effect of any rubber filler is most effective at small strains where the filler network is intact. In a hysteresis experiment, the matrix stiffening caused by a filler is largely destroyed during the first extension and the behavior of repeated extension cycles is very different than the first cycle. After a few extension/retraction cycles, known as the conditioning period, the hysteresis reaches a relatively constant value (Lion, 1996). This behavior is known as the Mullins effect (Chagnon et al., 2004; Mullins, 1948). For the vulcanizates, hysteresis is larger as THGd-loading is increased, akin to other rubber fillers (Boonstra, 1979) and corroborating the protein aggregation and reinforcing effect (Figure 3). Hysteresis is lower at higher elongation for the compounds with protein aggregate-reinforcement. This suggests that the protein filler network stores elastic energy at higher deformation (Loukil et al., 2018). Hysteresis increases as a function of silane content in the THGd-8 vulcanizates because there are more protein filler-rubber interactions to break at a given strain. At low elongation ($\varepsilon$=250%), the IR Control has the lowest hysteresis or highest elastic recovery (Figure 3a). At high elongation ($\varepsilon$=1000%), THGd-4 has the lowest hysteresis and is the only THGd-filled vulcanizate to decrease hysteresis over the IR Control, although THGd-8 and THGd-8/SIL-4 approach the IR Control hysteresis (Figure 3b). Hysteresis decreases as a function of increasing curing time in THGd-8 vulcanizates at $\varepsilon$=250% because of the more extensively formed crosslinked network. A rubber compound that relies more on its crosslinked network for stiffness than reinforcing fillers has lower hysteresis. As the elongation increases to 1000%, the cure time has no effect on hysteresis. This is interpreted as destruction of crosslinks at high elongation, which results from limited network extensibility in highly crosslinked samples (Mullins, 1948).

*3.4. Swelling*

In principle, the vulcanizate mechanical properties are dependent on the crosslink density, [X], which is related to formulation and degree of cure, $\alpha$ (Krejsa and Koenig, 1993). A common method to measure crosslink density is by an equilibrium swelling experiment, where a vulcanizate will swell in a good solvent and an unvulcanized compound will dissolve. The equilibrium volume swelling ratio, $Q_s$, is related to the crosslink density, [X], as described by the Flory-Rehner equation (www.astm.org, 2013; Bilgili et al., 2001; Flory, 1953; Nie et al., 2010; Valentín et al., 2008). Crosslink density, [X], is directly related to the shear modulus, G=[X]RT, where R is the ideal gas constant and T is absolute temperature. The rubber shear modulus, G, can be found from the tensile modulus, E, using E=3G (Shaw and MacKnight, 2005). Therefore, experimental values of E and $Q_s$ on the IR Control are used in the Flory-Rehner equation to independently determine the Flory-Huggins polymer-solvent interaction parameter, $\chi$. $\chi$ is found to be 0.395±0.005, which is in close agreement to the 0.391 literature value for toluene-IR (www.astm.org, 2013). So, this method works well for unfilled rubber.

Swelling is observed for all formulations, which is indicative of crosslinking. This demonstrates that sulfur crosslinking of IR in a ZnO-free system at a standard curing temperature of 145 °C has occurred. The determination of crosslink density from swelling measurements can be complicated by the presence of filler, resulting in a higher apparent crosslink density (Boonstra and Taylor, 1965; Kraus, 1963; Mori and Koenig, 1998; Porter, 1967). The filler restricts swelling, increasing modulus and artificially increasing crosslink density. The equilibrium swelling ratio ($Q_s$, Equation 3) decreases as THGd content increases up to 12 phr THGd and as silane content increases at THGd phr = 8 (Figure 4). The DSC isothermal curing experiments (Section 3.1) show that $\Delta H$ decreases, i.e., fewer crosslinks are formed, with increasing THGd content (Table III).

The decrease in $Q_s$ originates from the filler opposing swelling rather than from higher crosslink density. The silane results are evidence of the filler effect: stronger filler-matrix interactions resist swelling even in the lowest crosslinked samples (Table III). As the curing time is increased from 50 to 80 min in THGd-8, $Q_s$ decreases, which can be interpreted as a greater degree of cure after 80 min corroborating the DSC isothermal curing experiments (Section 3.1).

*3.5. Structural analysis*

The IR Control spectra are dominated by the various C-H vibrational modes: symmetric methylene stretching ($\nu_s(CH_2)$ at ~2850 $cm^{-1}$), asymmetric methylene stretching ($\nu_{as}(CH_2)$ at ~2915 $cm^{-1}$), symmetric methylene deformation ($\delta_s(CH_2)$ at ~1445 $cm^{-1}$), symmetric methyl stretching ($\nu_s(CH_3)_{as}$ at ~2960 $cm^{-1}$), symmetric methyl deformation ($\delta_s(CH_3)$ at ~1375 $cm^{-1}$), and wagging of the cis-1,4 addition ($\gamma$(C=C-H) at ~835 $cm^{-1}$) (Figure 5) (Agostini et al., 2008; Binder, 1963; Craciun et al., 2016; Gunasekaran et al., 2007; Rolere et al., 2015). The IR Control spectrum is normalized to the $\nu_s(CH_3)$ deformation at 1375 $cm^{-1}$. The major absorbances in the IR Control are separate from those in fully-aggregated THGd and it is easy to isolate the protein contributions from the rubber phase in the composites (Figure 5). Fully-aggregated THGd has the following dominant absorbances: amine/amide stretching ($\nu$(NH) centered at 3283 $cm^{-1}$), Amide I ($\nu$(C=O) from 1600-1700 $cm^{-1}$), and Amide II ($\delta$(N-H) and $\nu$(C-N) from 1480-1575 $cm^{-1}$) (Jackson and Mantsch, 1995; Miyazawa et al., 1956; Rolere et al., 2016). The absorbance maximum of the Amide I region occurs at 1625 $cm^{-1}$, which is indicative of strong β-sheet nanostructure formation in the fully-aggregated THGd (Ridgley et al., 2013). A small contribution at ~1660 $cm^{-1}$ from C=C stretching, $\nu$(C=C), in the IR Control is superimposed on the high wavenumber region of the Amide I absorbance but it does not affect the quantitative interpretation of β-sheets at the lower

1625 $cm^{-1}$ absorbance (Binder, 1963; Le Xuan and Decker, 1993; Salomon and Van Der Schee, 1954).

THGd-IR spectra are normalized to the $\nu(CH_3)$ 1375 $cm^{-1}$ absorbance in IR to quantify changes in the THGd structure relative to the IR content. At protein loadings above 4 phr THGd, an increase in the ν(N-H) and Amide I absorbance is observed with curing. This shows that a minimum concentration of protein is necessary for hydrogen bonding and β-sheet aggregation to occur during curing. The curing process is favorable to the formation of a β-sheet reinforcing phase and increased filler-filler interactions, i.e., hydrogen bonding. Figure 6 shows the spectra of uncured and cured THGd-12, which exemplify the change in the Amide I absorbance with curing for the filled vulcanizates with more than 4 phr THGd. An average 1625 $cm^{-1}$ β-sheet absorbance is calculated for the uncured and cured THGd-IR composites (Figure 7). Spectra are collected from different areas of an uncured compound or cured vulcanizate to assess the uniformity, i.e., dispersion, of the THGd phase. The variation in the normalized Amide I absorbance in Figure 6 shows the variation in protein aggregation across the sample surface. For the uncured compounds, the repeat spectra are largely superimposable (represented as a small standard error in Figure 7). This indicates that the compounding process results in a well-distributed protein phase with a similar degree of aggregation.

The β-sheet content for THGd-4 is unchanged with curing, suggesting that 4 phr protein is too low a concentration to foster aggregation. As protein concentration increases, more β-sheets and aggregation are observed and the Amide I absorbance in the cured vulcanizates is larger than the uncured compounds. In THGd-8, as curing time increases from 50 to 80 minutes, the protein absorbance does not change significantly, suggesting that protein aggregation occurs within 50 minutes. The cured vulcanizates have variation between repeat spectra (shown as an enlargement

of the standard error in Figure 7), and some areas of the vulcanizates exhibit greater protein aggregation than others (again see Figure 6). β-sheets are known to have high rigidity and stability (Keten et al., 2010) and β-sheet containing structures have been shown to have a reinforcing effect on polymer matrices (Byrne et al., 2011; DeButts et al., 2018a; Knowles and Buehler, 2011; Oppenheim et al., 2010; Rao et al., 2012). The FTIR results show that protein aggregation into rigid β-sheet structures occurs above 4 phr THGd and that reinforcement, as measured by an increase in E (Figure 2) and a decrease in $Q_s$ (Figure 4), is observed. Long molding times, as well as high-temperature and pressure conditions, such as the curing conditions used, have been shown to facilitate wheat protein aggregation into β-sheets (DeButts et al., 2018b; Kieffer et al., 2007). The decrease in ΔH and increase in $\overline{E}_\alpha$ for THGd-12 and THGd-16 (Table III), but higher modulus (Figure 2), suggest that the additional protein aggregates may impede the diffusion of curatives (i.e., TBBS and/or S) through the rubber phase. The diffusion of curatives through the rubber matrix is necessary to form active sulphurating species, which further diffuse to form crosslinks (Wu et al., 2013). THGd-16 has similar protein aggregation to THGd-12, (Figure 7) but a higher modulus (Figure 2). Both are similarly crosslinked (Table III) but THGd-16 has the highest swelling (Figure 4). Modulus is measured in the low applied strain region where the network is not highly extended. Swelling greatly extends the network to high strains. It is possible that the excess unassembled protein cannot reinforce at high strains and contributes to the high hysteresis.

In the uncured THGd-8/SIL-4 and THGd-8/SIL-8, a reduction in the Amide I absorbance is observed with increasing silane concentration, indicating less protein aggregation and more protein dispersion, consistent with a compatibilized protein-rubber system (Figure 7). The poor curing kinetics in these samples (Table III) shows that silane interferes with crosslinking by itself and/or by dispersing more unaggregated protein to interfere with curing. The post-cure β-sheet content

is similar in THGd-8, THGd-8/SIL-4 and THGd-8/SIL-8, showing that curing enhances protein aggregation even when the molecules are more dispersed in the silane containing compounds. The curing time and temperature are enough to allow protein molecules to diffuse to one another and aggregate even when highly dispersed in the silane containing compounds.

## 4. Conclusions

This study sought to improve the sustainability and ecotoxicity of cured rubber by introducing trypsin hydrolyzed gliadin from wheat protein (THGd) as a reinforcing filler. Isothermal differential scanning calorimetry (DSC) is used to assess the curing kinetics of the trypsin hydrolyzed gliadin-synthetic cis-1,4-polyisoprene rubber (THGd-IR) compounds. In the THGd-IR compounds, a reduced induction time and Cure Rate Index (CRI) is observed, indicating slower overall reaction kinetics. The composite kinetics are most favorable at 8 parts per hundred rubber (phr) THGd, which exhibits the lowest average activation energy ($\overline{E}_\alpha$) and reaches 90% cure the fastest. The increase in $\overline{E}_\alpha$ and decrease in heat of reaction ($\Delta H$) at high protein loadings of 12 and 16 phr THGd suggest that the additional protein hinders crosslinking. A (3-mercaptopropyl)triethoxysilane coupling agent (SIL) is added and negatively impacts the reaction kinetics because $\overline{E}_\alpha$ increases and $\Delta H$ decreases as a function of silane content.

Young's modulus (E) increases as a function of protein concentration, curing time, and silane concentration. THGd-4 matches the IR Control modulus, while THGd-16 exceeds it by 150%. The equilibrium volume swelling ratio ($Q_s$) generally decreases with increasing THGd content showing the reinforcing effect from THGd. Using Fourier transform infrared (FTIR) spectroscopy protein aggregation into nanostructured β-sheets is observed in the vulcanizates at THGd loadings >4 phr. The combined results from tensile, swelling, and FTIR experiments suggests that if

sufficient protein is present (> 4 phr), THGd can aggregate into a reinforcing filler phase during the curing process. Ultimately, this study demonstrates that an industrially viable reinforcing filler is possible using a wheat protein agricultural waste product.

## Acknowledgments

This work was supported by the USDA National Institute of Food and Agriculture, AFRI project [grant number USDA-2016-67021-25006]. Renee Thompson performed parts of this research while participating in the NSF-Research Experience for Teachers (RET) program "Biomechanics from molecular to organismal scales" [grant number NSF-EEC-RET-1301037].

## References

2013. ASTM D6814-02(2013) Standard Test Method for Determination of Percent Devulcanization of Crumb Rubber Based on Crosslink Density, ASTM D6814-02(2013). ASTM International, West Conshohocken, PA.

2016. Food and Agriculture Organization of the United Nations, in: database, F.s. (Ed.). FAOSTAT Database, Rome, Italy.

2018. World Bank Commodities Price Data (The Pink Sheet). World Bank.

Agostini, D., Constantino, C., Job, A.E., 2008. Thermal degradation of both latex and latex cast films forming membranes. J. Therm. Anal. Calorim. 91, 703-707.

Arrillaga, A., Zaldua, A.M., Atxurra, R.M., Farid, A.S., 2007. Techniques used for determining cure kinetics of rubber compounds. Eur. Polym. J. 43, 4783-4799.

Asseng, S., Cammarano, D., Basso, B., Chung, U., Alderman, P.D., Sonder, K., Reynolds, M., Lobell, D.B., 2017. Hot spots of wheat yield decline with rising temperatures. Global Change Biol. 23, 2464-2472.

Athamneh, A.I., Barone, J.R., 2009. Enzyme-mediated self-assembly of highly ordered structures from disordered proteins. Smart Mater. Struct. 18, 104024.

Barrera, C.S., Cornish, K., 2016. High performance waste-derived filler/carbon black reinforced guayule natural rubber composites. Ind. Crops Prod. 86, 132-142.

Barrera, C.S., Cornish, K., 2017. Processing and mechanical properties of natural rubber/waste-derived nano filler composites compared to macro and micro filler composites. Ind. Crops Prod. 107, 217-231.

Bergstrom, J.S., Boyce, M.C., 1999. Mechanical behavior of particle filled elastomers. Rubber Chem. Technol. 72, 633-656.

Bhattacharya, M., Biswas, S., Bhowmick, A.K., 2011. Permeation characteristics and modeling of barrier properties of multifunctional rubber nanocomposites. Polymer 52, 1562-1576.

Bhattacharyya, S.K., Parmar, B.S., Chakraborty, A., Dasgupta, S., Mukhopadhyay, R., Bandyopadhyay, A., 2012. Exploring Microcrystalline Cellulose (MCC) as a Green Multifunctional Additive (MFA) in a Typical Solution-Grade Styrene Butadiene Rubber (S-SBR)-Based Tread Compound. Ind. Eng. Chem. Res. 51, 10649-10658.

Bilgili, E., Arastoopour, H., Bernstein, B., 2001. Pulverization of rubber granulates using the solid state shear extrusion process. Powder Technol. 115, 277-289.

Binder, J.L., 1963. The infrared spectra and structures of polyisoprenes. J. Polym. Sci., Part A: Polym. Chem. 1, 37-46.

Boonstra, B., 1979. Role of particulate fillers in elastomer reinforcement: a review. Polymer 20, 691-704.

Boonstra, B.B., Taylor, G.L., 1965. Swelling of filled rubber vulcanizates. Rubber Chem. Technol. 38, 943-960.

Bras, J., Hassan, M.L., Bruzesse, C., Hassan, E.A., El-Wakil, N.A., Dufresne, A., 2010. Mechanical, barrier, and biodegradability properties of bagasse cellulose whiskers reinforced natural rubber nanocomposites. Ind. Crops Prod. 32, 627-633.

Byrne, N., Hameed, N., Werzer, O., Guo, Q., 2011. The preparation of novel nanofilled polymer composites using poly (l-lactic acid) and protein fibers. Eur. Polym. J. 47, 1279-1283.

Chagnon, G., Verron, E., Gornet, L., Marckmann, G., Charrier, P., 2004. On the relevance of Continuum Damage Mechanics as applied to the Mullins effect in elastomers. J. Mech. Phys. Solids 52, 1627-1650.

Choi, S.S., 2000. Influence of rubber composition on change of crosslink density of rubber vulcanizates with EV cure system by thermal aging. J. Appl. Polym. Sci. 75, 1378-1384.

Chough, S.H., Chang, D.H., 1996. Kinetics of sulfur vulcanization of NR, BR, SBR, and their blends using a rheometer and DSC. J. Appl. Polym. Sci. 61, 449-454.

Claunch, E.C., Ridgley, D.M., Barone, J.R., 2015. Completely self-assembled fiber composites. Composites Sci. Technol.

Craciun, G., Manaila, E., Stelescu, M.D., 2016. New Elastomeric Materials Based on Natural Rubber Obtained by Electron Beam Irradiation for Food and Pharmaceutical Use. Materials 9, 999.

Da Costa, H.M., Visconte, L.L.Y., Nunes, R.C.R., Furtado, C.R.G., 2003a. Rice-husk-ash-filled natural rubber. II. Partial replacement of commercial fillers and the effect on the vulcanization process. J. Appl. Polym. Sci. 87, 1405-1413.

Da Costa, H.M., Visconte, L.L.Y., Nunes, R.C.R., Furtado, C.R.G., 2003b. Rice husk ash filled natural rubber. III. Role of metal oxides in kinetics of sulfur vulcanization. J. Appl. Polym. Sci. 90, 1519-1531.

Daniel, C., Triboi, E., 2000. Effects of Temperature and Nitrogen Nutrition on the Grain Composition of Winter Wheat: Effects on Gliadin Content and Composition. J. Cereal Sci. 32, 45-56.

DeButts, B.L., Hanzly, L.E., Barone, J.R., 2018a. Protein-polyisoprene rubber composites. J. Appl. Polym. Sci. 135.

DeButts, B.L., Spivey, C.R., Barone, J.R., 2018b. Wheat Gluten Aggregates as a Reinforcement for Poly(vinyl alcohol) Films. ACS Sustain. Chem. Eng. 6, 2422-2430.

Despeisse, M., Kishita, Y., Nakano, M., Barwood, M., 2015. Towards a Circular Economy for End-of-Life Vehicles: A Comparative Study UK – Japan. Procedia CIRP 29, 668-673.

Ding, R., Leonov, A., 1996. A kinetic model for sulfur accelerated vulcanization of a natural rubber compound. J. Appl. Polym. Sci. 61, 455-463.

Engels, H.-W., Weidenhaupt, H.-J., Pieroth, M., Hofmann, W., Menting, K.-H., Mergenhagen, T., Schmoll, R., Uhrlandt, S., 2011. Rubber, 9. Chemicals and Additives, Ullmann's Encyclopedia of Industrial Chemistry. Wiley-VCH Verlag GmbH & Co. KGaA, Weinheim, pp. 1-66.
Erman, B., Mark, J.E., Roland, C.M., 2013. The Science and Technology of Rubber, 4 ed. Elsevier Academic Press, Boston.
Flory, P.J., 1953. Principles of Polymer Chemistry. Cornell University Press, Ithaca.
Ghosh, P., Katare, S., Patkar, P., Caruthers, J.M., Venkatasubramanian, V., Walker, K.A., 2003. Sulfur vulcanization of natural rubber for benzothiazole accelerated formulations: from reaction mechanisms to a rational kinetic model. Rubber Chem. Technol. 76, 592-693.
Gopalan Nair, K., Dufresne, A., 2003a. Crab shell chitin whisker reinforced natural rubber nanocomposites. 1. Processing and swelling behavior. Biomacromolecules 4, 657-665.
Gopalan Nair, K., Dufresne, A., 2003b. Crab shell chitin whisker reinforced natural rubber nanocomposites. 2. Mechanical behavior. Biomacromolecules 4, 666-674.
Gunasekaran, S., Natarajan, R.K., Kala, A., 2007. FTIR spectra and mechanical strength analysis of some selected rubber derivatives. Spectrochim. Acta, Part A 68, 323-330.
Ishida, H., Rodriguez, Y., 1995. Curing kinetics of a new benzoxazine-based phenolic resin by differential scanning calorimetry. Polymer 36, 3151-3158.
Jackson, M., Mantsch, H.H., 1995. The use and misuse of FTIR spectroscopy in the determination of protein structure. Crit. Rev. Biochem. Mol. Biol. 30, 95-120.
Jong, L., 2005. Rubber composites reinforced by soy spent flakes. Polym. Int. 54, 1572-1580.
Kc, B., Faruk, O., Agnelli, J.A.M., Leao, A.L., Tjong, J., Sain, M., 2016. Sisal-glass fiber hybrid biocomposite: Optimization of injection molding parameters using Taguchi method for reducing shrinkage. Composites Part A 83, 152-159.
Keten, S., Xu, Z., Ihle, B., Buehler, M.J., 2010. Nanoconfinement controls stiffness, strength and mechanical toughness of β-sheet crystals in silk. Nat. Mater. 9, 359-367.
Kieffer, R., Schurer, F., Köhler, P., Wieser, H., 2007. Effect of hydrostatic pressure and temperature on the chemical and functional properties of wheat gluten: studies on gluten, gliadin and glutenin. J. Cereal Sci. 45, 285-292.
Knowles, T.P.J., Buehler, M.J., 2011. Nanomechanics of functional and pathological amyloid materials. Nat. Nanotechnol. 6, 469-479.
Kraus, G., 1963. Swelling of filler-reinforced vulcanizates. J. Appl. Polym. Sci. 7, 861-871.
Krejsa, M., Koenig, J., 1993. A review of sulfur crosslinking fundamentals for accelerated and unaccelerated vulcanization. Rubber Chem. Technol. 66, 376-410.
Le Xuan, H., Decker, C., 1993. Photocrosslinking of acrylated natural rubber. J. Polym. Sci., Part A: Polym. Chem. 31, 769-780.
Leroy, E., Souid, A., Sarda, A., Deterre, R., 2013. A knowledge based approach for elastomer cure kinetic parameters estimation. Polym. Test. 32, 9-14.
Lion, A., 1996. A constitutive model for carbon black filled rubber: Experimental investigations and mathematical representation. Continuum Mech. Thermodyn. 8, 153-169.
López-Manchado, M., Arroyo, M., Herrero, B., Biagiotti, J., 2003. Vulcanization kinetics of natural rubber–organoclay nanocomposites. J. Appl. Polym. Sci. 89, 1-15.
Loukil, M.T., Corvec, G., Robin, E., Miroir, M., Le Cam, J.B., Garnier, P., 2018. Stored energy accompanying cyclic deformation of filled rubber. Eur. Polym. J. 98, 448-455.
MacCallum, J., Tanner, J., 1970. Derivation of rate equations used in thermogravimetry. Nature 225, 1127-1128.

Masłowski, M., Miedzianowska, J., Strzelec, K., 2017. Natural rubber biocomposites containing corn, barley and wheat straw. Polym. Test. 63, 84-91.
Messori, M., Bignotti, F., De Santis, R., Taurino, R., 2009. Modification of isoprene rubber by in situ silica generation. Polym. Int. 58, 880-887.
Michaelsen, C., Barmak, K., Weihs, T.P., 1997. Investigating the thermodynamics and kinetics of thin film reactions by differential scanning calorimetry. J. Phys. D: Appl. Phys. 30, 3167.
Miyazawa, T., Shimanouchi, T., Mizushima, S.i., 1956. Characteristic infrared bands of monosubstituted amides. J. Chem. Phys. 24, 408-418.
Mori, M., Koenig, J.L., 1998. Solid-state 13C-NMR and equilibrium-swelling studies of filled, TBBS-accelerated sulfur vulcanization of natural rubber. J. Appl. Polym. Sci. 70, 1391-1399.
Mullins, L., 1948. Effect of stretching on the properties of rubber. Rubber Chem. Technol. 21, 281-300.
Nie, Y., Huang, G., Qu, L., Zhang, P., Weng, G., Wu, J., 2010. Cure kinetics and morphology of natural rubber reinforced by the in situ polymerization of zinc dimethacrylate. J. Appl. Polym. Sci. 115, 99-106.
Oppenheim, T., Knowles, T.P., Lacour, S.P., Welland, M.E., 2010. Fabrication and characterisation of protein fibril–elastomer composites. Acta Biomater. 6, 1337-1341.
Park, G., Park, H., 2018. Structural design and test of automobile bonnet with natural flax composite through impact damage analysis. Compos. Struct. 184, 800-806.
Porter, M., 1967. Structural characterization of filled vulcanizates part 1. Determination of the concentration of chemical crosslinks in natural rubber vulcanizates containing high abrasion furnace black. Rubber Chem. Technol. 40, 866-882.
Rao, S.P., Meade, S.J., Healy, J.P., Sutton, K.H., Larsen, N.G., Staiger, M.P., Gerrard, J.A., 2012. Amyloid fibrils as functionalizable components of nanocomposite materials. Biotechnol. Prog. 28, 248-256.
Ridgley, D.M., Claunch, E.C., Barone, J.R., 2012. The effect of processing on large, self-assembled amyloid fibers. Soft Matter 8, 10298-10306.
Ridgley, D.M., Claunch, E.C., Barone, J.R., 2013. Characterization of large amyloid fibers and tapes with Fourier Transform Infrared (FT-IR) and raman spectroscopy. Appl. Spectrosc. 67, 1417-1426.
Ridgley, D.M., Claunch, E.C., Lee, P.W., Barone, J.R., 2014. The role of protein hydrophobicity in conformation change and self-assembly into large amyloid fibers. Biomacromolecules 15, 1240-1247.
Rolere, S., Bottier, C., Vaysse, L., Sainte-Beuve, J., Bonfils, F., 2016. Characterisation of macrogel composition from industrial natural rubber samples: Influence of proteins on the macrogel crosslink density. Express Polym. Lett. 10, 408.
Rolere, S., Liengprayoon, S., Vaysse, L., Sainte-Beuve, J., Bonfils, F., 2015. Investigating natural rubber composition with Fourier Transform Infrared (FT-IR) spectroscopy: A rapid and non-destructive method to determine both protein and lipid contents simultaneously. Polym. Test. 43, 83-93.
Rubinstein, M., Colby, R.H., 2003. Polymer Physics. Oxford University Press, Oxford.
Rwawiire, S., Tomkova, B., Militky, J., Jabbar, A., Kale, B.M., 2015. Development of a biocomposite based on green epoxy polymer and natural cellulose fabric (bark cloth) for automotive instrument panel applications. Composites Part B 81, 149-157.

Salomon, G., Van Der Schee, A.C., 1954. Infrared analysis of isomerized, vulcanized and oxidized natural rubber. J. Polym. Sci. 14, 181-192.
Shaw, M.T., MacKnight, W.J., 2005. Elasticity of Rubbery Networks, Introduction to Polymer Viscoelasticity. John Wiley & Sons, Inc., pp. 165-212.
Soratana, K., Rasutis, D., Azarabadi, H., Eranki, P.L., Landis, A.E., 2017. Guayule as an alternative source of natural rubber: A comparative life cycle assessment with Hevea and synthetic rubber. J. Clean. Prod. 159, 271-280.
Thomas, S., Stephen, R., 2010. Rubber nanocomposites: preparation, properties and applications. John Wiley & Sons.
Torre, L., Puglia, D., Iannoni, A., Terenzi, A., 2013. Modeling of the Chemorheological Behavior of Thermosetting Polymer Nanocomposites, Modeling and Prediction of Polymer Nanocomposite Properties. Wiley-VCH Verlag GmbH & Co. KGaA, pp. 255-287.
Tuck, C.S., Latham, A., Lee, P.W., Barone, J.R., 2014. Wheat Gluten Plasticized with Its Own Hydrolysate. J. Polym. Environ. 22, 430-438.
Valentín, J., Carretero-González, J., Mora-Barrantes, I., Chassé, W., Saalwachter, K., 2008. Uncertainties in the determination of cross-link density by equilibrium swelling experiments in natural rubber. Macromolecules 41, 4717-4729.
Van Genderen, E., Wildnauer, M., Santero, N., Sidi, N., 2016. A global life cycle assessment for primary zinc production. Int. J. Life Cycle Assess. 21, 1580-1593.
Wan, M., Isayev, A., 1996. Injection molding of rubber compound with rheology affected by vulcanization: part II. Modeling and experiment. Rubber Chem. Technol. 69, 294-312.
Wang, M.-J., 1999. The role of filler networking in dynamic properties of filled rubber. Rubber Chem. Technol. 72, 430-448.
Warren-Thomas, E., Dolman, P.M., Edwards, D.P., 2015. Increasing Demand for Natural Rubber Necessitates a Robust Sustainability Initiative to Mitigate Impacts on Tropical Biodiversity. Conserv. Lett. 8, 230-241.
Weegels, P.L., Marseille, J.P., Hamer, R.J., 1992. Enzymes as a Processing Aid in the Separation of Wheat Flour into Starch and Gluten. Starch - Stärke 44, 44-48.
Wu, J., Xing, W., Huang, G., Li, H., Tang, M., Wu, S., Liu, Y., 2013. Vulcanization kinetics of graphene/natural rubber nanocomposites. Polymer 54, 3314-3323.
Xie, Y., Hill, C.A.S., Xiao, Z., Militz, H., Mai, C., 2010. Silane coupling agents used for natural fiber/polymer composites: A review. Composites Part A 41, 806-819.
Yang, S.S., Nasr, N., Ong, S.K., Nee, A.Y.C., 2017. Designing automotive products for remanufacturing from material selection perspective. J. Clean. Prod. 153, 570-579.
Zhou, Y., Fan, M., Chen, L., Zhuang, J., 2015. Lignocellulosic fibre mediated rubber composites: An overview. Composites Part B 76, 180-191.

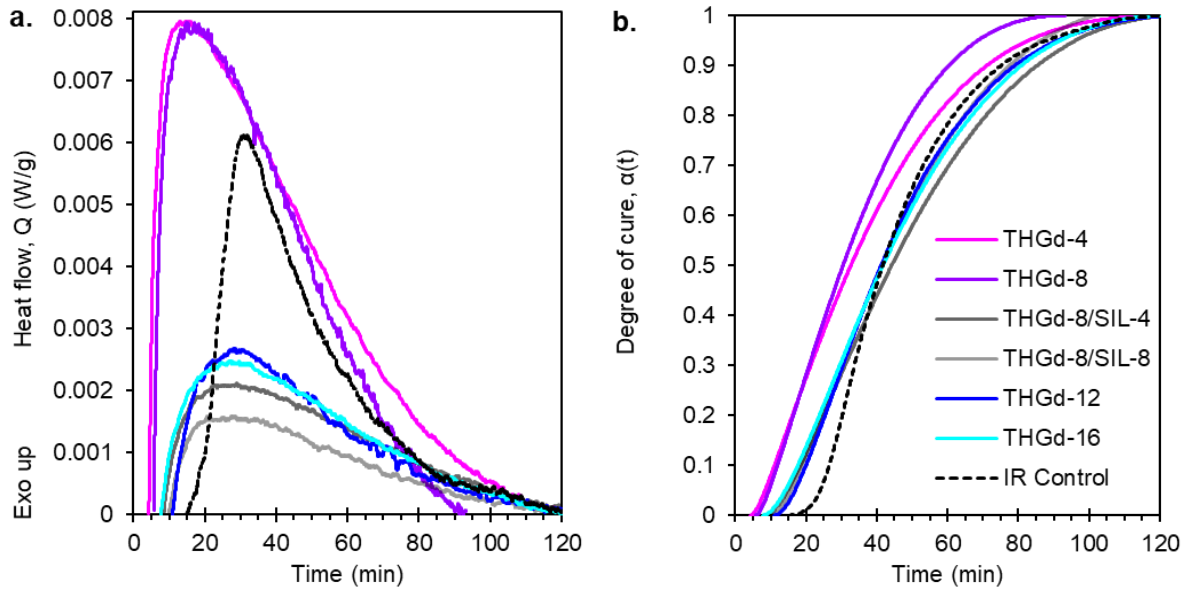


**Figure 1.** (a) 150 °C isotherms for IR Control (dashed line) and THGd-IR (solid lines) compounds showing heat flow (Q) as a function of time. A y-axis shift has been applied to the thermograms. (b) Degree of cure (α) as a function of time, found by numerically approximating the integral of Q with respect to time and normalizing by the area under the exotherm for the compounds shown in (1a).

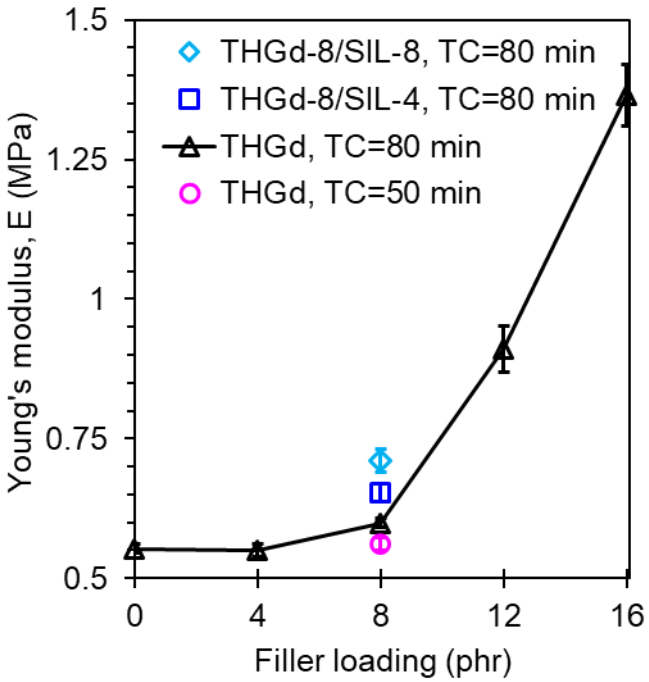


**Figure 2.** Young's modulus (E) ± standard error as a function of filler loading for THGd-IR vulcanizates with silane (THGd-8/SIL) and without silane (THGd). The cure time (TC) is given in the legend.

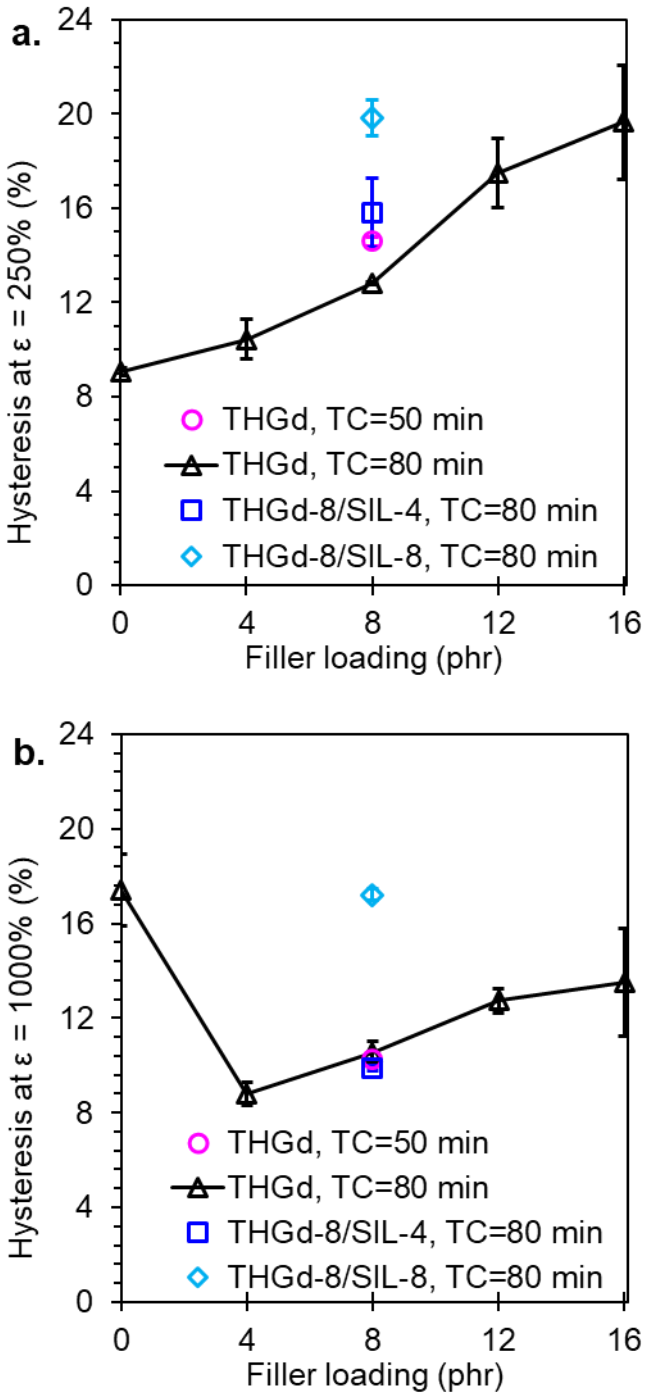


**Figure 3.** Tensile hysteresis ± standard error as a function of filler loading after 6 conditioning cycles at (a) 250 % elongation, and, (b) 1000 % elongation for THGd filled vulcanizates with silane (THGd-8/SIL) and without silane (THGd). The cure time (TC) is given in the legend.

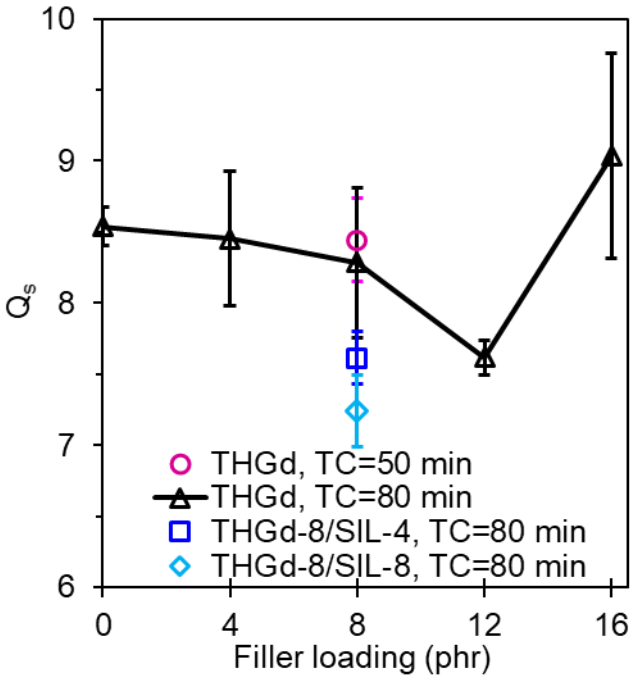


**Figure 4**. Equilibrium volume swelling ratio, $Q_s$ ± standard error as a function of filler loading, for THGd-IR vulcanizates with silane (THGd-8/SIL) and without silane (THGd). The cure time (TC) is given in the legend.

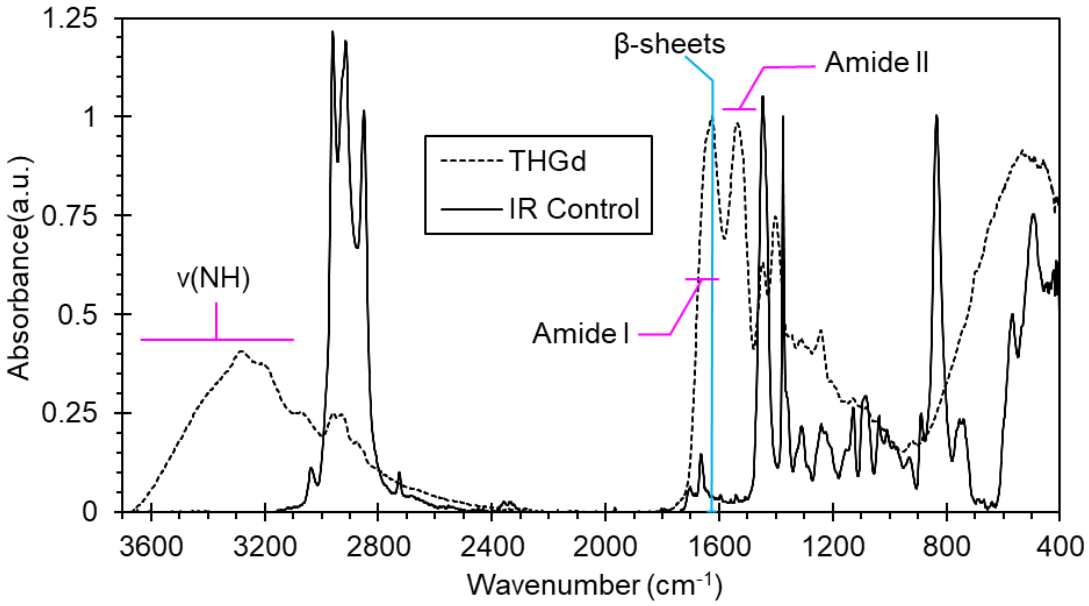


**Figure 5.** FTIR spectra for neat THGd (dashed line), normalized to the 1625 $cm^{-1}$ β-sheet absorbance in the protein Amide I region, and the IR control (solid line), normalized to the 1375 $cm^{-1}$ $\nu(CH_3)$ absorbance.

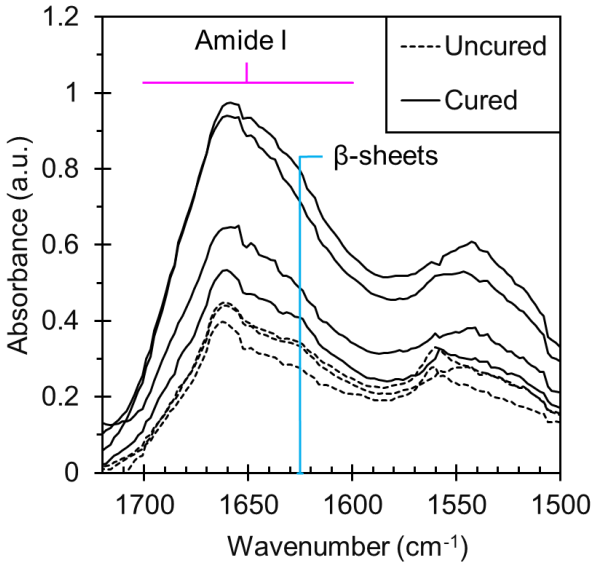


**Figure 6.** FTIR spectra normalized to the IR 1375 $cm^{-1}$ $\nu(CH_3)$ absorbance for uncured (dashed line) and cured (solid line) THGd-12.

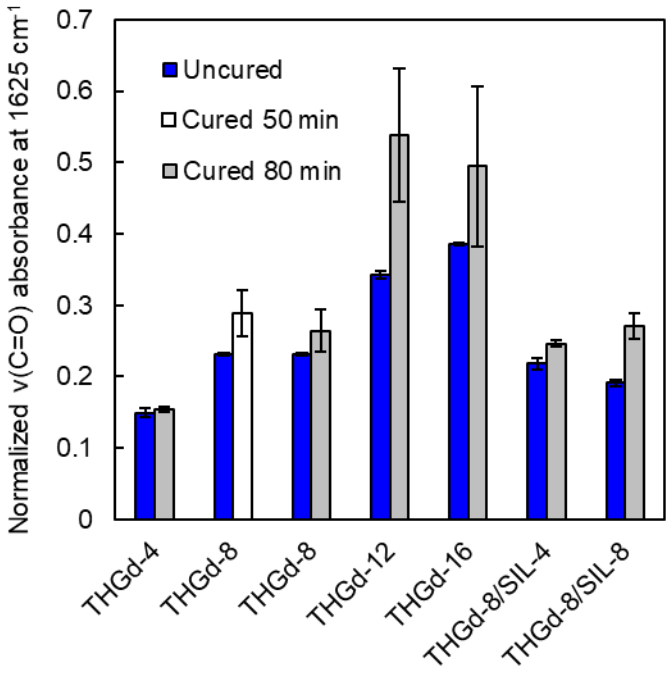


**Figure 7.** Changes in the normalized FTIR Amide I β-sheet aggregation absorbance, ν(C=O) at 1625 $cm^{-1}$, with curing for THGd-filled compounds. The spectra are normalized to the IR 1375 $cm^{-1}$ ν($CH_3$) absorbance so the figure shows the amount of THGd β-sheets relative to IR matrix. Absorbance given as mean ± standard error for uncured compounds (blue columns), vulcanizates cured for 50 min (open column) or 80 min (light grey columns).

**Table 1.** Compound formulations.

| Compound | TBBS (phr) | THGd (phr) | S (phr) | Silane (phr) | [c]TC (min) |
|---|---|---|---|---|---|
| IR Control, 50 min | 0.6 | ---- | 2.5 | ---- | 50 |
| [a]THGd-8, 50 min | 0.6 | 8 | 2.5 | ---- | 50 |
| [a]THGd-4, 80 min | 0.6 | 4 | 2.5 | ---- | 80 |
| [a]THGd-8, 80 min | 0.6 | 8 | 2.5 | ---- | 80 |
| [a]THGd-12, 80 min | 0.6 | 12 | 2.5 | ---- | 80 |
| [a]THGd-16, 80 min | 0.6 | 16 | 2.5 | ---- | 80 |
| [a,b]THGd-8/SIL-4,80 min | 0.6 | 8 | 2.5 | 4 | 80 |
| [a,b]THGd-8/SIL-8,80 min | 0.6 | 8 | 2.5 | 8 | 80 |

[a]protein containing compounds denoted as "THGd-x," where "x" is the protein concentration, given in phr; [b]compounds given as "THGd-x/SIL-y," where "y" is the concentration of (3-mercaptopropyl)triethoxysilane, given in phr; [c]cure time.

**Table 2.** Compounding steps for the formulations in Table I.

| THGd:IR | [a]$t_{step}$ (min) | [b]$t_{tot}$ (min) |
|---|---|---|
| 1. Add IR. | 0.5 | 0.5 |
| 2. Add TBBS. | 0.5 | 1 |
| 3. Add THGd (optional). | 1 | 2 |
| 4. Add SIL (optional). | 4 | 6 |
| 5. Add S. | 6 | 7 |

[a]mixing time per step; [b]total mixing time for the compound.

**Table 3.** DSC curing kinetics, given as the mean ± standard error.

| Compound | [a]$t_{05}$ (min) | [b]$t_{90}$ (min) | [c]$\Delta t$ (min) | [d]CRI ($min^{-1}$) | [e]$\Delta H$ (J/g) | [f]$\overline{E}_{\alpha}$ (kJ/mol) |
|---|---|---|---|---|---|---|
| IR Control | 25.9±1.3 | 77.9±1.8 | 51.9±2.3 | 1.92±0.02 | 14.0±2.1 | 71.5±8.0 |
| THGd-4 | 12.3±2.6 | 72.5±0.7 | 60.2±2.7 | 1.67±0.06 | 14.5±2.3 | 82.0±1.7 |
| THGd-8 | 10.2±0.4 | 61.1±0.7 | 50.9±0.8 | 1.96±0.01 | 12.9±1.9 | 76.6±3.2 |
| THGd-12 | 16.4±0.6 | 75.3±3.6 | 58.9±3.6 | 1.71±0.09 | 3.7±1.1 | 94.3±7.1 |
| THGd-16 | 15.7±0.9 | 77.4±4.1 | 61.8±3.6 | 1.64±0.14 | 4.3±1.1 | 97.2±6.0 |
| THGd-8/SIL-4 | 16.7±1.1 | 82.0±3.6 | 65.3±3.7 | 1.55±0.11 | 9.0±0.7 | 84.3±4.6 |
| THGd-8/SIL-8 | 23.4±7.2 | 95.6±12.4 | 72.2±13.9 | 1.40±0.11 | 3.0±0.7 | 82.9±4.8 |

[a]time to reach 5% cure; [b]time to reach 90% cure; [c]elapsed curing time; [d]Cure Rate Index; [e]heat of reaction; [f]average activation energy; [a-d]collected from DSC curing exotherms at 150 °C; [e,f]calculated from all isothermal reaction exotherms for a compound.

# CHAPTER VI. AGRICULTURAL PROTEINS AS MULTIFUNCTIONAL ADDITIVES IN ZNO-FREE SYNTHETIC ISOPRENE RUBBER VULCANIZATES

DeButts, B. L., Chauhan, N., & Barone, J. R. (2019). Agricultural proteins as multifunctional additives in ZnO-free synthetic isoprene rubber vulcanizates. *J. App. Polym. Sci.*, (in review).

Chapter VI has been submitted to and is under review by the following peer-reviewed journal: the *Journal of Applied Polymer Science* published by John Wiley & Sons, Inc. The chapter is formatted according to the journal guidelines set forth by the publishers.

Agricultural proteins as multifunctional additives in ZnO-free synthetic isoprene rubber vulcanizates

Barbara L. DeButts[1], Natasha Chauhan[2], and Justin R. Barone[1,3,4*]

[1]Macromolecular Science and Engineering and Macromolecules Innovation Institute, Virginia Tech, Blacksburg, VA, 24061, United States

[2]Department of Chemical Engineering, Virginia Tech, 245 Goodwin Hall, 635 Prices Fork Road, Blacksburg, VA 24061, United States

[3]Biological Systems Engineering, Virginia Tech, 301D Human and Agricultural Biosciences Building 1, 1230 Washington St. SW, Blacksburg, VA 24061, United States

[4]Center for Soft Matter and Biological Physics, Virginia Tech, Blacksburg, VA 24061, United States

[*]Corresponding author email: jbarone@vt.edu (J.R. Barone)

## ABSTRACT

Corn zein and wheat gliadin protein are compounded into synthetic cis-1,4-polyisoprene rubber (IR) and sulfur-cured in a zinc oxide (ZnO)-free system. The curing kinetics and mechanical and morphological properties are compared to a ZnO-activated or carbon black (CB)-reinforced cure system. The proteins provide reversion resistance and reinforcement to IR at filler loadings as low as 1 part per hundred rubber (phr). The zein-IR composites exhibit higher moduli, better filler-matrix adhesion, and less filler agglomeration/migration than gliadin-IR because zein is more chemically compatible with IR. The gliadin-IR composites have a lower percent set and

hysteresis, indicating the formation of an elastic restoring gliadin network. Optimal properties are achieved at 2 phr gliadin and 4 phr zein. At gliadin loading >2 phr and zein loading > 4 phr, the protein domain size increases and mechanical properties deteriorate. At equal filler loading, property improvements over CB-IR are observed for one or both proteins.

## INTRODUCTION

Rubber vulcanization, i.e. curing, is the act of forming an extended network through a covalent crosslinking reaction. It is a complex process in which a many-component system undergoes a series of reactions.[1-4] Industrial cure recipes typically contain an activator system, accelerator, curing agent, reinforcing fillers, processing aid, retardant, compatibilizer, antidegradant, antioxidant, and rubber.[5] The concentration and chemical properties of the additives have been shown to affect the cure kinetics and the final properties of the rubber vulcanizate.[6]

In an effort to improve the sustainability of cured rubber articles, many fillers of biological origin have been investigated and even incorporated into industrial cure packages.[7] Of particular interest are those biofillers which serve as multifunctional additives. For example, Bhattacharyya et al.[8] found that microcrystalline cellulose was an effective partial replacement for a silica reinforcing filler and an aromatic oil processing aid in styrene butadiene rubber. Prochoń and Ntumba[9] added hydrolysates of cattle hair keratin and bird feather wastes to carboxylated nitrile rubber (XNBR) and the composite mechanical properties and oil resistance were improved, while surface abrasion was reduced. A white rice husk ash filler was investigated as a reinforcing filler by Da Costa et al.[10-11] and found to function in a catalytic capacity, accelerating the crosslinking reaction and lowering activation energy ($E_a$). Barrera and Cornish[12-

[13] studied the effect of waste-derived fillers as co-fillers for carbon black and found that eggshell particles increased the rate of cure, which resulted in higher crosslink density and improved mechanical properties. When commercial proteins were added to guayule rubber (GR), Lhamo and McMahan[14] found that the composite green strength, bulk viscosity, and thermo-oxidative stability were improved. In the same study, Lhamo and McMahan probed the interaction of proteins and GR with various antioxidants and found the cure and mechanical properties changed based upon the protein-antioxidant combination, emphasizing the importance of optimizing the entire rubber-additive system.

In the studies given above and in others,[15-18] the biological fillers were investigated in a rubber cure package containing zinc oxide (ZnO). ZnO is commonly used as an activator in sulfur vulcanization to improve vulcanization kinetics, processability, and physical properties, such as abrasion resistance.[19-21] However, the use of ZnO is problematic because it is expensive, high density, and ecotoxic.[5, 22] The Environmental Protection Agency (EPA) and European Union (EU) have suggested that the use of ZnO be reduced due to its detrimental effects on aquatic organisms.[22-26] Many efforts have been made to reduce the quantity and/or particle size of ZnO.[23, 27-28] Few studies have completely eliminated ZnO from the curing package.[19, 29-30]

One property that must be controlled is reversion. Reversion is a form of thermal aging characterized by a loss of crosslink density which negatively impacts the mechanical properties. Reversion is a common problem for sulfur-vulcanized isoprene rubbers because the polysulfidic crosslinks (C-$S_x$-C) formed during curing are thermally labile.[31] To combat reversion, various approaches are used, such as increasing the accelerator to sulfur ratio, curing at a lower temperature for an extended time, or compounding with a sulfur donor, although these methods have undesirable consequences on the processing and/or properties of the vulcanizate.[5, 32] Anti-

reversion agents such as bisimides are commonly added to the cure package to increase thermal stability and maintain mechanical properties. Bisimides are typically used in the presence of zinc oxide (ZnO).[33]

In this work, agricultural proteins were investigated as multifunctional fillers in a ZnO-free, cured, synthetic cis-1,4-polyisoprene rubber (IR) system. The proteins of interest were corn zein and wheat gliadin because of the difference in the hydrophobicity of each protein. Based on its amino acid composition (quantified using the ProtParam tool in UniProt), gliadin was a hydrophilic protein (UniProt P04721, grand average of hydropathicity, GRAVY = -0.913, aliphatic index, AI=74.01), while zein was a hydrophobic protein (UniProt P04700, GRAVY = 0.383, AI=122.93). The role of the proteins as reinforcing fillers and anti-reversion agents was studied. The effect of protein on the curing kinetics, mechanical properties, and composite morphology was evaluated and compared to a system containing a zinc oxide (ZnO) activator or a carbon black (CB) reinforcing filler. The effect of the protein type (i.e., gliadin or zein) and loading was assessed using a cure meter, tensile testing, swelling experiments, and scanning electron microscopy (SEM). The vulcanization kinetics, mechanical properties, crosslink behavior, and morphology of protein-IR vulcanizates demonstrated that gliadin and zein were able to improve the reversion resistance of IR while providing additional reinforcement at concentrations as low as 1 phr without any detrimental effect on the curing kinetics. Thus, the potential for a completely zinc-free rubber curing system exists.

## EXPERIMENTAL

**Materials.** Gliadin from wheat (UniProt P04721, ~30 kDa) and slab synthetic cis-1,4-polyisoprene rubber (IR) were purchased from Sigma-Aldrich (St. Louis, MO). Corn zein (UniProt P04700, ~22 kDa) was purchased from MP Biomedicals, LLC (Solon, OH). Elemental sulfur (S),

carbon black (CB, Vulcan® 7H Cabot), and N-tert-butyl-benzothiazole sulfenamide (TBBS) were graciously provided by Hankook Tire.

**Preparation of protein-IR composites.** The neat materials were compounded in 45 g batches on a Prep-Center with an internal mixing head (Brabender, Hackensack, NJ) according to the formulations in Table 1 and order given in Table 2. All components were measured in parts per hundred rubber (phr). Single stage compounding was performed at 60 rpm for 7 min as specified in ASTM D3182, with an initial temperature of 50 °C and a dump temperature of 88±5 °C.

**Cure meter testing.** Compounds (~3.5 g) were conditioned at room temperature for 1 h, then isothermally cured in triplicate at 150 °C until a 5% reduction in the maximum torque (MH) was attained or 120 min (Rubber Process Analyzer Flex, TA Instruments, Waltham, MA). The amplitude of oscillation was ±0.5 ° and the frequency of oscillation was 1.7 Hz, as per ASTM D5289.

**Preparation of vulcanized sheets.** Compounds were compression molded at 150 °C on a manual hydraulic press (Model #3925, Carver Inc., Wabash, IN) under 0.9 MPa pressure for the t'90 time, as determined from cure meter testing. Steel shims (1 mm thickness) were used to achieve a uniform film thickness.

**Tensile testing.** ASTM D412 Die D tensile specimens were uniaxially deformed to 250 % and 1000 % elongation ($\epsilon$) for 9 cycles at a rate of 500 mm/min on a Texture Analyzer TA.HD*Plus* (Texture Technologies Corp., Hamilton, MA) equipped with a 100-kg load cell and self-tightening crosshatched grips. All tests were performed in triplicate and results reported as an average ± standard error. Young's moduli (E) were calculated by linear regression analysis of the low-strain Hookean region of the stress-strain plots in Excel. The peak stress at maximum elongation,

σ(ϵ=1000%), and permanent set, i.e., the remaining strain at zero load, were recorded. The hysteresis was calculated from Eq. 1, where $A_{loading}$ and $A_{unloading}$ were the areas under the loading and unloading curves, respectively.

$$\%Hysteresis = \left(\frac{A_{loading} - A_{unloading}}{A_{loading}}\right) * 100 \quad (1)$$

**Scanning electron microscopy with energy dispersive X-ray spectroscopy (SEM-EDX).** A tensile specimen from each composite was freeze fractured in liquid nitrogen, then sputter-coated with 5 nm iridium at a 45 ° angle. Micrographs were obtained with a 12.4 mm working distance and 10 kV accelerating voltage (FEI Quanta 600 FEG environmental SEM with a Bruker EDX Silicon Drifted Detector, Thermo Fisher Scientific, Waltham, MA). Oxygen was exclusive to the protein phase, so any Z-contrast arising from oxygen identified the protein phase. A corresponding decrease in the carbon signal intensity confirmed a protein phase domain. Any thermal oxidation of the IR phase during processing was insignificant and was not observed in the EDX spectra or oxygen maps. Li and Koenig[34-35] studied the oxidation of IR and found that an induction time of hours (1.5 h at 140 °C) was required to oxidize a thin surface layer (~100 μm) and that this layer blocked further oxidation. Since the samples tested here were thermally processed for less than 1 h and the fracture surface, rather than the sample surface, was imaged, IR oxidation was not a significant factor in this analysis. Protein aggregates smaller than 1 $\mu m^2$ could not be resolved by the EDX detector but could be distinguished as bright areas in the backscatter electron (BSE) micrographs using a BSE detector. Therefore, EDX elemental maps and BSE micrographs were used in conjunction to identify protein dispersion and morphology in the fracture surface. The surface area (SA), length (l), width (w), and aspect ratio (AR=l/w) of the

protein domains were measured at six magnifications (200x; 500x; 1000x; 2000x; 5000x; 10,000x) with ImageJ software. The protein domains were very heterogeneous in size and the data sets contained many outliers. Since the mean and standard deviation were heavily influenced by outliers, the median was used as a measure of the central tendency in the data and the spread was given by the Median Absolute Deviation (MAD).[36] The justifications for using the median were that the sample size was large (>100) and the protein domain sizes did not follow a normal distribution as determined by the Shapiro-Wilk W-test for Normality[37]

## RESULTS AND DISCUSSION

**Curing kinetics.** A rotorless cure meter was used to assess the cure behavior of the compounds in Table 1, which are cured at 150 °C. The S-shaped cure curves are shown in Figure 1. The cure properties, i.e., minimum torque (ML), change in torque (ΔM), scorch time (ts1), time to 90% cure (t'90), and Cure Rate Index (CRI), were averaged from three replicate tests, and are reported with standard error in Table 3. A graph with the cure parameters identified on the S-curve is given in the Supporting Information (Figure S1). The ts1 was defined as the time to increase the minimum torque by 1 unit (ML+1). The t'90 was calculated from the minimum and maximum torque, where t'90 = minutes to (ML+0.9ΔM). The overall curing kinetics were assessed by the Cure Rate Index (CRI = 100/(t'90-ts1)), which was inversely proportional to the elapsed curing time.

A typical three-stage curing process, consisting of a pre-cure, cure, and post-cure period, was observed for all compounds (Figures 1 and S1). The pre-cure cure period was identifiable as the bottom tail of the "S," where the elastic torque at time t ($M_t$) increased at a slower rate. The time at which curing began, i.e., scorch time (ts1), was deliberately retarded by the use of the delayed-action accelerator, TBBS.[38] It was important to maintain the scorch time of the IR

Control in the presence of the protein filler to ensure the compounds could be properly processed. The pre-cure period, or scorch time (ts1), was slightly suppressed at low protein loadings of 1-2 phr but was otherwise within standard error of the IR Control (Table 3 and Figure 1a). Large decreases in ts1 can create problems in processing applications such as molding, i.e., if the material begins to cure before filling the mold.[39] Typical rubber fillers, such as CB and ZnO, have been shown to decrease the pre-cure period with varying and sometimes conflicting effects on the overall kinetics.[40-41] From Figure 1, it was apparent that CB and ZnO had shorter scorch times than zein and gliadin at equivalent filler loading. A 40% decrease in ts1 from the IR Control was observed for CB-4, with little to no advantage to the overall curing kinetics (CRI) (Table 3 and Figure 1b). Similarly, a decrease in ts1 (-20% of the IR Control) was observed for ZnO-1, although an increase in CRI (+30% of the IR Control) was also observed (Table 3 and Figure 1a).

The change in torque (□M) can be considered a measure of the crosslink density and minimum torque (ML) a measure of the green strength of the uncured compound, i.e., how much the uncured compound can be handled without tearing prior to final cure, which is important when multiple processing and molding steps are involved. The green strength (ML) of IR was decreased at low protein loadings of 1 phr but was otherwise within standard error of the IR Control (Table 3). Thus, small amounts of protein served to plasticize IR, a result that has been found by other authors, and can be advantageous for processing the high molecular weight IR matrix.[14, 42] At comparable protein loadings, ZnO and CB were found to increase green strength more than gliadin or zein. An increase in the elastic torque at time, t, ($M_t$) was observed at 10-20 min, which indicated the onset of curing (Figure 1). During isothermal curing, crosslinks were formed at some rate and the stiffness of the material increased, causing an increase in $M_t$ up to

some maximum torque (MH). The central part of the S-curve, where the slope was the steepest, was parallel for all compounds, indicating that the Peak Cure Rate (PCR) was similar for the filled and unfilled compounds (Figure 1). The decrease in green strength at 1 phr gliadin or zein did not adversely affect the crosslink density of the cured vulcanizate. In all cases, the filled compounds either matched or exceeded the crosslink density of the IR Control, i.e., ΔM, although the increase was minimal (Table 3). The greatest crosslink density was observed for ZnO-1 (+20% over the IR Control), while the protein-filled compounds offered more modest increases in ΔM of up to 14% over the IR Control. It was important that the crosslink density be neither too low nor too high because the former leads to poor abrasion resistance while the latter embrittles the compound and causes processing difficulty.[43]

As the cure period finished and the curing approached the post-cure phase, the cure rate decreased as torque increased until $M_t$=MH and the compound reached 100% cure (Figures 1 and S1). The time at which curing was complete (t'100) was variable based upon whether the compound was filled and which filler was used. From Figure 1, it was apparent that CB-4 cured the fastest, followed by ZnO-1, then the IR Control and, finally, the protein-filled compounds. Although the protein-filled compounds reached t'100 later than the IR Control, indicating slower curing kinetics, the ΔM was generally higher, indicating a higher crosslink density. Thus, if the goal was to match the crosslink density of the IR Control, less curing time would be required in the protein-filled compounds. Isoprene rubber compounds are often incompletely cured to avoid post-cure thermal aging and loss of mechanical properties. Here, a 90% cure was used as the optimum cure.

On average, the protein filled compounds reached 90% cure at 33.3±0.8 min and had a CRI of 6.8±0.3, which was within standard error of the IR Control (t'90=31.5±1.1 min;

CRI=7.9±1.3) (Table 3). Of the protein-filled compounds, the t'90 and CRI of Zein-4 and Zein-6 deviated the most from the IR Control. Other anti-reversion agents, such as 4,4'-bis (maleimido) diphenyl methane (BMDM) have been shown to increase t'90 at similar loadings (5 phr).[31] In that case, the curing kinetics were improved by curing at a higher temperature which was a viable solution due to the increased thermal stability provided by BMDM. An increase in t'90 and decrease in CRI as zein loading increased suggested that the additional zein protein hindered crosslinking.

After maximum torque was reached, curing progressed into the post-cure region. Post-cure behavior can vary based on the compound formulation and curing conditions. In ideal curing behavior, the reaction culminates with irreversible network formation and crosslink formation plateaus, as is common in styrene-butadiene rubbers. However, in real systems, either reversion or "marching curves" (i.e., where a maximum torque is never reached) are common behaviors.[44] Reversion is characterized by crosslink disappearance and a loss of network structure due to non-oxidative thermal degradation.[45] Sulfur-cured isoprene rubbers commonly exhibit reversion behavior.[46] In the compound formulations tested, a decrease in $M_t$ was observed after MH was reached, indicative of reversion (Figure 1). However, the onset of reversion and amount of reversion was different depending on the filler type (Figure 2). The reversion resistance was quantified using the cure curves, in which the following was measured: (1) elapsed time at 100% cure ($\Delta$t'100 = time at MH ± 0.01 dN·m), and, (2) rate of reversion = $|\Delta M_t/\Delta t|$ for all t > t'100 (Figures S1 and 2). Both zein and gliadin fillers had reversion resistance properties, particularly at higher protein loadings of 4-6 phr, meaning that $\Delta$t'100 was increased (Figure 2a) and rate of reversion was decreased (Figure 2b). The greatest improvement in reversion resistance was observed for Gliadin-4, which increased $\Delta$t'100 by 230% and decreased

rate of reversion by 80% over the IR Control. Zein-4 was also beneficial to the reversion resistance: Δt'100 increased by 130% and rate of reversion decreased by 70%. A lesser improvement was observed for CB-4, where Δt'100 was increased by 60% and rate of reversion was decreased by 40% to the IR Control. Conversely, a negative impact on Δt'100 and the rate of reversion was observed with the addition of 1 phr ZnO. During post-cure network maturation, ZnO catalyzes a reduction in sulfur rank, i.e., converting polysulfidic crosslinks into di- or monosulfidic crosslinks, which increases crosslink density, but can contribute to reversion.[5, 28] Thus, the greatest resistance to reversion was observed in the protein-filled compounds, where reversion resistance increased as a function of protein loading.

**Mechanical properties.** Young's modulus (E) was greater in the filled vulcanizates compared to the unfilled IR Control (Figure 3). The amount of IR reinforcement was dependent upon the filler type and loading. At equivalent filler loading, reinforcement was lower in the composites with the traditional fillers, ZnO-1 and CB-4, compared to the protein-IR composites. Although CB is the most common rubber reinforcing filler used in industry, in this study, CB had the poorest reinforcement potential (+5% over the IR Control). The greatest increase in E over the IR Control was observed in the zein-filled composites, with maximum reinforcement occurring at 4 phr zein (E=0.86±0.01 MPa; +55% over the IR control). As the zein loading increased to 6 phr, E remained the same. In the gliadin-filled composites, maximum reinforcement was observed at 2 phr gliadin (+40% over the IR Control), after which E decreased (E=0.61±0.01 MPa; +10% over the IR Control). Since ΔM was similar to the IR Control for the protein-filled vulcanizates, and did not change based upon protein loading, it was expected that the crosslink densities would be similar (Table 3). Therefore, the change in E was

attributed to the reinforcing potential of the proteins, with zein being more effective at reinforcing IR.

Cured rubbers exhibit stress softening upon repeated extension and retraction, meaning that the stress at a constant elongation will decrease as a function of the deformation cycle, which is a process known as the "Mullins effect".[47-48] The amount of stress softening between the first and second cycle has been shown to correlate to other vulcanizate properties like the ultimate tensile strength (UTS).[49] The magnitude of the change in stress at maximum elongation, i.e., $|\Delta\sigma(\epsilon = 1000\%)|$, between the first and second deformation cycle was calculated and is reported as a function of filler loading (Figure 4). In the vulcanizates tested here, both gliadin and zein showed increased stress softening with increasing filler content with zein-filled rubber showing more stress softening than gliadin-filled rubber.

The hysteresis, or energy dissipated during extension and retraction, was calculated as a function of extension/retraction cycle and filler loading (Figure 5). Filled rubbers generally dissipate more energy than un-filled rubbers.[50-51] However, at low protein loadings, the opposite behavior was observed. Zein-1, Gliadin-1, and Gliadin-2 had lower hysteresis than the IR Control, i.e., 0 phr filler. This suggested that at low protein filler loading, more strain energy applied during extension was recovered upon retraction compared to unfilled and highly filled rubber compounds. Gliadin-1 exhibited the lowest hysteresis, i.e., highest elastic recovery, of any sample for all cycles. There are many applications that require low hysteresis at elongations of several hundred to thousand percent, such as rubber bands, gloves, balloons, and threads/fibers for golf balls, amongst others.[52-53] In tire treads, low hysteresis is important to lowering rolling resistance.[54] Conversely, high hysteresis is problematic because the dissipated energy leads to heat build-up in the vulcanizate. ZnO has high thermal conductivity and so can reduce heat

build-up.[29] Therefore, in the ZnO-free systems, e.g., Gliadin-IR, Zein-IR, and CB-IR, it was especially important to avoid heat build-up, i.e., decrease hysteresis. In cycle 1 for the gliadin- and zein-filled vulcanizates, higher protein loading resulted in larger hysteresis, akin to other rubber fillers.[55-56] Hysteresis decreased with repeat cycling and, after a few extension/retraction cycles, known as the conditioning period, the hysteresis reached a relatively constant value.[57] After the conditioning period, the hysteresis at higher protein loadings of 4 and 6 phr was similar to the IR Control and the CB-filled sample. The hysteresis in ZnO-1 was higher than Zein-1 and Gliadin-1 but similar to the IR Control. So protein fillers behave similarly to traditional rubber reinforcing fillers like carbon black at loadings of 4-6 phr. At these filler loadings, the applied strain energy was dissipated through the re-arrangement of filler particles in the rubber matrix (Figure 5b).[55-56] Low protein filler loadings of 1-2 phr resulted in more energy storage, especially compared to ZnO filler, at increased extension/retraction cycles (Figure 5a). At 1-2 phr filler, there may not be enough filler in the system for re-arrangement to have a significant effect on the energy dissipation. The ZnO result suggested this. It was interesting that the protein fillers had less hysteresis at 1-2 phr and that gliadin in particular had less hysteresis than zein. Gliadin is one of the 3 proteins in wheat gluten and wheat proteins exhibit elastomeric behavior typical of rubber.[58] Zein has some similarities to gliadin particularly in the amount of glutamine (Q) in the structure and is also considered a fairly elastic protein. It appeared that the elastic nature of the proteins contributed to increased energy storage at low loadings.

The remaining strain in the vulcanizate after retraction, i.e., the permanent set, was calculated as a function of cycle and filler loading (Figure 6). A lower permanent set was desirable and indicated less permanent deformation in the sample after an extension and retraction cycle.[52] Permanent set was observed to increase as a function of cycle and was

indicative of increased permanent deformation with repeated applied deformation. Hysteresis occurred because of energy loss in the rubber compound after an applied strain. Hysteresis is typically ascribed to viscous dissipation in the rubber. In filled rubbers, some of the applied deformation energy will go towards re-arranging the filler particles, which is another energy loss mechanism resulting in hysteresis. The permanent set showed that some applied strain energy went toward plastically or permanently deforming the rubber compound, probably through the breaking of IR intra- or inter-molecular bonds and/or breaking up of any filler particle agglomerates. For Zein-4 and Gliadin-2, a decrease in permanent set was observed, which were the same samples that had the highest moduli. This indicated that the highest moduli compounds were more resistant to permanent deformation, but it was not clear why the permanent set did not universally behave as the inverse of the modulus.

**Morphology.** SEM of the fracture surfaces of the protein-IR composites as a function of protein loading are shown in Figure 7. The protein domains in Gliadin-IR and Zein-IR were heterogeneous in size. Gliadin-IR had the largest particles at all protein loadings compared to the Zein-IR composites, with at least one gliadin particle on the order of 0.5-1 mm observable in each fracture surface. The largest gliadin particles were incorporated in the IR matrix and the gliadin particles fractured in the same plane as the IR matrix, indicating that some stress was effectively transferred from the matrix to the particle.[59] However, there were many smaller gliadin particles that had minimal interaction with the surrounding matrix and were unfractured, indicating that no stress transfer from IR matrix to gliadin particles had occurred and gliadin and IR had poor filler/matrix adhesion (Figure 8). The smaller gliadin particles were generally globular or ellipsoidal and were agglomerated throughout the fracture surface. There were large

gaps and voids between the particle edge and the surrounding matrix, demonstrating that the rubber matrix had pulled away from the particle due to poor compatibility.[60]

Comparatively, very few unfractured zein particles were present in the Zein-IR fracture surfaces (Figure 7). The zein particles had smooth fracture surfaces, indicating effective stress transfer from the IR matrix to the zein particle. Although some of the larger zein particles had voids or gaps where the particle surface met the IR matrix, the Zein-IR interface for the small- to mid-size particles showed good interfacial adhesion (Figure 8). The improvement in interfacial adhesion between zein and IR, as compared to gliadin and IR, was likely a contributing factor to the increased moduli in the Zein-IR composites. The median particle surface area was reported with the error of the Median Absolute Deviation (MAD/√n, where n is the number of observations) for gliadin and zein in the composites (Figure 9). A decrease in Young's modulus and increase in percent set was observed at 6 phr zein and 4-6 phr Gd, and these were the composites that had the largest particle surface area (>20 $\mu m^2$). At the same filler loading, the larger particle surface area in the gliadin-IR composites indicated fewer particles. Chemical incompatibility can lead to filler agglomeration/migration and poor filler matrix adhesion, which will decrease mechanical properties.[59] So the more hydrophilic gliadin particles remained agglomerated while the more hydrophobic zein particles dispersed during compounding. Better dispersion resulted in higher moduli in the zein-containing compounds.

The SEM data can be used to rationalize other mechanical property observations. The stress softening increased with increased filler loading. The stress softening was also higher for zein-filled rubber than for gliadin-filled rubber. Stress-softening is a viscoelastic effect, which was why it happened in the IR control. But it is also enhanced in filled rubbers from molecular debonding of the matrix from the filler particle surface. Zein was shown to be more compatible

with the IR matrix because zein was more hydrophobic than gliadin. There were also more zein particles at a given protein loading. Therefore, more stress-softening was expected because more IR molecules were adsorbed onto the zein particle surface relative to gliadin particles and that larger number of IR molecules could detach to increase stress softening.

## CONCLUSIONS

This study sought to improve the performance of cured rubber by investigating the reinforcement and reversion resistance potential of two agricultural protein fillers: corn zein and wheat gliadin. The proteins were compounded into synthetic cis-1,4-polyisoprene rubber (IR) and cured in the presence of an accelerator and sulfur. The curing kinetics, mechanical, and morphological properties were compared to an activated cure system containing zinc oxide (ZnO) and a reinforced system containing carbon black (CB). The addition of gliadin and zein to IR positively impacted reversion resistance with no negative impact on the original curing kinetic properties, i.e., the scorch time (ts1), cure time (t'90), change in torque (ΔM), and Cure Rate Index (CRI) were maintained. The reversion resistance was quantified as an extension of the plateau region, i.e., longer elapsed time at 100% cure, and a lower rate of reversion, i.e., decrease in the slope of the reverting curve. Conversely, any improvement in cure properties provided by zinc oxide (ZnO) and carbon black (CB) was at the expense of a suppressed ts1 and decreased reversion resistance.

Modulus increases over the IR Control and CB-reinforced vulcanizate were observed in the zein-IR and gliadin-IR composites. In the zein-filled composites, E increased with protein loading up to 4 parts per hundred rubber (phr) (+55% over the IR control). In the gliadin-filled composites, E reached a maximum at 2 phr Gliadin (+40% over the IR Control), then decreased.

The lowest permanent set, i.e., permanent deformation, was observed for Zein-4 and Gliadin-2. The permanent set was lower in Gliadin-2 than the IR Control. This was the only filled system to improve the elasticity of IR. At the same filler loading, the zein- and gliadin-filled systems had lower percent set than CB-IR. Stress softening was increased in the zein-filled vulcanizates compared to the gliadin-filled vulcanizates, which was attributed to increased filler-matrix debonding because of the larger number of zein particles and increased chemical compatibility between zein and IR. Gliadin-1 exhibited the lowest hysteresis, i.e., highest elastic recovery, of any sample for all cycles. This suggested that the gliadin protein filler stored elastic energy during repeat deformations. After a conditioning period, the hysteresis at higher protein loadings of 4 and 6 phr was similar to the IR Control and the CB filled sample.

## CONFLICTS OF INTEREST

There are no conflicts to declare.

## ACKNOWLEDGEMENTS

This work was supported by the United States Department of Agriculture [grant number USDA-2016-67021-25006].

## REFERENCES

1. Krejsa, M.; Koenig, J. *Rubber Chem. Technol.* 1993, *66*, 376-410.
2. Ding, R.; Leonov, A. *J. Appl. Polym. Sci.* 1996, *61*, 455-463.
3. Loo, C. T. *Polymer* 1974, *15*, 357-365.

4. Kruželák, J.; Sýkora, R.; Hudec, I. *Chem. Pap. - Chem. Zvesti* 2016, *70*, 1533-1555.

5. Erman, B.; Mark, J. E.; Roland, C. M. In The Science and Technology of Rubber; Erman, B.; Mark, J. E.; Roland, C. M., Eds.; Elsevier Academic Press: Boston, 2013; p 816.

6. Chough, S. H.; Chang, D. H. *J. Appl. Polym. Sci.* 1996, *61*, 449-454.

7. Sarkar, P.; Bhowmick, A. K. *J. Appl. Polym. Sci.* 2018, *135*, 45701.

8. Bhattacharyya, S. K.; Parmar, B. S.; Chakraborty, A.; Dasgupta, S.; Mukhopadhyay, R.; Bandyopadhyay, A. *Ind. Eng. Chem. Res.* 2012, *51*, 10649-10658.

9. Prochoń, M.; Ntumba, Y. H. T. *Rubber Chem. Technol.* 2015, *88*, 258-275.

10. Da Costa, H. M.; Visconte, L. L. Y.; Nunes, R. C. R.; Furtado, C. R. G. *J. Appl. Polym. Sci.* 2003, *90*, 1519-1531.

11. Da Costa, H. M.; Visconte, L. L. Y.; Nunes, R. C. R.; Furtado, C. R. G. *J. Appl. Polym. Sci.* 2003, *87*, 1405-1413.

12. Barrera, C. S.; Cornish, K. *Ind. Crops Prod.* 2017, *107*, 217-231.

13. Barrera, C. S.; Cornish, K. *Ind. Crops Prod.* 2016, *86*, 132-142.

14. Lhamo, D.; McMahan, C. *Rubber Chem. Technol.* 2017, *90*, 387-404.

15. Jong, L. *J. Appl. Polym. Sci.* 2013, *130*, 2188-2197.

16. Sakaki, T.; Nakade, S. Rubber composition and method of producing rubber products using the same composition. U.S. Patent 005587411A, Dec. 24, 1996.

17. McMahan, C.; Lhamo, D. *Rubber Chem. Technol.* 2015, *88*, 310-323.

18. Masłowski, M.; Miedzianowska, J.; Strzelec, K. *Polym. Test.* 2017, *63*, 84-91.

19. Heideman, G.; Noordermeer, J. W.; Datta, R. N.; van Baarle, B. *Rubber Chem. Technol.* 2006, *79*, 561-588.

20. Das, A.; Wang, D.-Y.; Leuteritz, A.; Subramaniam, K.; Greenwell, H. C.; Wagenknecht, U.; Heinrich, G. *J. Mater. Chem.* 2011, *21*, 7194-7200.

21. Manoharan, P.; Chandra Das, N.; Naskar, K. *Biopolymers* 2017, *107*.

22. Bindu, P.; Thomas, S. *J. Phys. Chem. B* 2013, *117*, 12632-12648.

23. Panampilly, B.; Thomas, S. *Polym. Eng. Sci.* 2013, *53*, 1337-1346.

24. Dale, A. L.; Lowry, G. V.; Casman, E. A. *Environ. Sci. Technol.* 2015, *49*, 7285-7293.

25. Ma, H.; Williams, P. L.; Diamond, S. A. *Environ. Pollut.* 2013, *172*, 76-85.

26. Wu, B.; Torres-Duarte, C.; Cole, B. J.; Cherr, G. N. *Environ. Sci. Technol.* 2015, *49*, 5760-5770.

27. Roy, K.; Alam, M. N.; Mandal, S. K.; Debnath, S. C. *J. Nanostruct. Chem.* 2014, *4*, 133-142.

28. Heideman, G.; Datta, R.; Noordermeer, J. W.; van Baarle, B. *J. Appl. Polym. Sci.* 2005, *95*, 1388-1404.

29. Heideman, G.; Datta, R. N.; Noordermeer, J. W.; van Baarle, B. *Rubber Chem. Technol.* 2004, *77*, 512-541.

30. Sandstrom, P. H. Vulcanization accelerating diamines. U.S. Patent 4824914 A, April 25, 1989.

31. Gopisathi, S.; Park, C.; Huh, Y. I.; Jeon, J.; Yun, C. H.; Won, J.; Jeong, K.-U.; Nah, C. *Rubber Chem. Technol.* 2018.

32. Kawai, N. Method for producing modified polymer, and rubber composition. U.S. Patent 9969850, May 15, 2018.

33. Sathi, S. G.; Jeon, J.; Won, J.; Nah, C. *J. Polym. Res.* 2018, *25*, 108.

34. Li, G.-Y.; Koenig, J. L. *Appl. Spectrosc.* 2002, *56*, 1390-1396.

35. Li, G.-Y.; Koenig, J. L. *Rubber Chem. Technol.* 2005, *78*, 355-390.

36. Leys, C.; Ley, C.; Klein, O.; Bernard, P.; Licata, L. *J. Exp. Soc. Phychol.* 2013, *49*, 764-766.

37. Royston, J. P. *J. Roy. Stat. Soc. Ser. C. (Appl. Stat.)* 1982, *31*, 115-124.

38. Ghosh, P.; Katare, S.; Patkar, P.; Caruthers, J. M.; Venkatasubramanian, V.; Walker, K. A. *Rubber Chem. Technol.* 2003, *76*, 592-693.

39. Engels, H.-W.; Weidenhaupt, H.-J.; Pieroth, M.; Hofmann, W.; Menting, K.-H.; Mergenhagen, T.; Schmoll, R.; Uhrlandt, S., Rubber, 9. Chemicals and Additives. In *Ullmann's Encyclopedia of Industrial Chemistry*, Wiley-VCH Verlag GmbH & Co. KGaA: Weinheim, 2011; pp 1-66.

40. Wu, J.; Xing, W.; Huang, G.; Li, H.; Tang, M.; Wu, S.; Liu, Y. *Polymer* 2013, *54*, 3314-3323.

41. Coran, A. Y. *J. Appl. Polym. Sci.* 2003, *87*, 24-30.

42. Qureshi, M. N.; Qammar, H. *Mater. Sci. Eng., C* 2010, *30*, 590-596.

43. Galizio, B. C.; Randall, A. M.; Clark, M. M. Rubber compositions containing carbon black and whey protein. U.S. Patent 20190031837A1, January 31, 2019.

44. López-Manchado, M.; Arroyo, M.; Herrero, B.; Biagiotti, J. *J. Appl. Polym. Sci.* 2003, *89*, 1-15.

45. Leroy, E.; Souid, A.; Sarda, A.; Deterre, R. *Polym. Test.* 2013, *32*, 9-14.

46. Milani, G.; Leroy, E.; Milani, F.; Deterre, R. *Polym. Test.* 2013, *32*, 1052-1063.

47. Mullins, L. *Rubber Chem. Technol.* 1948, *21*, 281-300.

48. Chagnon, G.; Verron, E.; Gornet, L.; Marckmann, G.; Charrier, P. *J. Mech. Phys. Solids* 2004, *52*, 1627-1650.

49. Harwood, J. A. C.; Payne, A. R. *J. Appl. Polym. Sci.* 1966, *10*, 1203-1211.

50. Wang, M.-J. *Rubber Chem. Technol.* 1999, *72*, 430-448.

51. Bergstrom, J. S.; Boyce, M. C. *Rubber Chem. Technol.* 1999, *72*, 633-656.

52. Shamis, M. S.; DeMarco, A. C.; Shawver, S. E.; Wasson, S. C. Elastomeric articles having a welded seam that possess strength and elasticity. U.S. Patent 8,566,965 B2, Oct. 29, 2013.

53. Hamada, A.; Ochi, A.; Mano, S.; Horiuchi, K.; Suzuki, M. Thread rubber for golf balls. U.S. Patent 5,861,465, Jan. 19, 1999.

54. Hall, D. E.; Moreland, J. C. *Rubber Chem. Technol.* 2001, *74*, 525-539.

55. Loukil, M. T.; Corvec, G.; Robin, E.; Miroir, M.; Le Cam, J. B.; Garnier, P. *Eur. Polym. J.* 2018, *98*, 448-455.

56. Boonstra, B. *Polymer* 1979, *20*, 691-704.

57. Lion, A. *Continuum Mech. Thermodyn.* 1996, *8*, 153-169.

58. Shewry, P. R.; Halford, N. G.; Belton, P. S.; Tatham, A. S., Gluten, the elastomeric protein of wheat seeds. In *Elastomeric Proteins*, Shewry, P. R.; Tatham, A. S.; Bailey, A. J., Eds. Cambridge University Press: Cambridge, 2002; pp 279-301.

59. Essabir, H.; Raji, M.; Bouhfid, R.; Qaiss, A. E. K., Nanoclay and Natural Fibers Based Hybrid Composites: Mechanical, Morphological, Thermal and Rheological Properties. In *Nanoclay Reinforced Polymer Composites: Natural Fibre/Nanoclay Hybrid Composites*, Jawaid, M.; Qaiss, A. e. K.; Bouhfid, R., Eds. Springer Singapore: Singapore, 2016; pp 29-49.

60. Gopi Sathi, S.; Jeon, J.; Kim, H. H.; Nah, C. *Plast. Rubber Compos.* 2019, *48*, 115-126.

## TABLES AND FIGURES

**Table 1.** Compound formulations.

| **Compound** | **TBBS** (phr) | **S** (phr) | **Gliadin** (phr) | **Zein** (phr) | **ZnO** (phr) | **CB** (phr) |
|---|---|---|---|---|---|---|
| IR Control | 0.6 | 2.5 | 0 | 0 | 0 | 0 |
| Zein-1 | 0.6 | 2.5 | 0 | 1 | 0 | 0 |
| Zein-2 | 0.6 | 2.5 | 0 | 2 | 0 | 0 |
| Zein-4 | 0.6 | 2.5 | 0 | 4 | 0 | 0 |
| Zein-6 | 0.6 | 2.5 | 0 | 6 | 0 | 0 |
| Gliadin-1 | 0.6 | 2.5 | 1 | 0 | 0 | 0 |
| Gliadin-2 | 0.6 | 2.5 | 2 | 0 | 0 | 0 |
| Gliadin-4 | 0.6 | 2.5 | 4 | 0 | 0 | 0 |
| Gliadin-6 | 0.6 | 2.5 | 6 | 0 | 0 | 0 |
| ZnO-1 | 0.6 | 2.5 | 0 | 0 | 1 | 0 |
| CB-4 | 0.6 | 2.5 | 0 | 0 | 0 | 4 |

**Table 2.** Compounding steps for the IR Control and Protein-IR composites in Table 1, where $t_{step}$ is the mixing time per step and $t_{tot}$ is the total mixing time for the compound.

| Step | $t_{step}$ (min) | $t_{tot}$ (min) |
|---|---|---|
| 1. Add IR. | 0.5 | 0.5 |
| 2. Add TBBS. | 0.5 | 1 |
| 3. Add protein or CB | 1 | 2 |
| 5. Add S. | 6 | 7 |

**Table 3.** Cure properties of compounds in Table 1: minimum torque (ML); torque change (ΔM); scorch time (ts1); cure time (t'90); cure rate index (CRI). All values given as the mean ± standard error.

| Compound | ML (dN·m) | ΔM (dN·m) | ts1 (min) | t'90 (min) | CRI ($min^{-1}$) |
|---|---|---|---|---|---|
| IR Control | 1.39±0.02 | 2.95±0.11 | 18.3±0.9 | 31.5±1.1 | 7.9±1.3 |
| Zein-1 | 1.30±0.01 | 3.35±0.06 | 16.2±0.6 | 32.4±0.4 | 6.2±0.3 |
| Zein-2 | 1.37±0.02 | 2.99±0.20 | 18.2±1.1 | 32.9±0.9 | 6.8±0.3 |
| Zein-4 | 1.35±0.02 | 3.32±0.38 | 18.2±2.0 | 38.3±3.9 | 6.3±2.3 |
| Zein-6 | 1.43±0.01 | 3.19±0.12 | 19.0±0.8 | 39.2±2.1 | 5.1±0.7 |
| Gliadin-1 | 1.32±0.00 | 3.14±0.25 | 16.0±1.5 | 30.3±1.4 | 7.5±1.5 |
| Gliadin-2 | 1.36±0.01 | 3.10±0.20 | 16.7±0.5 | 31.9±1.3 | 6.7±0.6 |
| Gliadin-4 | 1.45±0.03 | 3.09±0.05 | 18.1±0.8 | 30.6±0.8 | 8.1±0.8 |
| Gliadin-6 | 1.36±0.03 | 3.22±0.21 | 17.0±0.8 | 30.9±0.7 | 7.3±0.6 |
| ZnO-1 | 1.44±0.02 | 3.55±0.04 | 14.5±0.8 | 24.2±0.1 | 10.5±0.9 |
| CB-4 | 1.50±0.03 | 3.47±0.30 | 10.7±0.7 | 31.0±6.8 | 5.5±3.1 |

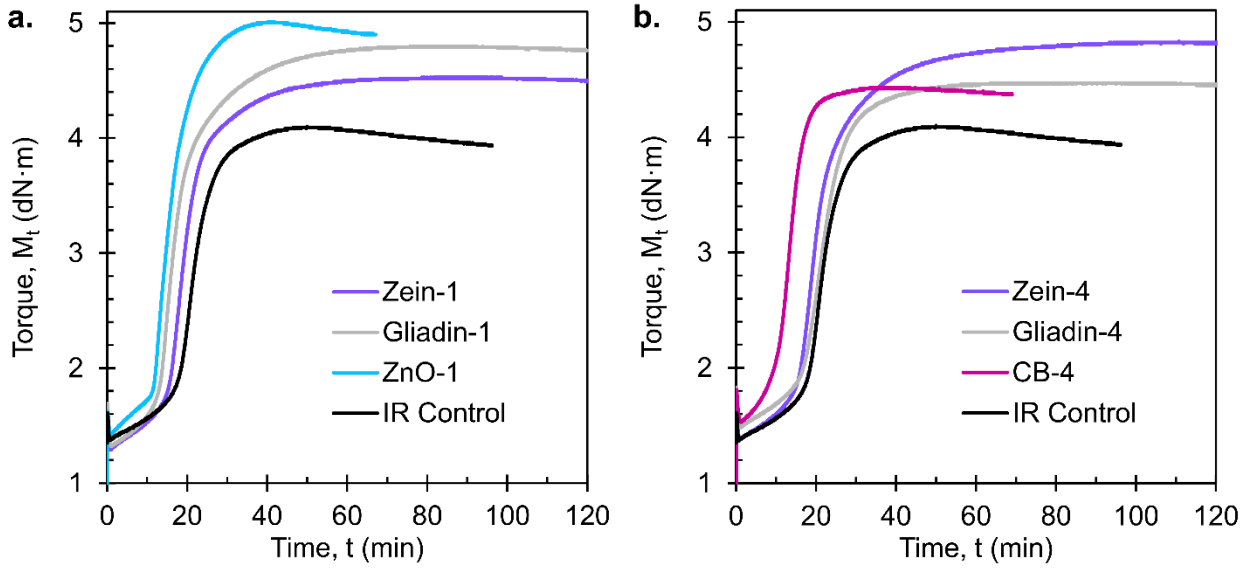


**Figure 1.** Example 150 °C isotherms showing elastic torque ($M_t$) as a function of time for an unfilled IR Control and filled compounds containing (a) 1 phr filler or (b) 4 phr filler.

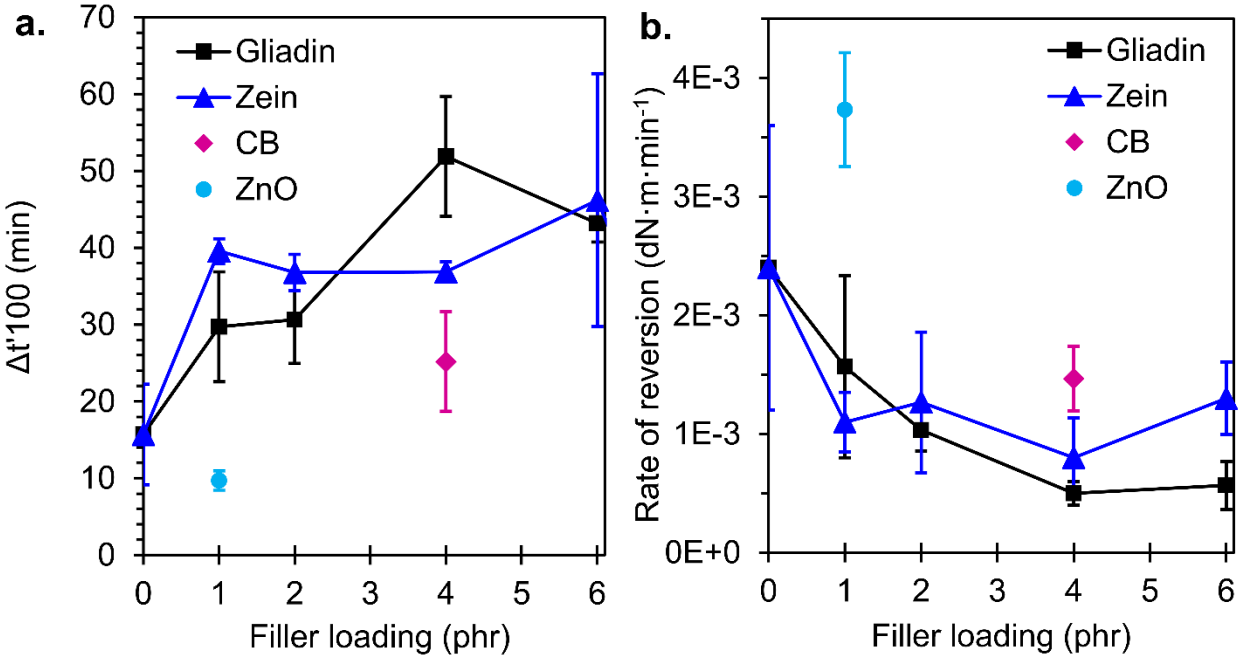


**Figure 2.** Reversion resistance in Gliadin-IR (□), Zein-IR (Δ), CB-IR (◊), and ZnO-IR(○), compounds, quantified as: (a) elapsed time at 100% cure (Δt'100 = time at MH ± 0.01 dN·m), and (b) rate of reversion = $|\Delta M_t/\Delta t|$ for all t > t'100. Values given as the mean ± standard error.

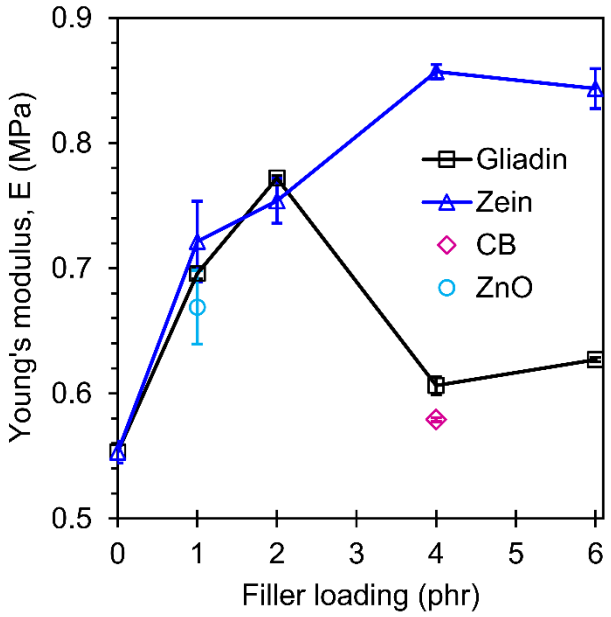


**Figure 3.** Young's modulus (E) as a function of filler loading for Gliadin-IR (□), Zein-IR (Δ), CB-IR (◊), and ZnO-IR(○), vulcanizates. Values given as the mean ± standard error.

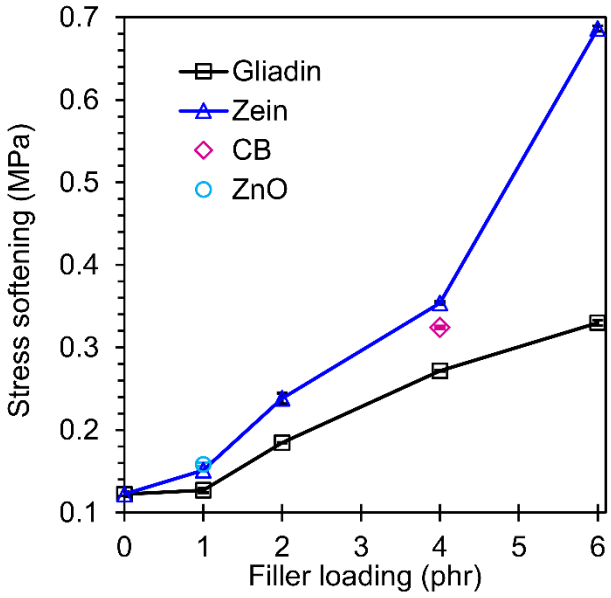


**Figure 4.** Stress softening, quantified as the magnitude of the change in stress at 1000% elongation, $|\Delta\sigma(\epsilon = 1000\%)|$, between deformation cycle 1 and 2, in Gliadin-IR (□), Zein-IR (Δ), CB-IR (◊), and ZnO-IR(○) compounds. Values given as the mean ± standard error.

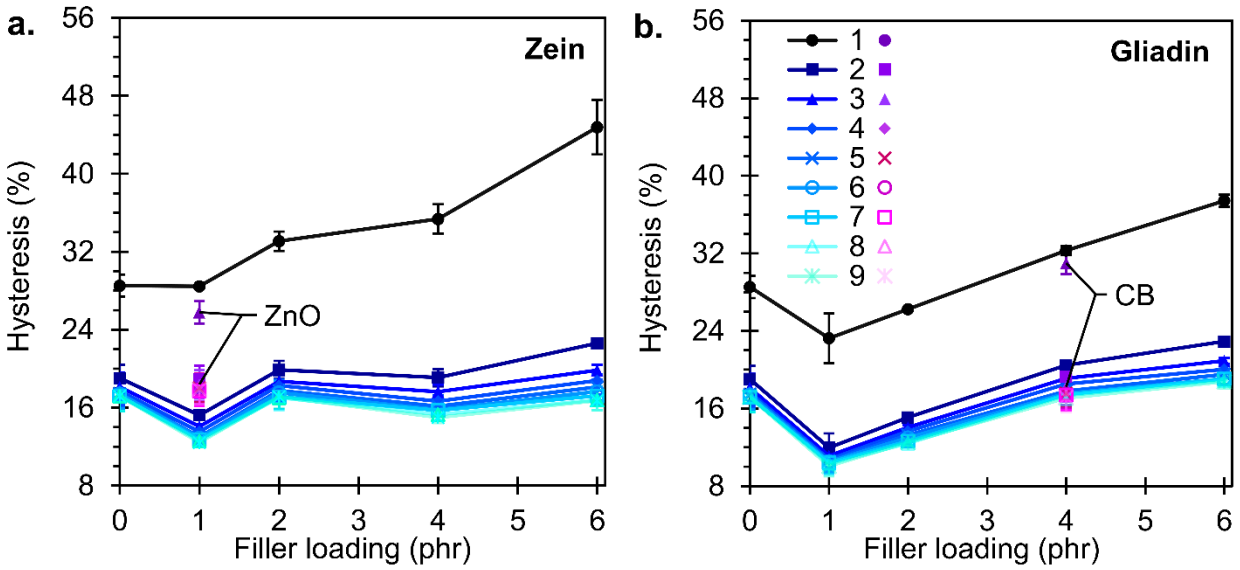


**Figure 5.** Hysteresis as a function of filler loading and extension/retraction cycle (color gradient from dark to light) in: (a) Zein-IR (with ZnO-1 as a reference), and, (b) Gliadin-IR (with CB-4 as a reference) vulcanizates at an applied strain of $\epsilon$=1000 %.

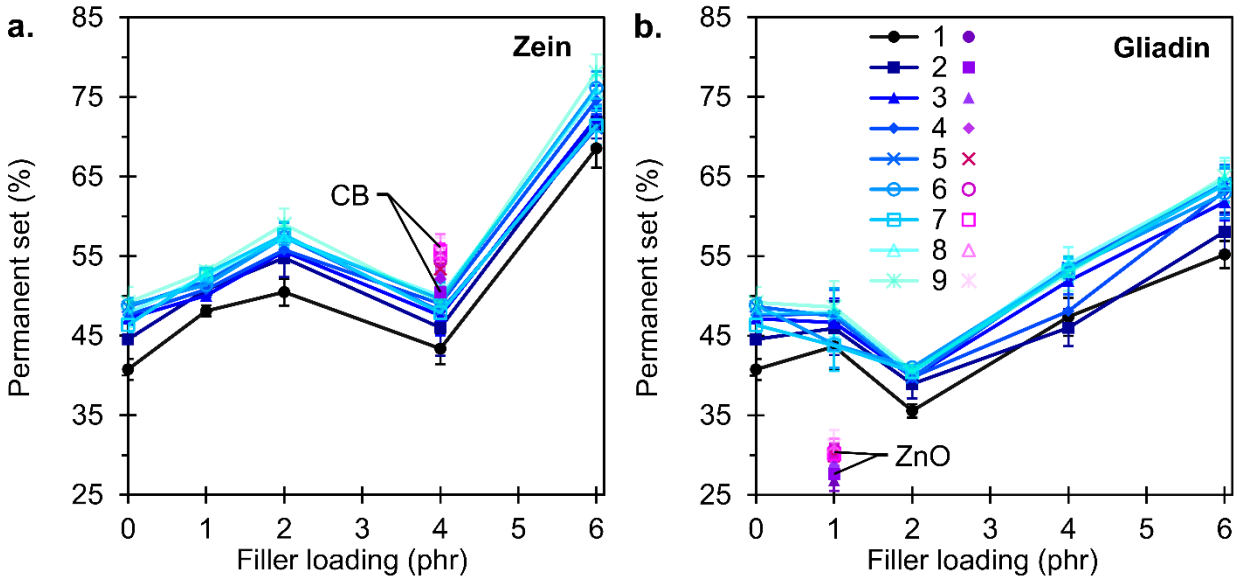


**Figure 6.** Permanent set as a function of filler loading and extension/retraction cycle (color gradient from dark to light) in: (a) Zein-IR (with CB-4 as a reference), and, (b) Gliadin-IR (with ZnO-1 as a reference) vulcanizates at an applied strain of $\epsilon$=1000 %.

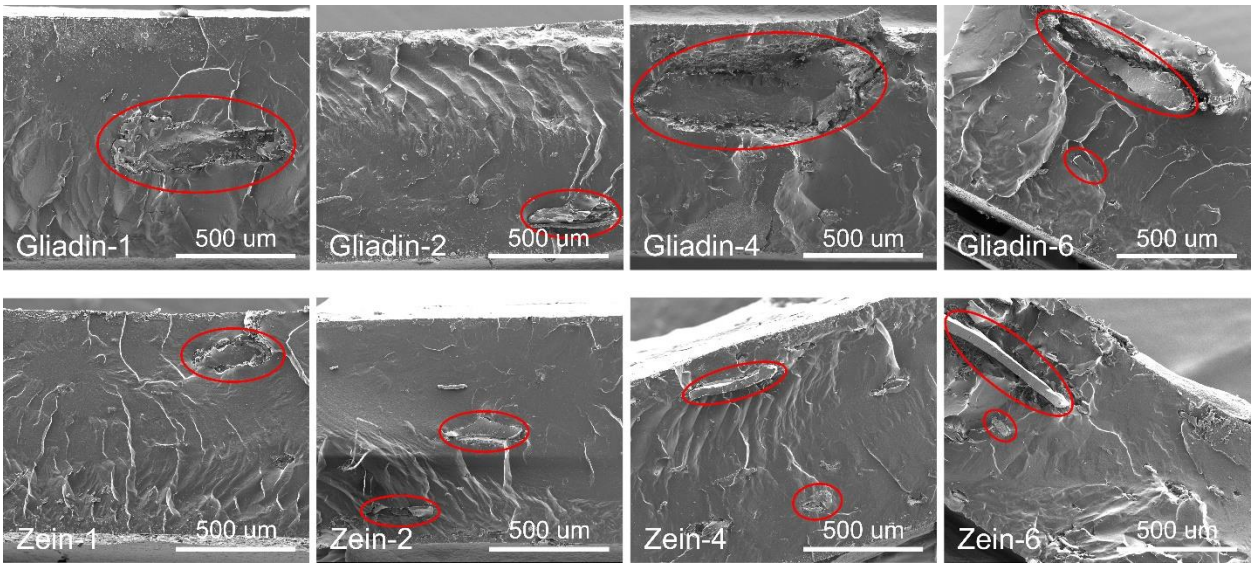


**Figure 7.** SEM of the fracture surface of the Gliadin-IR (top row) and Zein-IR (bottom row) vulcanizates with some of the largest protein domains circled.

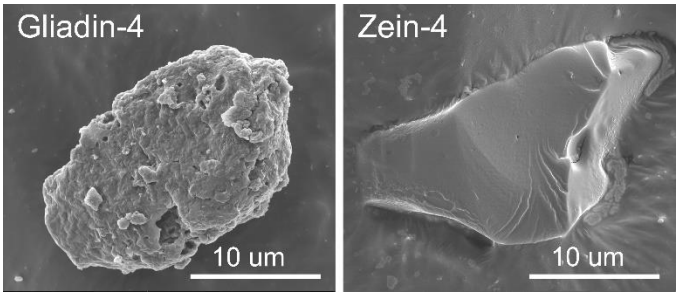


**Figure 8.** SEM of the fracture surface of a protein particle in Gliadin-4 (left) and Zein-4 (right).

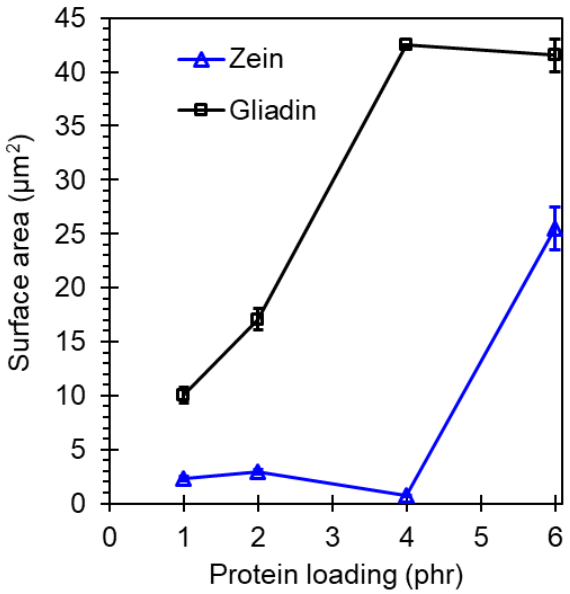


**Figure 9.** Median particle surface area ± error of the Median Absolute Deviation as a function of protein loading in Gliadin-IR (□) and Zein-IR (Δ) vulcanizates.

# CHAPTER VII. CONCLUSIONS

To improve the sustainability of polymer composites, many fillers of biological origin have been investigated and incorporated into commodity polymers. Of particular interest are those biological fillers that serve as multifunctional additives. In this work, agricultural proteins wheat gluten and corn zein were investigated as multifunctional additives (MFAs) in polymer composites. The primary functions of the biological MFAs investigated herein were to: (1) provide reinforcement, (2) improve thermal stability, and (3) lower cost. To maximize the industrial relevance of this work, commodity crops (e.g., wheat and corn) were used because they are widely available, biodegradable, renewable, inexpensive, and can be sourced from agricultural waste. Commodity polymers, poly(vinyl alcohol) (PVA) and synthetic cis-1,4-polyisoprene rubber (IR), were used as matrices. A common application for PVA is flexible packaging and IR is used in tires. The flexible packaging industry and automotive industry are interested in new materials which are sustainable, lower cost, and can be processed using existing industrial methods.

The protein fraction of wheat and corn was utilized because proteins are known to cooperatively self-assemble into various structures in aqueous solution. The mechanism of self-assembly is believed to be universal to all proteins. In the self-assembly route studied here, e.g., amyloid fiber formation, denatured peptides hydrogen bond to form β-sheets, which then stack together to form fibrils or fibers. Protein self-assembly is a hierarchical process, traversing several length scales (nm-cm), and progressing from isotropic paired β-sheet nanostructures to anisotropic fibers. The nanoscale β-sheet phase endows the amyloid fibers with rigidity, toughness, and thermal and mechanical stability. The hierarchical nature of amyloid self-assembly allows for an engineered material with tunable properties. The universality of protein self-assembly presents a unique opportunity to choose a protein additive based upon: (1) environmental factors (i.e., crop production and cost), or (2) the compatibility of the protein with the polymer matrix (i.e., the hydrophobicity of the protein varies with the amino acid sequence).

In Chapter II, trypsin hydrolyzed wheat gluten (THWG) proteins were incubated in aqueous PVA solutions, then the composite solutions were air dried and compression molded into films. Protein aggregates formed through a typical mechanism of β-sheet self-assembly. The

amount of aggregation, i.e., β-sheet self-assembly, was dependent upon the molding conditions and PVA molecular weight. A greater molding time and pressure and/or a lower PVA molecular weight allowed for more protein aggregation. The larger protein structures provided less reinforcement, so these composites had less reinforcement. In Chapters III and IV, wheat proteins THWG and trypsin hydrolyzed gliadin (THGd) were dispersed in synthetic polyisoprene rubber during compounding to form nanocomposites. The composite moduli correlated to the protein β-sheet content and reinforcement increased with increasing protein concentration. The β-sheet containing structures were very thermally stable, even under harsh rubber compounding conditions. By optimizing the processing temperature, compounding time, and protein batch preparation, uniform protein dispersion and optimal IR reinforcement were achieved. In Chapter V, THGd was compounded into IR with a cure accelerator and sulfur curative, then compression molded to cure the rubber. Protein aggregation into nanostructured β-sheets was observed during the curing process. Rubber reinforcement increased as a function of protein concentration and curing time. The results from Chapters II-V showed an interesting concept: *in situ* filler formation in polymer matrices where the choice of polymer and processing conditions influenced the final morphology and composite properties.

For Chapters II-V, the same hydrolyzed wheat proteins, THWG and THGd, were utilized in a hydrophilic matrix (PVA) and a hydrophobic matrix (IR). THWG and THGd are predominantly hydrophilic proteins, with some hydrophobic residues. Anisotropic "spike-like" aggregates were observed in the PVA composites, where good protein-PVA compatibility existed. Isotropic agglomerates of "primary particles" were observed in the IR composites, where the protein and rubber existed as discrete phases and were weakly interacting at most. Thus, the protein morphology and progression along the self-assembly hierarchy was influenced by the protein-polymer interactions. In both systems, larger protein aggregates and/or agglomerates negatively impacted the mechanical properties. In Chapter V, a chemical compatibilizer was added to some of the cured THGd-IR composites. In the compatibilized composites, reinforcement was higher. In Chapter VI, a simplified and direct approach to compatibilization was used: a hydrophobic protein (zein) was substituted for the hydrophilic gliadin protein and compounded and cured in IR. Reinforcement was greater in the zein-IR composites where improved protein-IR compatibility was observed. However, greater mechanical stability was attained using a gliadin filler, and these composites had less permanent deformation and lower

viscous dissipation than the zein-filled composites or, in some cases, the IR Control. Both zein and gliadin improved the thermal stability of IR. These results suggested that alternate property improvements were possible based upon the protein properties, and the choice of protein filler must be based on more than hydrophilic/-phobic character.

During the course of this research, some questions arose that warrant further study. For example, biological systems are inherently heterogeneous which can be problematic for applications which have stringent processing-property requirements. In the systems where *in situ* filler formation was observed, such as the curing of THGd-IR, some areas of the composite had more filler aggregation than others on a microscopic scale. Also not addressed here is the degradability of biological systems and how that is problematic for long term usage of protein-filled polymer composites. A protein filler may be more appropriate for a degradable matrix, such as PVA used here. Additional antidegradants may be necessary to stabilize the protein in a non-degradable matrix, such as IR used here, but the entire rubber-additive system must be optimized.

# APPENDIX A. SUPPORTING INFORMATION: Wheat gluten aggregates as a reinforcement for poly(vinyl alcohol) films

DeButts, B. L., Spivey, C. R., & Barone, J. R. (2017). Wheat Gluten Aggregates as a Reinforcement for Poly (vinyl alcohol) Films. *ACS Sustainable Chemistry & Engineering*, *6*(2), 2422-2430.

# Wheat gluten aggregates as a reinforcement for poly(vinyl alcohol) films

*Barbara L. DeButts[a-c], Cara R. Spivey[d], and Justin R. Barone[b-e]**

[a]Macromolecular Science and Engineering, [b]Macromolecules Innovation Institute, [c]Biological Systems Engineering, Virginia Tech, 301D Human and Agricultural Biosciences Building 1, 1230 Washington St. SW, Blacksburg, VA 24061, [d]NSF RET: Biomechanics from molecular to organismal scales, [e]Center for Soft Matter and Biological Physics, Virginia Tech, Blacksburg, VA 24061

Author. Email address: bdebutts@vt.edu (B. DeButts), caraspivey@gmail.com (C. Spivey).

* Corresponding author. Email address: jbarone@vt.edu (J. Barone).

Number of pages: 3 (including cover sheet)

Number of figures: 2

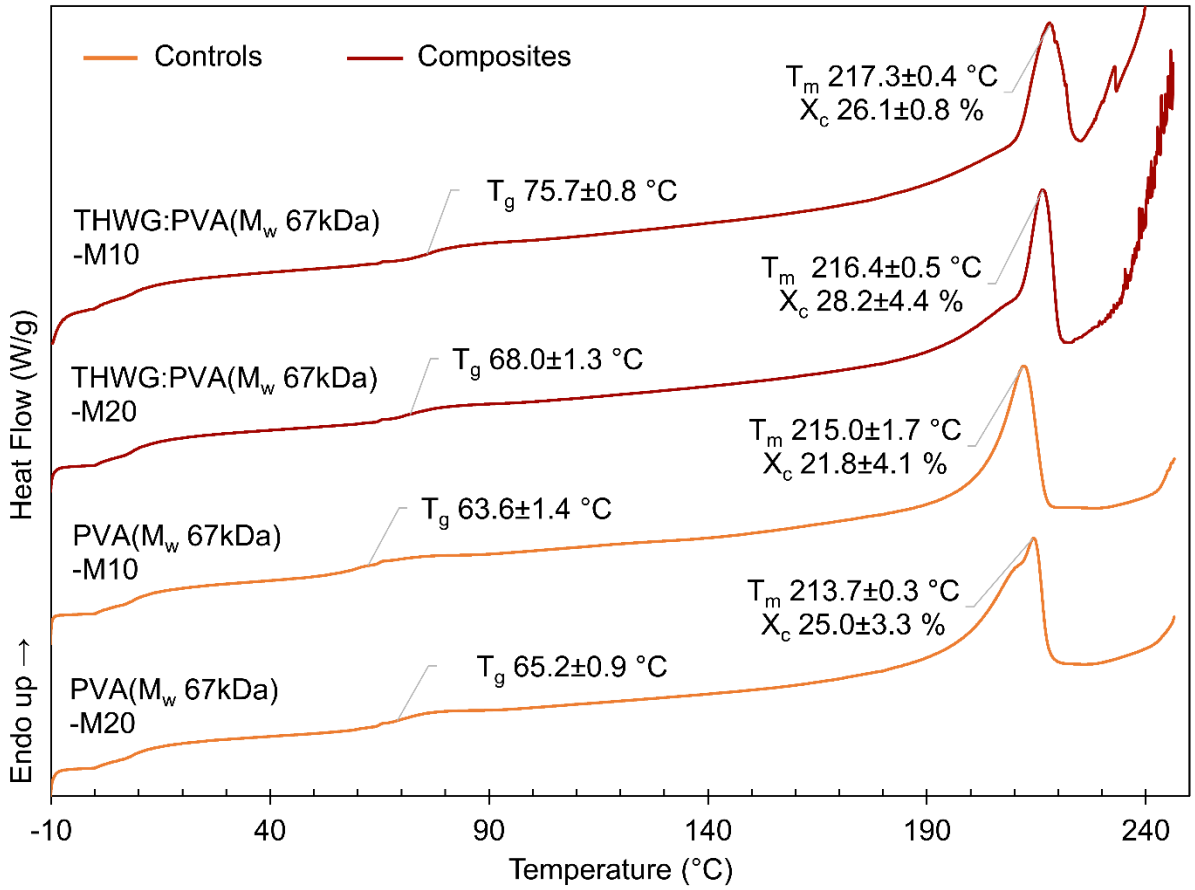


**Figure S1.** DSC second heat scans of PVA control and 33% THWG:PVA composites comparing the effect of processing conditions at constant PVA molecular weight on the PVA and composite thermal properties. Data is also shown along with the modulus data for each material in Table 1 of the manuscript.

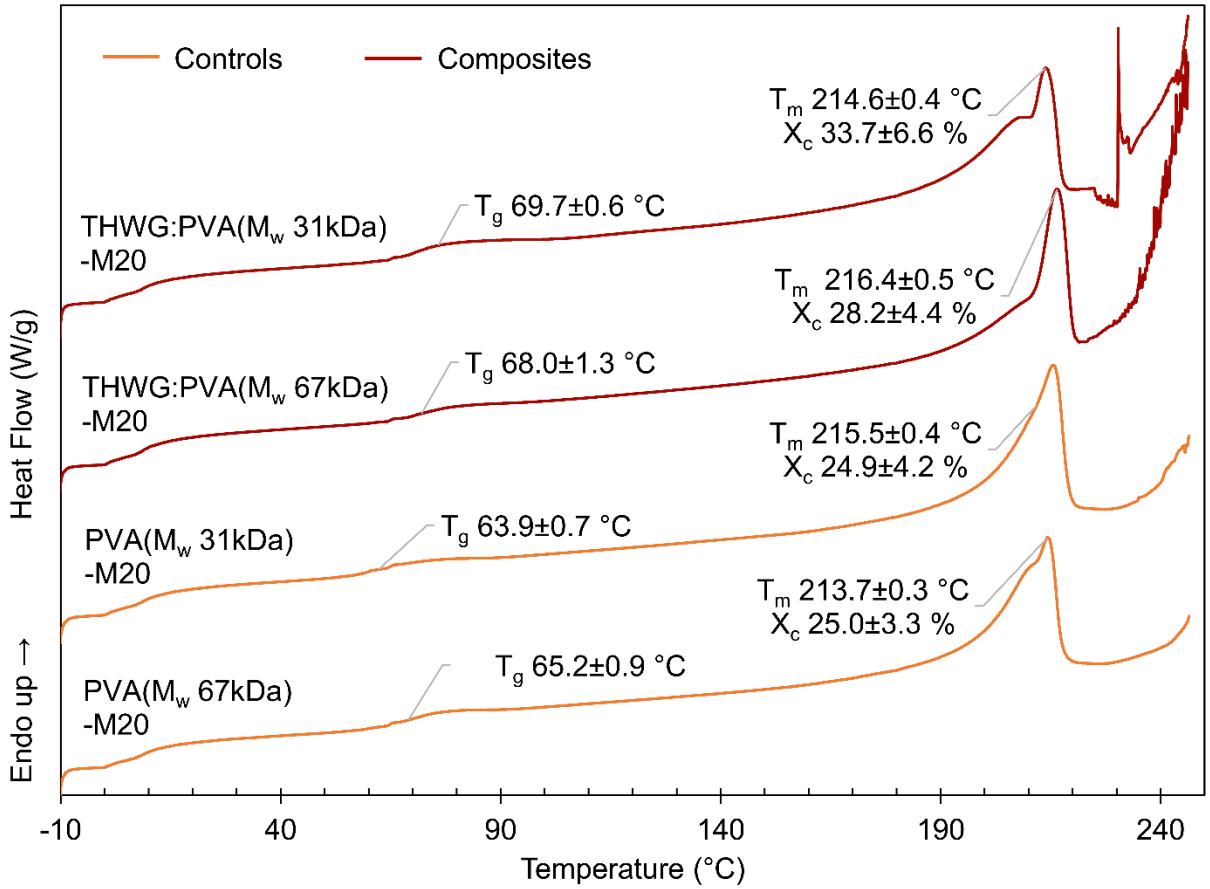


**Figure S2.** DSC second heat scans of PVA control and 33% THWG:PVA composites comparing the effect of PVA molecular weight at constant processing conditions on the PVA and composite thermal properties. Data is also shown along with the modulus data for each material in Table 1 of the manuscript.

APPENDIX B. SUPPORTING INFORMATION: Hydrolyzed wheat protein as a self-assembled reinforcing filler in synthetic isoprene rubber vulcanizates.

DeButts, B. L., Thompson, R.V., & Barone, J. R. (2019). Hydrolyzed wheat protein as a self-assembled reinforcing filler in synthetic isoprene rubber vulcanizates. *Ind. Crops Prod.*, (in review).

Chapter V has been submitted to and is under review by the following peer-reviewed journal: *Industrial Crops and Products* published by Elsevier B.V. The chapter is formatted according to the journal guidelines set forth by the publishers.

**SUPPORTING INFORMATION:**

# Hydrolyzed wheat protein as a self-assembled reinforcing filler in synthetic isoprene rubber vulcanizates

Barbara L. DeButts[a,b], Renee V. Thompson[c], Justin R. Barone[a-e*]

[a]*Macromolecular Science and Engineering,* [b]*Macromolecules Innovation Institute, Virginia Tech, Blacksburg, VA 24061*

[c]*NSF RET: Biomechanics from molecular to organismal scales*

[d]*Biological Systems Engineering, Virginia Tech, 301D Human and Agricultural Biosciences Building 1, 1230 Washington St. SW, Blacksburg, VA 24061*

[e]*Center for Soft Matter and Biological Physics, Department of Physics, 850 W. Campus Dr., Virginia Tech, Blacksburg, VA 24061*

*Corresponding author.

*E-mail address:* jbarone@vt.edu (J.R. Barone).

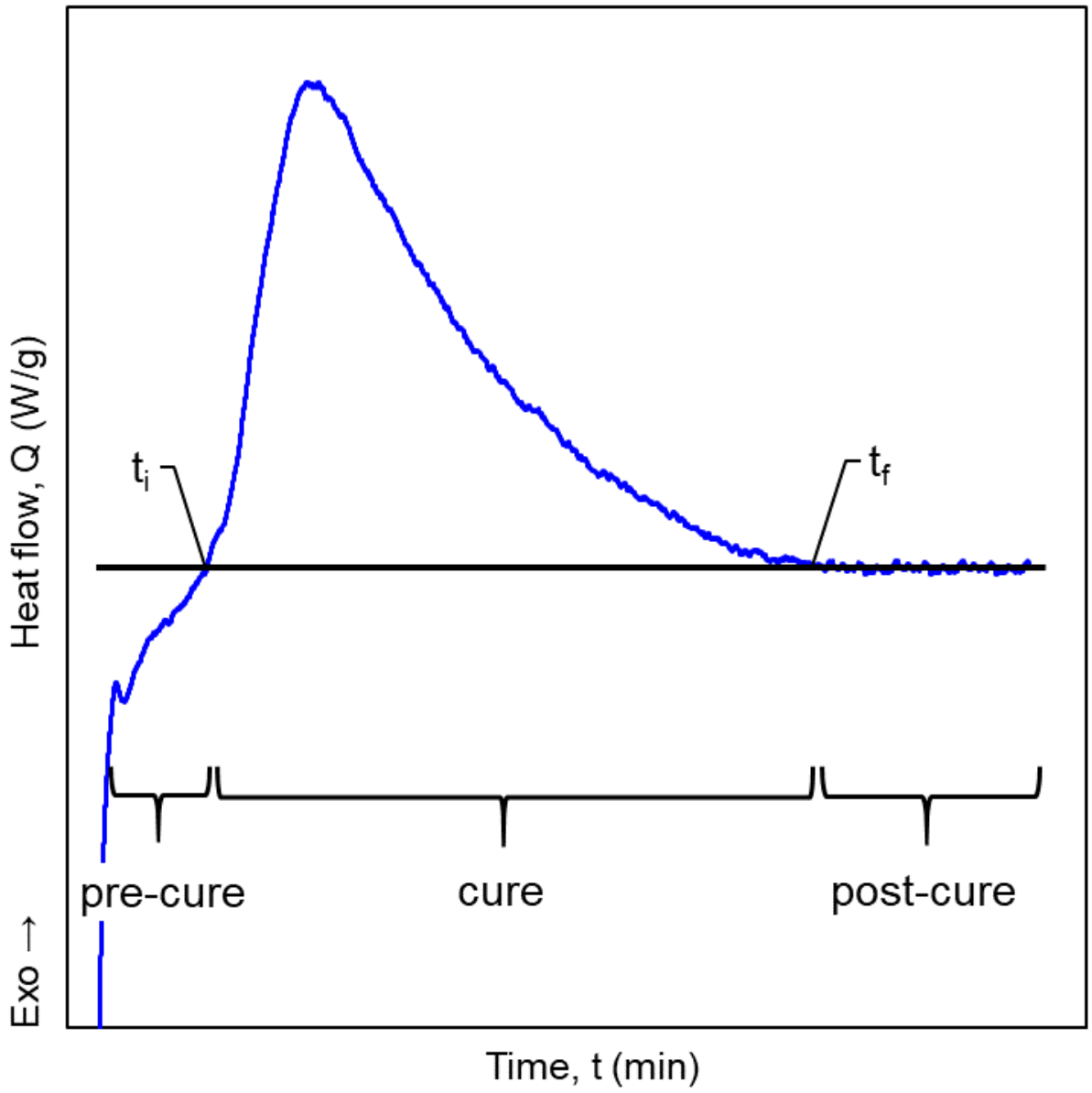


**Figure S1.** A typical isothermal curing curve of heat flow (Q) versus time (t) with the pre-cure (i.e., induction period or scorch time), cure, and post-cure periods and a horizontal baseline originating from the heat flow plateau after curing identified on the graph. The time at which curing starts ($t_i$) and ends ($t_f$) are located at the intersection of the baseline with the experimental data.

## APPENDIX C. SUPPORTING INFORMATION: Agricultural proteins as multifunctional additives in ZnO-free synthetic isoprene rubber vulcanizates.

DeButts, B. L., Chauhan, N., & Barone, J. R. (2019). Agricultural proteins as multifunctional additives in ZnO-free synthetic isoprene rubber vulcanizates. *J. App. Polym. Sci.*, (in review).

Chapter VI has been submitted to and is under review by the following peer-reviewed journal: the *Journal of Applied Polymer Science* published by John Wiley & Sons, Inc. The chapter is formatted according to the journal guidelines set forth by the publishers.

**SUPPORTING INFORMATION:**

# Agricultural proteins as multifunctional additives in ZnO-free synthetic isoprene rubber vulcanizates

Barbara L. DeButts[1], Natasha Chauhan[2], and Justin R. Barone[1,3,4*]

[1]Macromolecular Science and Engineering and Macromolecules Innovation Institute, Virginia Tech, Blacksburg, VA, 24061, United States

[2]Department of Chemical Engineering, Virginia Tech, 245 Goodwin Hall, 635 Prices Fork Road, Blacksburg, VA 24061, United States

[3]Biological Systems Engineering, Virginia Tech, 301D Human and Agricultural Biosciences Building 1, 1230 Washington St. SW, Blacksburg, VA 24061, United States

[4]Center for Soft Matter and Biological Physics, Virginia Tech, Blacksburg, VA 24061, United States

[*]Corresponding author email: jbarone@vt.edu (J.R. Barone)

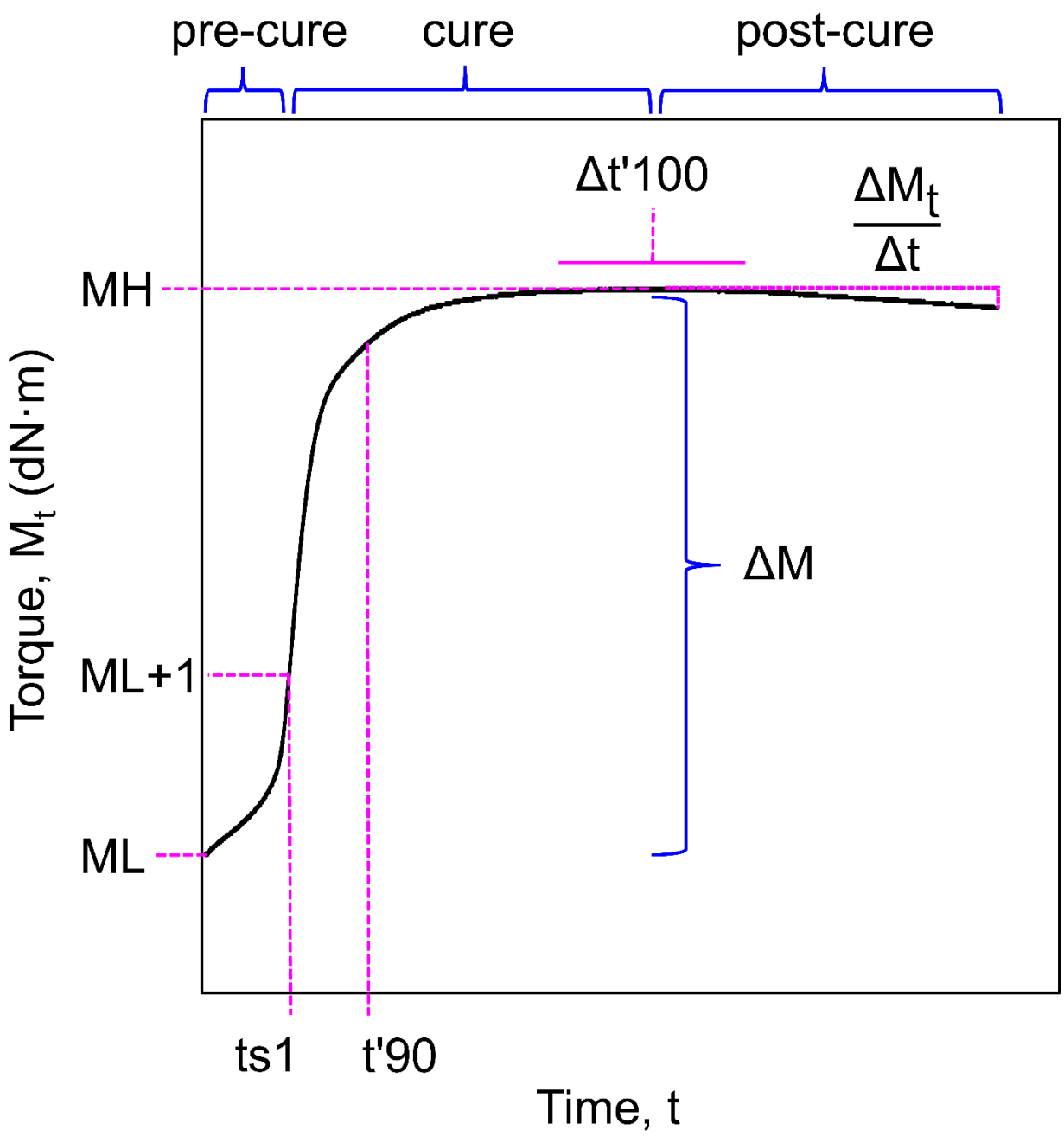


**Figure S1.** A typical S-shaped cure curve of elastic torque ($M_t$) versus time (t) with the pre-cure, cure, and post-cure periods and cure properties identified on the graph: minimum torque (ML); maximum torque (MH); torque change (ΔM); scorch time (ts1); cure time (t'90); elapsed time 100% cure (Δt'100); rate of reversion ($\Delta M_t/\Delta t$).